

Growth study of Fe on Be(0001) by scanning tunneling microscopy and spectroscopy

Dissertation
zur Erlangung des Doktorgrades
an der Fakultät für Mathematik, Informatik und
Naturwissenschaften
Fachbereich Physik
der Universität Hamburg

vorgelegt von

Hermann Ulrich Osterhage

Hamburg

2022

Gutachter der Dissertation:

Prof. Dr. Roland Wiesendanger
Prof. Dr. Wolfgang Hansen

Zusammensetzung der Prüfungskommission:

Prof. Dr. Roland Wiesendanger
Prof. Dr. Wolfgang Hansen
PD Dr. habil. Guido Meier
Dr. Stefan Krause
Prof. Dr. Michael Potthoff

Vorsitzender der Prüfungskommission:

Prof. Dr. Michael Potthoff

Datum der Disputation

31.03.2022

Vorsitzender des Fach-Promotionsausschusses PHYSIK:

Prof. Dr. Wolfgang J. Parak

Leiter des Fachbereichs PHYSIK:

Prof. Dr. Günter H. W. Sigl

Dekan der Fakultät MIN:

Prof. Dr. Heinrich Graener

Abstract

In this thesis, scanning tunneling microscopy and spectroscopy were used to probe the Be(0001) surface and the growth behavior of iron on top of it. The experiments were performed under ultra-high vacuum conditions with home-build scanning tunneling microscopes at cryogenic temperatures between 4.2 K and 60 K.

A cleaning procedure for the (0001) surface of Be single crystals based on Ar^+ ion sputtering at elevated temperatures was developed that yields extended parallel terraces with a low defect density. The electronic band structure of the clean Be(0001) surface was investigated by scanning tunneling spectroscopy. The parabolic dispersion of a surface state band is identified in interference patterns of the surface charge density. Inelastic electron tunneling spectroscopy further reveals the contributions of phonon-assisted tunneling of electrons into Be(0001).

The growth of iron on this surface by evaporative deposition was studied in dependence of the iron coverage and of the substrate temperature during and after deposition. At room temperature, island growth in the Volmer-Weber mode occurs. At 300 °C, intermixing of deposited iron with the substrate is observed and substantiated by Auger electron spectroscopy. Alloyed films with a locally (2×2) -ordered surface structure form in the process. This growth mode persists for iron coverages between 0.5 atomic layers and 3.8 atomic layers. The surface structure of these ordered alloyed films is found to resemble stretched (0001) planes of bulk-truncated FeBe_2 in a Laves structure.

Zusammenfassung

Im Rahmen dieser Arbeit wurden die Be(0001)-Oberfläche und darauf gewachsene Eisenfilme mittels Rastertunnelmikroskopie und Rastertunnelspektroskopie untersucht. Die Experimente wurden unter Ultrahochvakuumbedingungen bei kryogenen Temperaturen zwischen 4.2 K und 60 K durchgeführt.

Für diese Studien wurde eine Reinigungsprozedur für die (0001)-Oberfläche von Berylliumeinkristallen entwickelt. Diese basiert auf Kathodenzerstäubung mit Ar^+ -Ionen bei erhöhter Proben temperatur und liefert Probenoberflächen mit ausgedehnten, parallel orientierten Terrassen von geringer Verunreinigungsdichte. Anschließend wurde die elektronische Bandstruktur von reinen Be(0001)-Oberflächen mittels Rastertunnelspektroskopie untersucht. Anhand von Interferenzmustern in der Ladungsdichte an der Oberfläche wurde die parabolische Dispersion eines Oberflächenzustands identifiziert. Inelastische Rastertunnelspektroskopie offenbart den Beitrag von durch Elektron-Phonon-Wechselwirkung assistiertem Tunneln zum gesamten Tunnelstrom.

Das Wachstum von auf diese Oberfläche aufgedampftem Eisen wurde in Abhängigkeit der aufgetragenen Eisenmenge und der Substrattemperatur untersucht. Bei Raumtemperatur tritt Inselwachstum im Volmer-Weber-Modus auf. Hingegen weist die veränderte Oberflächenmorphologie bei 300 °C zusammen mit Auger-Elektronenspektroskopie auf eine Vermischung des aufgetragenen Eisens mit dem Be(0001)-Substrat hin. Infolgedessen bilden sich legierte Filme, deren Oberfläche lokal (2×2) -geordnete Bereiche aufweisen. Dieser Wachstumsmodus wurde für eine Eisenbedeckung zwischen 0.5 und 3.8 Atomlagen beobachtet. Die Oberflächenstruktur dieser geordneten Filme entspricht verspannten (0001)-Ebenen von FeBe_2 in einer Laves-Struktur.

Contents

1	Introduction	1
2	Methodology of surface investigations	5
2.1	Basic principle of STM	5
2.2	Scanning tunneling spectroscopy	7
2.3	Spin-polarized scanning tunneling spectroscopy	10
2.4	Inelastic scanning tunneling spectroscopy	11
2.5	Principles of Auger electron spectroscopy	12
3	Instrumentation and experimental implementation	15
3.1	Surface preparation facilities	15
3.2	Tip fabrication	18
3.3	The variable-temperature STM	19
3.4	The low-temperature STM	21
4	Physical properties of Be(0001) and ϵ-Fe	25
4.1	Electronic properties of Be(0001)	25
4.1.1	Theory of a 2D electron gas reflected in STM	26
4.1.2	Previous STM investigations of Be(0001)	28
4.2	Physical properties of the high-pressure ϵ -phase of Fe	29
5	Preparation of the clean Be(0001) surface	31
5.1	The beryllium crystals	31
5.2	Previously established <i>in situ</i> cleaning procedures for Be surfaces	32
5.3	Refined sputter cleaning of Be(0001) for STM experiments	33
5.3.1	Interdependence of preparation parameters	34
5.3.2	Preparation step one: The influence of the annealing temperature	38
5.3.3	Preparation step two: Minimization of the impurity density	40
5.3.4	Reproducibility in the low-temperature system	43
6	Characterization of the Be(0001) surface by STM and STS	47
6.1	Be(0001) imaged on the atomic scale	47

6.2	Scanning tunneling spectroscopy results on Be(0001)	51
6.3	Mapping the surface electron dispersion	56
6.4	Inelastic tunneling effects on Be(0001)	62
6.4.1	Results of inelastic tunneling spectroscopy	62
6.4.2	Influence of electron-phonon coupling on the tunneling process	63
6.4.3	Bias dependence of the tunneling barrier height	67
7	Growth of Fe on Be(0001)	71
7.1	Mechanisms of thin film growth of Fe/Be(0001)	71
7.2	Growth for room temperature deposition of Fe	73
7.3	Growth for Fe deposition at elevated temperatures	77
7.3.1	Growth for Fe coverages ≤ 0.2 ML	77
7.3.2	Ordered Fe/Be(0001) films forming for Fe coverages ≥ 0.5 ML	86
7.4	Coverage-dependent Auger electron spectroscopy	101
7.5	Microscopic investigation of (2×2) -ordered Fe-Be films	106
7.5.1	Fe growth on Be(0001) compared to Fe-Be alloys	106
7.5.2	STS measurements on (2×2) -ordered films	116
8	SP-STM investigation on the Fe/Be(0001) surface	119
8.1	Characterization of the tip magnetization on the reference sam- ple Fe/Ir(111)	120
8.2	Probing Fe-Be islands with a spin-sensitive STM tip	123
9	Conclusion and perspective	131
	Bibliography	133
	Index of abbreviations	149
	Publications	151
	Conferences	153
	Danksagung / Acknowledgments	155

1 Introduction

The requirements of modern information technology for miniature data storage and energy-efficient computation devices have spurred research on low-dimensional magnetic systems. In this context, Fe films grown by molecular beam epitaxy (MBE) on various substrate materials were found to exhibit a variety of magnetic properties. Adaptation of the film to the substrate's lattice structure leads to Fe films with symmetries and interatomic distances that differ from the natural body-centred cubic (bcc) bulk phase of Fe (α -Fe). Atomic coordination and interatomic distances in turn determine the magnetic properties of a material. An important quantity in this respect is the exchange energy, favoring parallel or anti-parallel alignment of spins depending on the sign of the exchange constant. The exchange constant is generally distance-dependent, including changes of its sign [1]. Consequently, the magnetic ground states in heteroepitactic films may differ from the ferromagnetic bulk phase as well. Apart from that, interactions with the substrate material influence the magnetic properties.

Scanning tunneling microscopy (STM) is a useful tool to study the growth of such films. In STM, a biased tip with an atomically sharp apex is approached to a metallic sample surface close enough to detect a tunneling current between these two electrodes. Lateral scanning of the tip relative to the sample allows for imaging of the electronic surface density of states (DOS) with atomic-scale resolution in real space. Due to correlations of the atomic positions with the electronic DOS, the atomic order of surfaces can be resolved. Utilizing magnetic probe tips, spin-polarised scanning tunneling microscopy (SP-STM) additionally enables the imaging of the local sample magnetization at atomic-scale resolution [2]. Furthermore, the STM's lateral scanning capability facilitates local current injections into sample surfaces, enabling the manipulation of the surface magnetism and studies of its dynamics [3].

The system of Fe on Ir(111) is an example for the versatile magnetic textures occurring in thin films and related STM applications. A single atomic layer of Fe grows in continuation of the Ir(111) lattice (pseudomorphically) [4]. Due to the Dzyaloshinskii-Moriya interaction with the substrate favoring a non-collinear orientation of neighboring spins, the magnetic ground state of the Fe film is a lattice of nanometer-sized skyrmions [5].

In Fe films of two and three atomic layers on Ir(111), the magnetic ground states are spin spirals, arising as a consequence of competing exchange and Dzyaloshinskii-Moriya interaction [6, 7]. Lastly, inside an external magnetic field, the spin spiral in films of three atomic layers transitions to a skyrmionic state. These skyrmions could be switched individually by electric fields induced by an STM tip [8]. This shows that the combination of MBE and STM can be used to create and investigate thin films with tailored magnetic properties by choice of film thickness and substrate material. A variety of substrate materials was investigated in the past, including the bcc substrate material W and the hexagonal close-packed (hcp) material Re. While a pseudomorphically grown film of Fe/W(110) of monolayer thickness is ferromagnetic with an in-plane easy axis of the magnetization direction [9, 10], the Fe monolayer on W(001) is antiferromagnetic [11]. One pseudomorphic atomic layer of Fe on Re(0001) however has a non-collinear ground state [12, 13]. While these previously employed substrate materials have diverse crystal structures and surface terminations, their surface density is lower compared to α -Fe. Accordingly, tensile stress is present in pseudomorphically grown films.

Under high pressure, Fe is known to undergo a phase transition into an hcp phase (ϵ -Fe) [14, 15], representing a compressed atomic configuration with respect to the conventional α -phase. The ϵ -phase is of special interest since it is stable under conditions assumed to occur in the earth's core [16, 17]. The high pressures necessary for its synthesis are experimentally only attainable in diamond anvil cells. Consequently, experimental investigations of ϵ -Fe are limited to measurement techniques capable of penetrating the anvil cells. X-ray investigations showed that the transition occurs at pressures $p > 13$ GPa and coincides with a loss of ferromagnetic order [18]. Mössbauer spectroscopy found no hyperfine magnetic field in ϵ -Fe, leading to the conclusion that there are no ordered magnetic moments in this material and that it is paramagnetic [19, 20]. Conversely, density functional theory (DFT) calculations predict the existence of a magnetic ground state with antiferromagnetic or noncollinear order [21–23]. Fast spin fluctuations in these ordered states preventing Mössbauer detection of hyperfine fields were put forward as an explanation for this discrepancy [20]. Still, the magnetic properties of ϵ -Fe remain an open question and progress on this issue would have implications for geophysics and the understanding of the earth's core that stabilizes the geomagnetic field crucial for life on earth [17].

Fe films grown on a hcp substrate could possibly circumvent the experimental limitations of diamond anvil cells. By adaptation to a hexagonal substrate lattice with a lattice constant smaller than $a_{\epsilon\text{-Fe}} = 245$ pm [14], Fe films may grow in the compressed ϵ -phase. These films could then be characterized using SP-STM, providing direct insight into the spin texture on the surface of this film

with atomic-scale resolution. Prerequisites for this are that the growth actually occurs in this tightly-spaced manner and that the substrate does not critically affect the magnetic properties of the Fe film.

The element Be is a candidate for a substrate material with a basal lattice constant of $a_{\text{Be}} = 228 \text{ pm}$ [24]. Pseudomorphic growth on this substrate poses the potential of hosting Fe films in a hcp structure with an even smaller lattice spacing than bulk ϵ -Fe. On W(110), the pseudomorphically grown monolayer of Fe relaxes in higher coverages towards the natural bcc phase [25]. Similarly, Fe grown on a surface of Be may relax first into the ϵ -phase and lastly into α -Fe for even higher coverages.

This thesis focuses on the preparation and characterization of Be(0001) surfaces and the investigation of Fe growth on this surface in dependence of coverage and substrate temperature. While the main motivation for this study is the promise of creating an ϵ -Fe specimen accessible for STM, the Be(0001) surface itself has unique electronic properties and a scanning tunneling spectroscopy (STS) investigation of it was lacking so far. Knowledge of the electronic properties and their manifestation in STM and STS is crucial for the interpretation of data acquired on overlayers on this substrate. Previous experimental investigations of the electronic structure of Be(0001) were limited to photoemission experiments [26–30]. The surface electronic properties of Be(0001) differ significantly from the bulk properties. In bulk Be, the electronic DOS is low around the Fermi level making it effectively a semimetal [30, 31]. Localized within the two uppermost atomic planes [32], Be(0001) hosts free-electron-like surface states [26, 27, 29] that contribute 80 % to the electronic surface DOS [33]. This peculiar electronic structure with a thin metallic surface region on an otherwise semimetallic bulk [34] sets Be(0001) apart from previously investigated substrate materials for Fe growth.

Free-electron-like surface states also exist on noble metal surfaces. The case of Pt(111) was used to study the distance-dependent exchange coupling, the so-called Ruderman-Kittel-Kasuya-Yosida (RKKY) interaction, between magnetic moments of adatoms mediated by conduction electrons [1]. However, Pt and heavy metals in general exhibit spin-orbit coupling and magnetic adatoms or films on their surfaces will thus be additionally affected by the Dzyaloshinskii-Moriya interaction [35]. Light Be with only four electrons per atom could pose a basis for RKKY coupled spins mediated by surface electrons in the absence of spin-orbit coupling.

Delocalized surface state electrons scatter from residual impurities or step edges on surfaces and create interference patterns of the DOS, called Friedel oscillations, that can be detected using STM [36]. A previous investigation of Be(0001) reported an enhanced amplitude of oscillations in STM constant-

current contours for low bias values, corresponding to electronic states near the Fermi level [37]. This apparently contradicts the free electron picture of the Be(0001) surface state, corroborated by photoemission data [26, 27, 29], that implies a constant surface state DOS. Strong electron-phonon coupling, affecting the electron dispersion and thus enhancing the electronic DOS near the Fermi level, was discussed as one possible explanation [38]. Another possible explanation revolved around the potential formation of a charge density wave (CDW) on Be(0001).

Based on previously employed routines [29, 39–41], the sputter cleaning procedure for Be(0001) was refined in this work to yield extended terraces with low impurity concentration. This poses the basis for studies involving STM and STS on the Be(0001) substrate itself and of subsequently deposited Fe. The electronic properties of Be(0001) were probed using STS to study the influence of bulk and surface states on the tunneling process, respectively. The surface charge oscillations on this surface were revisited and characterized spectroscopically in dependence of energy to discriminate between contributions of Friedel oscillations and a supposed CDW. Additionally, inelastic electron tunneling spectroscopy (IETS) was used to probe the electron-phonon coupling in this surface. Afterwards, Fe was deposited on the substrate and the growth was studied in dependence of the deposited amount and of the substrate temperature. STM and STS were used to investigate the morphology and complexity of the resulting islands and films. Additional information about the structure and chemical composition of the grown overlayers was gathered using low energy electron diffraction (LEED) and Auger electron spectroscopy (AES).

In this thesis, the electronic surface properties of Be(0001) and the potential of this surface as a host substrate for Fe films in a compressed hcp phase are investigated. The physical processes behind the employed experimental methods are described in Chapter 2. In Chapter 3, the methods of tip and sample preparation, as well as the used experimental setups are presented. The physical properties of Be(0001) and ϵ -Fe, as well as previous investigations of these materials are compiled in Chapter 4. An investigation of the influence of sputter cleaning parameters on the resulting morphology and impurity density of Be(0001) follows in Chapter 5. The results of an STS study conducted on the cleaned surface regarding surface charge oscillations on Be(0001), the surface state band, and electron-phonon coupling are covered in Chapter 6. Chapter 7 covers the actual growth of Fe on Be(0001) as studied using STM, STS, LEED and AES in dependence of the substrate temperature. Investigations of the Fe/Be(0001) system using a spin-sensitive tip are presented in Chapter 8. Lastly, a conclusion and an outlook to further perspectives of this work are given in Chapter 9.

2 Methodology of surface investigations

The experimental results presented in this thesis were obtained using STM and STS. These techniques allow for the investigation of the electronic structure of conducting sample surfaces with atomic-scale spatial resolution. The experiments are complemented by AES to obtain information on the chemical surface composition. This chapter introduces the working principle of STM and AES. The operational modes of STM employed in this work and their relation to physical quantities are described.

2.1 Basic principle of STM

In STM, the quantum mechanical phenomenon of tunneling across a barrier between two conducting electrodes is utilized to map the surface of a sample. This is realized by applying a bias voltage U between the sample and a measurement tip across a vacuum gap, and approaching the tip to the sample. A schematic of the STM geometry with bias applied to the sample and the tip on ground potential is depicted in Figure 2.1. At a sufficiently small separation of the electrodes ($\Delta z \lesssim 1$ nm), electrons can tunnel across the gap and the resulting current can be measured.

The magnitude of the tunnel current depends on the DOS of tip and sample electronic states involved in the tunneling process. The Bardeen approach to tunneling processes using perturbation theory has proven to give a suitable description for tunneling experiments [42]. Within this approach, the electron

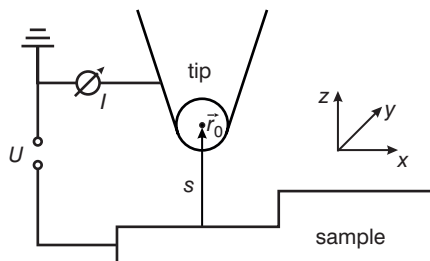


Figure 2.1: Schematic of the tunnel junction in STM. The tip apex is approximated as a sphere with the center at \vec{r}_0 , according to the Tersoff-Hamann model. A vacuum gap separates the tip and the sample. The width of the gap is defined as the distance s between \vec{r}_0 and the sample surface. A bias voltage U is applied between tip and sample with the tip held on ground potential.

wave functions in the two electrodes are treated as independent and their overlap in the barrier region governs the transition matrix element M , and thus the tunneling probability. The general expression for the tunneling current then reads [43]

$$I = \frac{4\pi e}{\hbar} \int_{-\infty}^{\infty} [f(E_F - eU + E) - f(E_F + E)] \times \rho_S(E_F - eU + E) \rho_T(E_F + E) |M|^2 dE, \quad (2.1)$$

where $f(E) = (\exp(E/(k_B T)) + 1)^{-1}$ is the Dirac distribution function with the Boltzmann constant k_B , and ρ_T and ρ_S denote the electronic DOS of tip and sample, respectively. At low temperatures, this can be simplified to [43]

$$I = \frac{4\pi e}{\hbar} \int_0^{eU} \rho_S(E_F - eU + E) \rho_T(E_F + E) |M|^2 dE. \quad (2.2)$$

It becomes evident that the current depends on the DOS of both electrodes in an energy interval set by the bias voltage.

The tunneling matrix element M depends on the precise choice of wave functions inside tip and sample. Tersoff and Hamann considered a spherical tip with radius R in the so-called s -wave approximation, neglecting contributions with quantum number $l > 0$ to the matrix element [44]. Additionally assuming a small bias voltage, one obtains [45]

$$I \propto U \rho_T(E_F) e^{2\kappa R} \rho_S(E_F, \vec{r}_0), \quad (2.3)$$

with the decay constant

$$\kappa = \frac{\sqrt{2m_e\phi}}{\hbar}. \quad (2.4)$$

Here, m_e is the electron mass and ϕ is an effective potential barrier. The current in this model for small bias is proportional to the sample DOS around E_F at the center of the tip \vec{r}_0 . The tip-sample separation in this approximation is defined as the distance s between the sample surface plane and \vec{r}_0 . Because of the exponential decay of electron wave functions into the vacuum region, also the measured tunneling current has an exponential dependence on the distance between tip and sample [45]:

$$I \propto e^{-2\kappa s}. \quad (2.5)$$

Using piezoelectric actuators to control the tip position, images based on the previously explained effects can be obtained. For this, the tip is scanned line by

line laterally across the sample surface. In the most commonly used constant-current operation mode, the measured tunneling current is used as a reference for a feedback loop that adjusts the vertical (z) position of the tip to keep the current constant. The resulting profiles $z(x, y)$ contain information on the surface topography and its electronic density. Within the Tersoff-Hamann model, z is a contour of constant sample DOS at E_F and gives a good approximation of the topography for samples with a homogeneous DOS. Generally, especially for samples consisting of different atomic species, the influences of electronic DOS and topography onto the constant-current map are difficult to distinguish.

2.2 Scanning tunneling spectroscopy

For higher bias values, states lying away from the Fermi level also contribute to the tunneling process as can be seen from the general expression in Equation (2.2). The situation is schematically depicted in Figure 2.2. In the absence of a bias voltage, the Fermi levels in both electrodes align as shown in Figure 2.2 (a). ϕ_T and ϕ_S denote the work functions of tip and sample, respectively. The sample DOS is traced in between the electrodes. The tip density of states will be treated as constant in the following and is not depicted. Shaded regions correspond to occupied states. A positive bias U applied to the sample will shift the sample states by $-eU$ relative to the Fermi level of the tip, as shown in Figure 2.2 (b). Electrons from the tip will now tunnel into unoccupied sample states within the energy interval $[E_F, E_F + eU]$. Conversely, for negative values

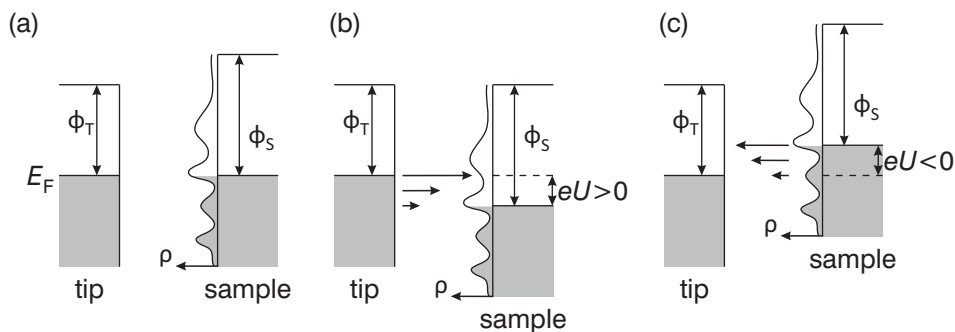


Figure 2.2: Electronic states contributing to the tunneling process. (a) The Fermi levels of tip and sample are aligned in the absence of a bias voltage U . (b) For positive sample bias, the sample states are shifted downwards in energy by eU and electrons tunnel elastically into unoccupied sample states. (c) For negative sample bias, the sample states are shifted upwards and electrons tunnel from the sample into unoccupied tip states.

of U , electrons tunnel from occupied sample states within $[E_F - eU, E_F]$ into the tip (see Figure 2.2 (c)).

We will now consider the differential tunneling conductance dI/dU . Influences of the matrix element are expressed as an energy- and bias-dependent transmission probability [46, 47]

$$T(E, U, s) = \exp \left[-2s \sqrt{\frac{2m_e}{\hbar^2} \left(\phi + \frac{eU}{2} - E + \frac{\hbar^2 k_{\parallel}^2}{2m_e} \right)} \right]. \quad (2.6)$$

Here, k_{\parallel} is the electron momentum parallel to the sample surface. States with high parallel momenta k_{\parallel} decay faster into the vacuum and consequently their transmission probability is diminished [45]. With the assumption of a slowly varying (free-electron-like) DOS of the tip, differentiation of Equation (2.2) leads to the differential tunneling conductance

$$\begin{aligned} \frac{dI}{dU}(U) &\propto \rho_T(E_F) \rho_S(E_F + eU) T(eU, eU) \\ &+ \int_0^{eU} \rho_T(eU - E) \rho_S(E) \frac{dT(E, eU)}{dU} dE. \end{aligned} \quad (2.7)$$

The transmission coefficient is monotonically increasing with absolute bias $|U|$ and contributes a smooth background to the first term in Equation (2.7), while the second term is often neglected [48]. Consequently, $dI/dU(U)$ can be interpreted as a measure for ρ_S at the energy eU .

Measurement of dI/dU is conventionally realized by applying an ac modulation voltage U_{mod} to the tunneling junction on top of the dc voltage U . Using lock-in detection, the oscillation amplitude of the tunneling current caused by the modulation voltage can be measured. If the modulation frequency f is chosen outside the bandwidth of the current feedback loop, images of dI/dU can be acquired together with the constant-current image. In this case, the feedback loop keeps the time-averaged current equal to the setpoint and does not react to the faster oscillating ac-component. The resulting dI/dU maps contain information on spatial variations of $\rho_S(eU)$ and T , due to local variations of the tunneling barrier height ϕ . Alternatively, the dc bias voltage can be varied at a stationary tip position and dI/dU can be acquired as a function of U at a fixed position of the sample to investigate the local structure of the sample DOS.

The considerations above were made in the approximation of zero temperature. For finite temperatures, the Fermi-Dirac distribution function dictates the occupation of electronic states. Contributions to $dI/dU(U)$ are not strictly limited anymore to states at $E = eU$ of the positively biased electrode because the

negatively biased electrode has a finitely occupied DOS above the Fermi level. As a consequence, features in the tunneling spectrum related to the DOS will smear out. The effect can be described by a convolution of the zero-temperature conductance with the broadening function [49]

$$\eta_{\text{th}}(U) = \cosh^{-2}\left(\frac{eU}{2k_{\text{B}}T}\right). \quad (2.8)$$

The FWHM of this function is $3.5k_{\text{B}}T$, which limits the energy resolution of STS. At 4.2 K, the temperature of liquid He, the energy resolution is thus limited to $\Delta E \approx 1$ meV.

Additionally, the measurement principle based on lock-in technique and a sinusoidal modulation voltage of root mean square amplitude $U_{\text{mod}} = U_{\text{pk}}/\sqrt{2}$ smears out the tunneling spectra. This so-called instrumental broadening is given by a convolution with [49]

$$\eta_{\text{inst}}(U) = \begin{cases} \frac{2\sqrt{U_{\text{pk}}^2 - U^2}}{\pi U_{\text{pk}}^2} & \text{for } |U| \leq U_{\text{pk}}, \\ 0 & \text{for } |U| > U_{\text{pk}}, \end{cases} \quad (2.9)$$

with a FWHM of $\approx 2.5U_{\text{mod}}$. Consequently, the energy resolution in STS is limited to

$$\Delta E = \sqrt{\Delta E_{\text{th}}^2 + \Delta E_{\text{inst}}^2} = \sqrt{(3.5k_{\text{B}}T)^2 + (2.5eU_{\text{mod}})^2}. \quad (2.10)$$

We will now consider the influence of a temperature difference across the tunnel junction. If the temperatures of tip and sample differ, $T_{\text{T}} \neq T_{\text{S}}$, the occupation of states in both electrodes will smear out by different amounts. This results in electrons with energy $E > E_{\text{F}}$ tunneling from the hot electrode into the cold electrode and electrons with $E < E_{\text{F}}$ tunneling in the opposite direction. The resulting net current generated from these contrary effects depends on the variations of matrix element and DOS with energy as seen from Equation (2.1). Following the considerations of Tersoff and Hamann [44], Støvneng and Lipavský developed a model for the thermovoltage arising in STM due to this effect [50]. Assuming a constant matrix element and a slowly varying DOS near E_{F} for both electrodes, the thermovoltage for small bias values reads [50, 51]

$$U_{\text{th}} = \frac{\pi^2 k_{\text{B}}}{6e} (T_{\text{T}}^2 - T_{\text{S}}^2) \left. \frac{\sigma'}{\sigma} \right|_{U=0}. \quad (2.11)$$

Here, $\sigma = dI/dU$ is the conductance and $\sigma' = d\sigma/dU$ its first derivative with respect to the bias voltage. This means that the thermovoltage can be quantified

in STS by measuring dI/dU and d^2I/dU^2 in the vicinity of $U = 0$ when the temperatures of both electrodes are known, and even lateral variations in U_{th} can be resolved. Conversely, with lateral variations in the sample DOS, and hence in the tunneling conductance, the effective bias voltage $U_{\text{eff}} = U + U_{\text{th}}$ will vary depending on the tip position, leading to ill-defined tunneling conditions. This compromises the interpretation of STM and STS data when thermovoltage is neglected in the presence of substantial temperature gradients across the tunnel junction.

2.3 Spin-polarized scanning tunneling spectroscopy

In the considerations so far, the spin degree of freedom of the electron was neglected. However, a ferromagnetic electrode for example will generally have a DOS divided into unequal contributions of opposite spin ρ_{\uparrow} and ρ_{\downarrow} . The difference in the spin-resolved DOS determines the electrodes' magnetization $\vec{m}_i = (\rho_{i,\uparrow} - \rho_{i,\downarrow}) \hat{e}_i$ and spin polarization

$$P_i(E) = \frac{\rho_{i,\uparrow} - \rho_{i,\downarrow}}{\rho_{i,\uparrow} + \rho_{i,\downarrow}}, \quad (2.12)$$

where \hat{e}_i denotes the unit vector of the quantization axis in the respective electrode. Elastic tunneling between the two electrodes has to conserve energy and spin momentum. Consequently, electrons from the tip carrying spin \uparrow or \downarrow can only tunnel into unoccupied sample states of the same spin direction. ρ_{\uparrow} and ρ_{\downarrow} are shifted in energy relative to each other for different occupations, resulting in different densities of available final states. Depending on the local sample magnetization \vec{m}_S and assuming a constant tip magnetization \vec{m}_T , the resulting tunneling current will thus differ in dependence of the relative alignment of \vec{m}_S and \vec{m}_T with extremal values for (anti-)parallel alignment [52].

Extending the Tersoff-Hamann model to spin-polarized tunneling under the assumption of constant $\rho_{T,\uparrow}$ and $\rho_{T,\downarrow}$ yields [53]

$$I \propto \rho_T \int_0^{eU} \rho_{S,\uparrow}(E_F + E, \vec{r}_0) + \rho_{S,\downarrow}(E_F + E, \vec{r}_0) dE + \vec{m}_T \int_0^{eU} \vec{m}_S(E_F + E, \vec{r}_0) dE. \quad (2.13)$$

The second term implicitly contains the difference of the integrated spin-resolved

sample DOS. Certain bias voltages (and thus integration limits) may lead to a vanishing of this term and the result will be identical to the spin-averaged case.

The differential conductance however reads [53]

$$\frac{dI}{dU}(U) \propto \rho_T \rho_S(E_F + eU, \vec{r}_0) + \vec{m}_T \vec{m}_S(E_F + eU, \vec{r}_0). \quad (2.14)$$

The magnetic contrast in dI/dU is thus only dependent on the energy-resolved polarization and due to the scalar product on the angle θ enclosed by \vec{m}_T and \vec{m}_S :

$$\frac{dI}{dU}(U) \propto \sigma_0 (1 + P_T P_S(eU) \cos \theta), \quad (2.15)$$

with the spin-averaged conductance σ_0 . By choice of a bias voltage yielding a strong spin polarization in the sample, magnetic textures can appear much more pronounced in dI/dU compared to constant-current height contours that depend on the integrated spin-polarized current.

2.4 Inelastic scanning tunneling spectroscopy

Previously, only elastic tunneling processes, in which initial and final states are equal in energy, were discussed. When tunneling electrons excite a collective mode, they lose the energy $\hbar\omega$. This process, known as inelastic tunneling, is depicted in Figure 2.3 (a). In the reversely biased situation, electrons may as well tunnel inelastically from the sample into states of the tip. The final state has to be unoccupied, so that the threshold bias for inelastic tunneling via excitation

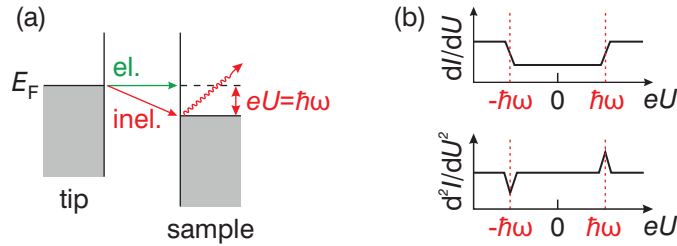


Figure 2.3: Inelastic tunneling processes in STS. (a) Schematic of the situation for positive sample bias. Electrons tunneling elastically from tip states at E_F into sample states at $E_F + eU$ are indicated by a green arrow. The inelastic tunneling process is depicted in red. An electron excites a quasiparticle mode with the energy $\hbar\omega_i$ and tunnels into a sample state at E_F . This poses an additional conductance channel beyond the threshold $|eU| > \hbar\omega$. (b) Consequently, the conductance dI/dU exhibits steps at the threshold for quasiparticle generation. The second derivative d^2I/dU^2 likewise shows peaks that are antisymmetric with respect to $U = 0$.

of a mode ω is given by $|eU| > \hbar\omega$ [54]. Above this threshold, the inelastic tunneling can be viewed as an additional conductance channel contributing to the total tunneling conductance. Consequently, steps can be measured in dI/dU at $eU = \pm\hbar\omega$ as shown in Figure 2.3 (b). Interesting from an experimental point of view is the second derivative of the tunneling current d^2I/dU^2 because inelastic excitations here appear as a pair of antisymmetric peaks around zero bias. This way, the energies of collective modes in the electrodes, such as molecular vibrational modes or phonons, can be determined and $d^2I/dU^2(U)$ exhibits a spectrum of possible excitations [45].

Inelastic electron tunneling spectroscopy (IETS) will be used in this work to study the coupling of electrons to surface phonons. The sketches in Figure 2.3 describe the situation for a single inelastic (phonon) excitation. On real solid surfaces there will be a continuous phonon spectrum with the phonon DOS $F(\omega)$. The inelastic spectrum will reflect this DOS weighed by a matrix element $M(\omega)$ that contains the coupling strength of tunneling electrons to the phonon modes [45]:

$$\frac{d^2I}{dU^2}(U) \propto |M(eU)|^2 F(eU). \quad (2.16)$$

To a good approximation, the matrix element is proportional to the electron-phonon interaction strength α , and d^2I/dU^2 is then a direct measure for the Eliashberg function α^2F [55, 56]

$$\frac{d^2I}{dU^2}(U) \propto \alpha^2F(eU). \quad (2.17)$$

Peaks in the IETS may appear slightly shifted compared to peaks in α^2F due to influences of the tunneling barrier [57].

2.5 Principles of Auger electron spectroscopy

Auger electron spectroscopy (AES) is an analytical method sensitive to the chemical composition of a material's surface. The chemical sensitivity stems from the distinct energy difference between atomic orbitals in chemical elements. Figure 2.4 depicts a schematic of the Auger process. A beam of primary electrons with an energy of typically $E_p = 3 \text{ keV}$ is focused on the sample surface. This electron beam can ionize atoms in the sample by emission of a secondary electron from an inner orbital with binding energy $E_B = E_a$. The process is schematically depicted in Figure 2.4 for the case of Be with the electron configuration $1s^22s^2$.

The resulting hole in the K shell will be spontaneously filled by an electron from an orbital of higher energy (L shell in this case) with the energy difference

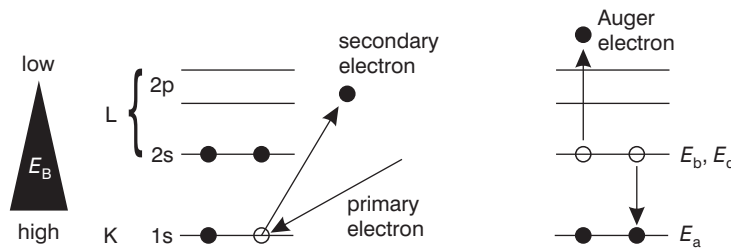


Figure 2.4: Schematic of the Auger process occurring in Be. A primary electron beam leads to ejection of an electron from the K shell. An electron from the L shell then drops into the K shell. An Auger electron is emitted carrying the excess energy as kinetic energy.

$E_a - E_b$, leaving the ion in an excited state. This excess energy is then released by either emission of a photon or — if it exceeds the binding energy E_c of other electrons in the atom — by emission of a so-called Auger electron [58]. The kinetic energy of the Auger electrons leaving the material reads

$$E_{\text{kin}} = E_a - E_b - E_c. \quad (2.18)$$

This quantity does not depend on the energy of the incident electron but only depends on the atomic energy levels. For Be with only two distinct energy levels of occupied orbitals, there is only one possible Auger process labeled KLL according to the original shells of participating primary, secondary and Auger electrons, respectively. For heavier elements, more possible transitions (LMM, MNN, etc.) exist. The surface sensitivity of this method stems from the finite mean free path of the Auger electrons inside the material. It extends to a maximum of 5 nm into the sample, with exponentially decaying contributions to the total Auger electron yield [58].

In an experiment, a cylindrical mirror analyzer is used to filter the Auger electrons for a particular kinetic energy. Electrons of only this energy pass through and are detected in an electron multiplier. By variation of the allowed passing energy, a spectrum of the detected number of electrons $N(E)$ is acquired that shows distinct peaks of Auger electrons on a continuous background formed by scattered electrons that experienced random energy losses in the sample prior to detection [58]. Conventionally, the differentiated Auger spectra $dN/dE(E)$ are presented and can be directly measured using lock-in technique. For this, an ac modulation voltage with an amplitude U_{mod} of a few mV is applied to the cylindrical mirror analyzer and the response on the electron detector, being proportional to $dN/dE(E)$, is measured. The rising and falling flanks of a peak in $N(E)$ correspond to positive and negative peaks in the differentiated spectrum. As the low-energy side of peaks in $N(E)$ is broadened due to energy loss, the negative peaks in $dN/dE(E)$ are usually quoted [58].

The intensity of peaks in the Auger spectrum depends on a multitude of parameters specific to both the sample under investigation and the employed hardware. For dN/dE spectra, the intensity of a peak i is proportional to U_{mod} , to the primary beam intensity I_p , and to the lock-in sensitivity g :

$$I_i \propto gU_{\text{mod}}I_p. \quad (2.19)$$

These are parameters that can be controlled experimentally. The surface roughness is a parameter that is less well-controlled and a rougher surface will lead to a lower measured intensity [58]. Furthermore, the response of an analyzer setup is generally energy dependent [59]. For identification of the chemical composition of an unknown sample, its Auger spectrum can be compared to spectra obtained on pure elemental samples or samples with a known stoichiometry. Qualitatively, the constituents of the sample under investigation can be identified by comparison of the measured peak positions to peak positions occurring for known samples.

Theoretically, the concentration c_i of an element i in an unknown sample is proportional to the ratio of the intensities of a corresponding peak in this sample I_i and the peak at the same energy in a pure sample $I_{i,0}$:

$$c_i = \frac{I_i}{I_{i,0}}. \quad (2.20)$$

Such a quantitative analysis requires reference samples for calibration. Another possibility for quantification is the assignment of normalized sensitivity factors S_i to certain characteristic peaks for various elements. The concentration of an element A in a sample can then be estimated in a single measurement through

$$c_A = \frac{I_A/S_A}{\sum_i I_i/S_i}, \quad (2.21)$$

where the summation is over one peak per element identified in the spectrum. For this purpose, Handbooks exist that compile reference spectra with tabulated values of S_i of all viable elements acquired with the same analyzer setup [58, 60]. Due to the surface sensitivity of AES, this method can only be applied rigorously to homogeneous samples, as the Auger yield reduces with distance from the sample surface. Also, an uncertainty remains concerning the comparability of the analyzers used in the experiment and in the reference measurements. The energy dependence of different setups differs considerably, so that there is a significant spread in the relative sensitivities across different handbooks [59].

3 Instrumentation and experimental implementation

The experimental results presented in this thesis were obtained by using two distinct experimental facilities. While both facilities essentially share the same appliances for sample preparation, the STMs mounted inside are dissimilar due to their different intended purpose. The variable temperature (VT) system is designed to allow studies over a broad temperature range between 24 K and room temperature with a small down time in between sample preparation and investigation. For studies requiring temperatures down to ~ 1 K or an external magnetic field, the low temperature (LT) system has to be employed.

This chapter provides an overview of techniques and devices used for sample and tip preparation as well as of the two STMs used in this work.

3.1 Surface preparation facilities

Ambiguities in the chemical composition of the sample, eg. impurities on the sample surface, will lead to ambiguities in the interpretation of experimental observations. Facilities and methods for preparing clean single crystal surfaces — and metallic adlayers thereon — under ultra-high vacuum (UHV) conditions (*in situ*) are presented in the following.

Both UHV systems share a design of three connected but individually sealable chambers, exemplarily depicted in Figure 3.1 for the LT system [61]. Samples or tips mounted on sample plates of 1 mm thickness made of heat resistant Mo or W may be introduced via an additional small load lock. Transfer rods and wobblesticks facilitate the transfer of samples and tips through the chamber systems. The STMs are situated in dedicated chambers to avoid a contamination of the insides, including the cryostats, during sample preparation.

Electron beam heating stages inside all chambers except the STM chambers allow for heating of the samples to over 2000°C. For metal surfaces with C impurities like W(110) or Ir(111), O₂ dosing valves are attached. Electron beam heating in an O₂ atmosphere leads to promotion of C impurities to the sample surface where they oxidize. The oxidized impurities can then be desorbed

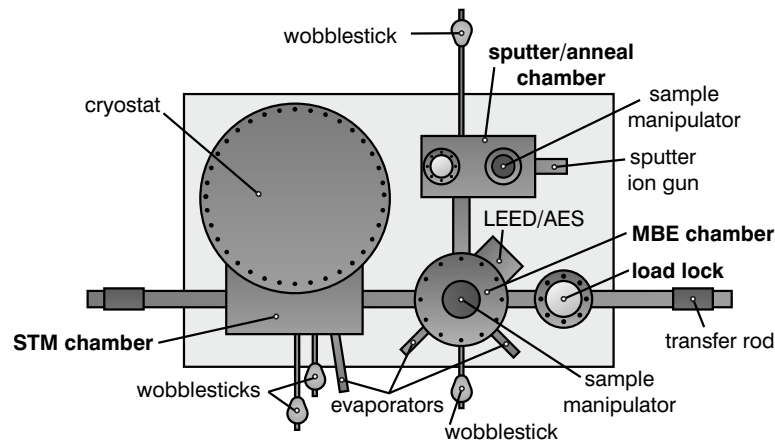


Figure 3.1: Schematic assembly of the vacuum chambers and components in the LT system. Image adapted with permission from [61].

by flashing to even higher temperatures or be removed by Ar^+ sputtering [62, 63].

For *in situ* sample or tip preparation, the systems are equipped with sputter ion guns of the following models: a SPECS IQE 11/35 in the VT system, and a SPECS IQE 12/38 in case of the LT system. Metallic overlayers can be grown on samples by MBE using electron beam evaporators. Sample manipulators allow the precise positioning of samples in front of ion gun, evaporators, or LEED/AES optics by linear motion and rotation. Detailed descriptions of the VT system and the LT system can be found in the dissertations of A. Schlenhoff [64] and J. Friedlein [65], respectively.

A schematic drawing of a sample manipulator used for surface preparation is depicted in Figure 3.2. A sample mounted on a sample plate is placed above the integrated ohmic heating element and radiatively heated from below. As heating elements, W wires and pyrolytic boron nitride elements are installed, allowing sample heating up to $\sim 1000^\circ\text{C}$ during sputtering or during material deposition. The sample temperature is monitored using a K-type thermocouple mounted on the manipulator near the contact point to the sample plate.

Ar^+ ion sputtering is a technique used to clean surfaces by removal of surface oxides, adlayers, or other impurities. The inert gas Ar is introduced into the UHV chamber through a leak valve to a partial pressure of typically $p_{\text{Ar}} < 1 \times 10^{-4}$ mbar. A filament wire inside the sputter ion gun is heated by an electric current to thermally overcome the work function of electrons inside the filament and create an electron cloud around it. These electrons can be accelerated towards an anode to ionize the surrounding Ar atoms in collision events. The resulting ions are then accelerated towards the sample with an

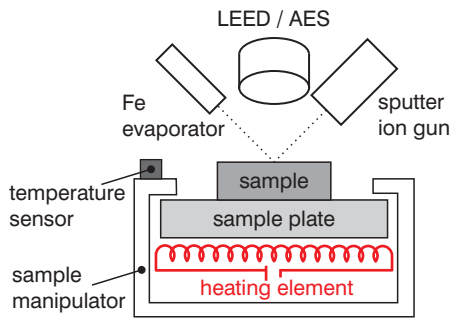


Figure 3.2: Schematic drawing of a sample manipulator installed in the UHV systems. The manipulator is equipped with a resistive heating element. Temperature readout is realized on the manipulator close to the sample plate. By movement of the manipulator, the sample can be positioned in front of evaporators, an ion sputter gun, or a combined LEED/AES assembly.

arbitrary acceleration voltage defining the kinetic energy of the Ar^+ ions $E_{\text{Ar}} = eU$. The typical energy range for sputter cleaning is 0.1 keV-5.0 keV and the ion current incident on the sample surface amounts to a few μA .

In consequence, the sample is bombarded by a beam of ions that knock atoms out of the sample surface in collisions. This way, material is removed from the sample surface over time. Simultaneously, the sputtering damages the surface, leading to a roughening or to implantation of Ar below the surface. Heating during or after the sputtering is required to anneal this damage and to reestablish a smooth surface by thermally activated reorganization of the surface atoms. The crystallinity of the surface and its chemical composition can be monitored intermittently by LEED and AES. Sputtering and annealing is repeated in cycles until the desired surface quality is obtained.

On a cleaned substrate surface, Fe overlayers can be grown by evaporative deposition. Inside the evaporator, a 2 mm thick cylindrical Fe rod is heated by electron bombardment until sublimation occurs. A shutter between the evaporator and the sample allows a controlled dosage of the deposited material. The growth can be influenced by variation of the substrate temperature, and by variation of the deposition rate depending on the evaporant heating power. A flux monitor detects a portion of the ions leaving the evaporator's aperture. This quantity — usually a few nA — is generally proportional to the deposition rate. The evaporators were calibrated based on the known growth behavior of Fe/W(110) in the VT lab and Fe/Ir(111) in the LT lab, respectively. The amount of deposited Fe was determined in the regime of ≈ 1 mono-layer (ML). Due to the smaller surface unit cell of Be(0001) compared to W(110) and Ir(111), the difference in atomic surface densities has to be taken into account, and the effective coverage Θ of pseudomorphically grown Fe/Be(0001) has to be corrected by a factor of 0.64 in case of W(110) [66] and 0.71 in case of Ir(111).

3.2 Tip fabrication

The application of the STM as a tool to precisely investigate electronic surface properties of the sample system under investigation requires means to prepare well defined tips. The main requirements for STM tips are sharpness, i.e. a tip apex with small aperture angle, for high spatial resolution and a metallic surface with slowly varying electronic DOS to prevent the distortion of tunneling spectra by tip artifacts [43, pp. 297]. In case of SP-STM, a spin-polarized tip apex is additionally required.

A natural choice for tunneling tips are noble metals because of their resistance against oxidation. Tips of sufficient sharpness can be readily produced by pulling apart a thin piece of Pt/Ir (90/10) wire. The wire will become ever thinner under tensile stress and eventually tear, leaving a small apex at the point of rupture. This alloy with 10 % Ir content is favored over pure Pt because it is harder and thus more resistant in case of contact with the sample [45]. Pt/Ir tips used in this work were prepared by tearing an end off a Pt/Ir (90/10) wire of 0.25 mm in diameter.

Another common tip sharpening technique is electrochemical etching. The tip material is submerged in a basic or acidic solution and biased against a counterelectrode. The preferential etching in the area just below the surface level of the solution, leads to formation of a neck in the tip material [67]. The material will tear once the neck can not support the weight of the submerged part anymore. Cr and W tips used in this work were prepared by electrochemical etching in solutions of 1 mol l^{-1} - 5 mol l^{-1} HCl and 2 mol l^{-1} KOH, respectively, under application of a bias voltage of 5 V. The raw material was a 99.95 % pure wire of 0.2 mm-0.75 mm in diameter in the case of W. For Cr tips, sticks with a cross section of $0.5 \text{ mm} \times 0.5 \text{ mm}$ cut from a foil of 99.99 % purity were used.

After the etching procedure, the tips can be mounted in a tip holder and inserted into UHV. However, they will still carry an oxide layer on the surface that may impede the STM or STS measurements. This oxide layer can be removed *in situ* by heating to high temperatures or by Ar^+ sputtering. Another possibility to manipulate the tip apex is the field emission treatment. For this, the tip is biased with approximately -200 V and approached to the sample until a field emission current of a few μA is observed. As a consequence of the high current, the tip apex will melt locally, lose material, and recrystallize [43, pp. 302]. To finally sharpen the tip microscopically in an STM experiment, it can be brought into contact with the sample in a controlled way by dipping a few Å into the sample and subsequent retraction. Also short bias pulses of $U \leq 10 \text{ V}$ are routinely applied to the tunnel junction for fractions of a second. Similar to

the field emission treatment, this induces microscopic reshaping of the tip apex and may fortuitously lead to a sharper configuration.

Cr tips used in this work were initially conditioned by field emission treatment at $U = -200\text{ V}$ and $I \geq 30\text{ }\mu\text{A}$ for at least 30 min. W tips used in the VT system were prepared by flash heating with $P = 20\text{ W}$ for 7 s using electron bombardment. W tips used in the LT system were sputtered for 25 min with $E_{\text{Ar}} = 1.2\text{ keV}$ and $p_{\text{Ar}} = 4 \times 10^{-7}\text{ mbar}$ upon insertion into UHV. All tips were further sharpened and conditioned by combinations of bias pulses and controlled contact with the sample surface. Additionally, spin-polarized tips were created by controlled dipping of Cr tips into Fe layers on Ir(111) and subsequent voltage pulses.

3.3 The variable-temperature STM

The variable-temperature scanning tunneling microscope (VT-STM) is a home-built instrument depicted in Figure 3.3 [68]. The microscope assembly stands on a base plate that is suspended from metal springs. Isolation from mechanical vibrations is achieved by an eddy-current damping stage. The STM itself is suspended inside a gold-plated radiation shield, from which it is thermally well decoupled. For a minimum contact surface, six ruby balls separate the metallic

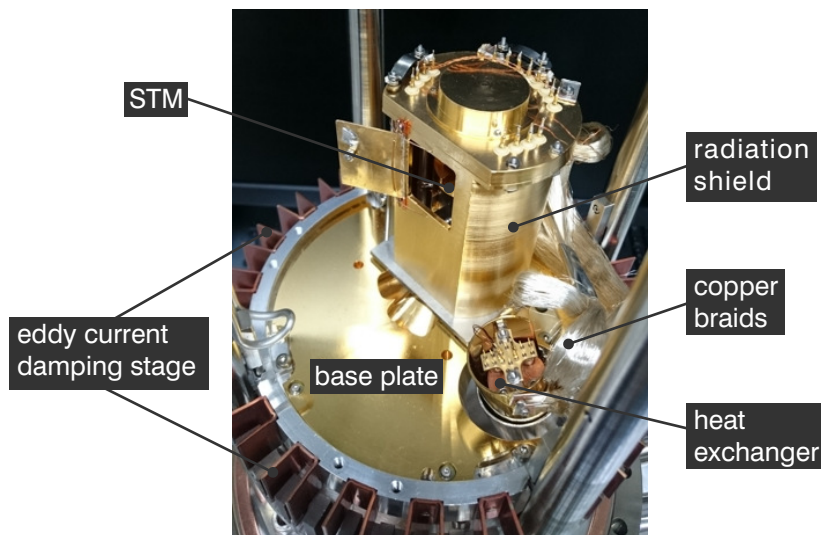


Figure 3.3: Photograph of the VT-STM on the eddy-current damping stage. The flow cryostat, terminated by the heat exchanger, can be seen in the foreground. Image adapted with permission from [68].

parts of the STM and the shield. Cooling of the STM is achieved by a liquid He flow cryostat. The exhaust of the cryostat is pumped by a scroll pump, drawing He through the assembly. The He flow cools the heat exchanger. The STM is thermally coupled to the heat exchanger via flexible copper braids in order to limit the transmission of vibrations from the cryostat to the STM by simultaneously guaranteeing a high thermal conductance. This design enables a short downtime between sample preparation and STM investigations such as basic structural investigations in constant-current mode. For example, a determination of surface impurity densities can be performed with running turbomolecular pumps as the eddy-current damping stage dampens mechanical vibrations arising from the pump rotation and sample cleaning can be resumed immediately if the purity is unsatisfactory.

A proportional-integral-derivative (PID) controlled valve allows setting a stable flow of He through the cryostat [69]. To further stabilize the temperature, the heat exchanger is equipped with a resistive heater. Using a PID controlled power supply, the heating power on the heat exchanger can be regulated to compensate for changes of the environment, for example changes in the room temperature or in the incident radiation on the heat exchanger. The temperature readout is realized by a Si diode mounted inside the heat exchanger and a GaAs/GaAlAs diode mounted inside the STM, near the sample. In thermal equilibrium, the sample temperature T_s is approximately 15 K higher than at the heat exchanger [70] and the He consumption rises drastically when the sample temperature approaches the attainable base temperature of $T_s \approx 24$ K. At $T_s = 40$ K, the liquid He consumption amounts to ca. 12.5 l per day, allowing more than two weeks of uninterrupted operation with a 250 l reservoir dewar.

The VT-STM was built by Torben Hänke, whose dissertation contains a detailed description of its assembly [70]. Figure 3.4 depicts the bare VT-STM, as it is housed inside the radiation shield. The sample is mounted upside-down inside the sample receptacle and is clamped by a CuBe spring. The tip is clamped or glued with conductive epoxy inside a tip holder. The tip holder is held inside the tip holder receptacle by a CuBe leaf spring. This assembly is embedded inside the tube scanner, which is in turn glued on a macor base. To allow an approach of the tip to the sample, the tube scanner is housed inside a sapphire prism that can be driven up and down by stick-slip motion via six shear piezo stacks. For *in-situ* tip exchange, a shuttle is inserted into the sample receptacle that holds the tip holder in position. Then, the sapphire prism can be moved downwards by the shear piezos, freeing the tip holder from the tip holder receptacle. Introduction of a tip works the other way around by insertion of the tip on a shuttle into the sample receptacle and subsequent upwards movement of the prism until the tip holder is sheathed inside the tip holder receptacle again.

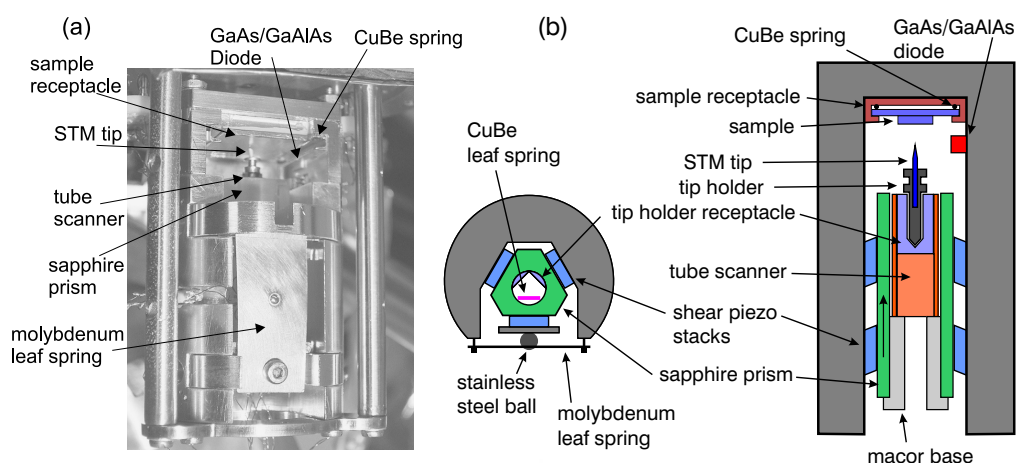


Figure 3.4: (a) Photograph of the bare VT-STM taken from [70]. (b) Schematic cross-sectional views of the VT-STM.

The VT system is well suited for structural investigations and growth studies due to the easy accessibility of the STM and the eddy-current noise damping that enable a high turnover of samples. The flow cryostat further allows experiments in a variable temperature range between 24 K and 300 K.

3.4 The low-temperature STM

The low-temperature scanning tunneling microscope (LT-STM) is designed to allow STM and STS studies at temperatures down to 1 K in an out-of-plane magnetic field of up to 3 T. A detailed description of the instrument can be found in [65]. The custom-built UHV chamber and cryostat are schematically depicted in Figure 3.5. The bath cryostat comprises two large cryogenic reservoirs: a 130 l liquid He tank and a 120 l liquid N₂ tank around it. Inside the He tank there is a pair of superconducting Helmholtz coils. This layered design ensures a holding time of one week, after which the He tank has to be refilled to keep the coils fully submerged. The STM is situated on the center axis of the Helmholtz coils where the generated magnetic field is approximately homogeneous. It is mounted on a pedestal coupled to a small liquid He reservoir of approximately 1 l, the so-called "1 K-pot". The 1 K-pot can be connected to or disconnected from the LHe tank by a valve. Pumping on the 1 K-pot lowers the boiling point of the He inside and facilitates a minimum attainable temperature of $T = 1.1$ K [71]. Alternatively, the valve between LHe tank and 1 K-pot can be opened and the system then operates at $T = 4.2$ K and atmospheric pressure. Influx of thermal radiation

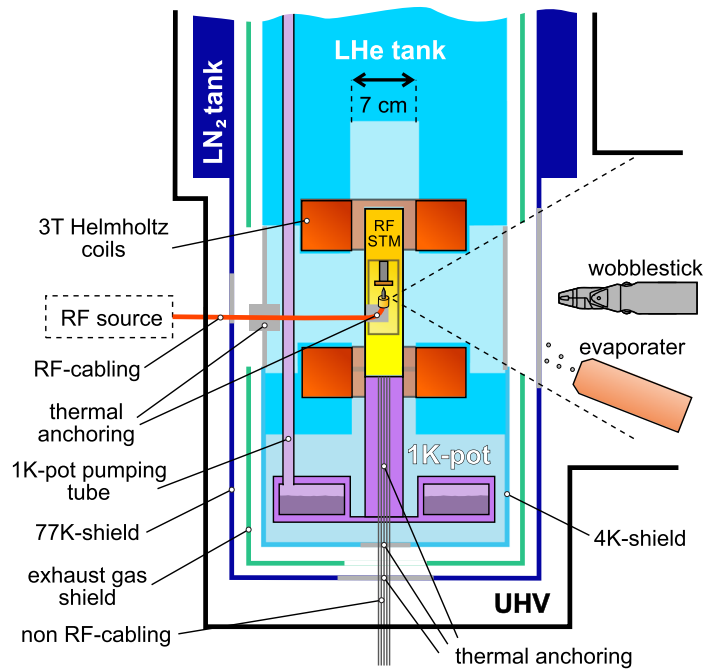


Figure 3.5: Schematic of the STM chamber of the LT system including the cryostat, the STM and the cabling. Reprinted from [71], with the permission of AIP Publishing.

onto the STM is reduced by concentric radiation shields. One shield each is mounted on the cryogenic tanks. Another shield in between is coupled to the He exhaust of the 4 K tank and additionally shields the liquid He reservoir from radiation. A coaxial radio frequency (RF) cable allows for optional application of RF signals to the tip. It is fed through the side walls of the radiation shields. The other cables, contacting the sample and the piezos inside the STM, are fed through the bottom of the cryostat. All cables are thermally anchored at the 1 K-pot, at the 4 K-shield, and at the 77 K-shield. The shields can be rotated to yield optical access to the STM and to exchange tips and samples using a wobblestick.

The STM itself is depicted in Figure 3.6. The sample is mounted on a piezoelectric tube scanner that can be moved along the vertical axis by stick-slip motion while the tip is fixed below. The reason for this is the stiffness of the semi-rigid RF cable attached to the tip that is embedded inside the STM body. The tip holder is realized by a coaxial G3PO bullet connector with a polytetrafluoroethylene (PTFE) dielectric, enabling transmission of RF ac signals to the tunnel junction. The bullet connector's inner conductor has a spring holder designed to bind to its counterpart. Likewise, tips can be inserted

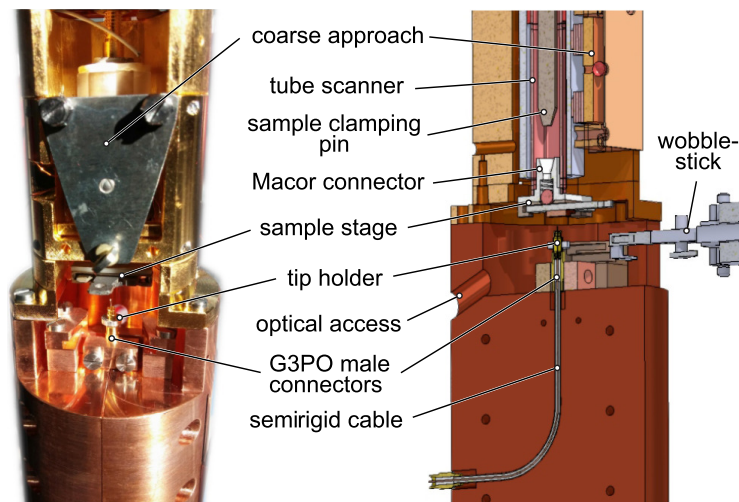


Figure 3.6: Photograph (left) and cross-sectional drawing of the LT-STM. Reprinted from [71], with the permission of AIP Publishing.

into the spring holder at one end of the connector. Tip exchange is realized by manual disconnection of the bullet connector and insertion of a new one, including a new tip, using the wobblestick.

In contrast to the VT-STM, the LT-STM is rigidly connected to the cryostat. The use of the Helmholtz coils to generate an external magnetic field excludes the implementation of an eddy-current damping stage. Instead, the whole UHV chamber system rests on four pneumatic damping pillars.

With the lower base temperature, the LT system allows the investigation of low-temperature phenomena and tunneling spectroscopy with higher energy resolution compared to the VT system. The theoretically attainable energy resolution is 0.3 meV at 1.1 K and 1.3 meV at 4.2 K. Furthermore, experiments in out-of-plane magnetic fields of up to $|B| = 3$ T are possible.

4 Physical properties of Be(0001) and ϵ -Fe

This chapter compiles the relevant physical properties of the substrate material Be(0001) and of ϵ -Fe desired to be grown on this substrate.

4.1 Electronic properties of Be(0001)

As the fourth element of the periodic table, beryllium has the atomic electron configuration $1s^2 2s^2$. It crystallizes in the hcp structure with lattice constants of $a = 228$ pm and $c = 358$ pm [24]. Bonding in the Be crystal is facilitated by hybridization of s and p bands [72–74]. Among the group II elements, Be is set apart by its peculiar electronic structure. Figure 4.1 depicts the band structure of Be(0001) theoretically derived using the pseudopotential method [75]. Shaded areas represent the projected bulk bands. The bulk electronic DOS of Be is very low in the vicinity of the Fermi level, leading to electronic bulk properties similar to semiconductors [31, 74]. In fact, the Be bulk can be viewed as a semimetal as it has a wide band gap close to the Γ -point but there are states that cross the Fermi level closer to the edges of the Brillouin zone [76–79].

The Be(0001) surface was found to behave more metallic than the bulk [34, 79] due to the presence of electronic surface states inside the partial bulk band gap [26, 27, 29], indicated by the dashed lines in Figure 4.1. Angle resolved

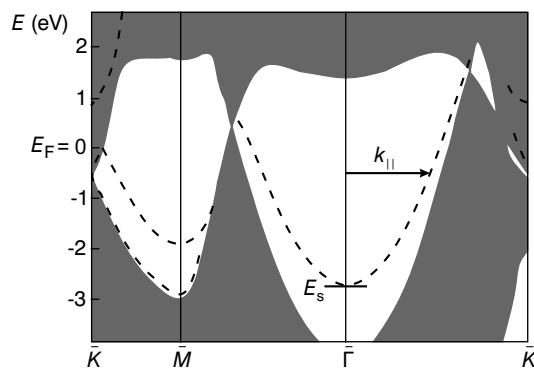


Figure 4.1: Band structure of Be(0001) calculated using the pseudopotential method. Dashed lines represent surface states. The band minimum of the $\bar{\Gamma}$ surface state E_s and its momentum parallel to the surface plane $k_{||}$ are indicated. Adapted by permission from Springer [75] © 2000.

photoemission spectroscopy (ARPES) experiments confirmed the parabolic dispersion of two surface states with band minima centered at the $\bar{\Gamma}$ and \bar{M} points, respectively [29]. The dispersion relation according to the model of nearly free electrons reads

$$E(k) = E_s + \frac{\hbar^2 k_{\parallel}^2}{2m^*}, \quad (4.1)$$

where E_s is the band minimum energy, $k_{\parallel} = \sqrt{k_x^2 + k_y^2}$ is the momentum parallel to the surface plane and m^* is the effective electron mass. E_s and k_{\parallel} are exemplarily indicated for the $\bar{\Gamma}$ surface state in Figure 4.1. The $\bar{\Gamma}$ surface state was assigned to s - p_z states and the \bar{M} surface state originates from $p_{x,y}$ states [30, 77]. According to first-principles calculations, the DOS of the $\bar{\Gamma}$ surface state is localized more strongly in the surface region compared to other metals, with 90 % of the charge of this state situated in the uppermost two atomic layers [32].

4.1.1 Theory of a 2D electron gas reflected in STM

The electronic band structure of Be(0001) has implications for STM experiments on this surface, as the STM is sensitive to the spatially resolved electronic DOS at a sample surface. The electronic surface properties of Be(0001) were found to be dominated by parabolic surface bands in photoemission experiments [26–29]. The DOS of two-dimensional surface bands with a parabolic dispersion relation will be described within the model of nearly free electrons in the following considerations.

Consider a two-dimensional unit square of width L inhabited by two states of opposite spin. The unit volume in reciprocal space will be

$$V_u = \left(\frac{2\pi}{L}\right)^2. \quad (4.2)$$

Thus, the number of states inside an area of radius k_{\parallel} reads

$$N = 2 \frac{\pi k_{\parallel}^2}{V_u} = \frac{k_{\parallel}^2 L^2}{2\pi}, \quad (4.3)$$

with the factor 2 representing both spin directions. Solving Equation (4.1) for

$$k_{\parallel} = \sqrt{\frac{2m^*}{\hbar^2} (E - E_s)}, \quad (4.4)$$

this can be inserted into Equation (4.3) and differentiation yields the two-dimensional electronic surface DOS [80]

$$\rho_{2D}(E) = \frac{dN}{dE} = \begin{cases} \frac{m^* L^2}{\pi \hbar^2} & \text{for } E > E_s \\ 0 & \text{for } E < E_s \end{cases}. \quad (4.5)$$

This means that the DOS of a parabolic band in two dimensions has a jump at the onset energy E_s and is otherwise independent of energy.

Crystal surfaces are not ideal two-dimensional planes but contain defects like atomic step edges or impurities. Electrons propagating along the surface will scatter from these impurities and be partially reflected, leading to interference and thus to an oscillatory DOS at the surface, so called Friedel oscillations [81]. Following Avouris *et al.* [82], we consider a step edge as a one-dimensional wall along y at $x = 0$ and a Bloch wave propagating along x and y with an exponentially decaying part along z . Assuming no transmission through the wall, the wave function ψ has to fulfill the condition $\psi(x = 0) = 0$:

$$\psi = c \sin(k_x x) e^{(k_y y)} e^{-\int_0^z \kappa dz}. \quad (4.6)$$

Here, c is a constant and κ describes the decay of the wave function into the vacuum along z . The number of states in dependence of energy E and distance from the step x can now be found by integration:

$$\begin{aligned} N(E, x) &= \int_{k_{||} \leq \frac{2m^*}{\hbar^2} E} |\psi|^2 dk_x dk_y \\ &\propto \frac{\pi k_{||}^2}{2} \left(1 - \frac{J_1(2k_{||}x)}{k_{||}x} \right), \end{aligned} \quad (4.7)$$

where J_1 denotes the 1st-order Bessel function. For the DOS follows

$$\rho_{2D}(E, x) = \frac{dN}{dE} \propto \left(1 - J_0(2k_{||}x) \right), \quad (4.8)$$

with the 0th-order Bessel function J_0 . Consequently, the DOS will oscillate in the vicinity of a step edge with the wave number $q = 2k_{||}$. The spatial decay of the oscillations is slow with the amplitude asymptotically falling off proportional to $x^{-1/2}$ [82]. In constant-current mode for low bias voltages, the STM images contours of constant DOS and consequently Friedel oscillations can be mapped.

4.1.2 Previous STM investigations of Be(0001)

Previously, STM experiments in constant-current mode were conducted on Be(0001) [37], as well as on Be(10 $\bar{1}$ 0) [83, 84]. These experiments revealed pronounced charge density oscillations on these surfaces near defects for sample bias voltages within $|U| \leq 400$ mV. Surface states were identified as the cause for these oscillations, as the oscillations' wave vector q matches twice the Fermi wave vector k_F [37, 84] (cf. Equation (4.8)). A striking observation was the enhancement of the oscillations' amplitudes on Be(0001) when the bias approaches zero, increasing from 4.2 pm at $U = -35$ mV to 42 pm at $U = -2.1$ mV [37]. This strong bias dependence contradicted the simple interpretation as Friedel oscillations of surface state electrons. For the parabolically dispersing $\bar{\Gamma}$ surface state, a negligible bias dependence would be expected since the DOS for such a state in 2D has only a weak energy dependence (see Equation (4.5)) [37]. A CDW was proposed as a possible cause for this bias dependence of the oscillation amplitude [37]. Transitions to a CDW state are often accompanied by the formation of a band gap at the Fermi level [85]. But Hengsberger *et al.* excluded the existence of a band gap wider than 4 meV at the Fermi level in Be(0001) for $T > 12$ K through ARPES experiments [41, 86].

Furthermore, strong coupling of the Be(0001) surface state to phonons was put forward as a possible explanation for the enhanced amplitudes observed near the Fermi level [37]. The underlying physical mechanism in this case would be the renormalization of the surface state dispersion, flattening the band inside the energy range of the phonon bandwidth around the Fermi level and thus enhancing the electronic DOS in this range [87]. The electron-phonon interaction in Be(0001) was intensively studied theoretically [78, 79, 88, 89], as well as experimentally involving ARPES [76, 90, 91]. Indeed, the electron-phonon coupling was found to be strong in Be(0001), especially for surface phonons, with mass enhancement factors of $\lambda = 0.7$ [79, 88, 90] to $\lambda = 0.94$ [76]. The phonon bandwidth of Be is approximately 80 meV [76, 92].

Ultimately, the origin of the deviations of standing electron waves as observed in STM on Be(0001) from the picture of Friedel oscillations remains an open question. This thesis aims at resolving this question by spectroscopic characterization of the Be(0001) surface using STS.

4.2 Physical properties of the high-pressure ϵ -phase of Fe

The bcc ground state of Fe is energetically favored over close-packed configurations due to ferromagnetic interactions [16, 93]. In the pressure range of 13.5 GPa-15.7 GPa, a loss of ferromagnetic order in Fe was detected using Mössbauer spectroscopy [94], and x-ray magnetic circular dichroism [18]. This magnetic transition is accompanied by a first-order structural phase transition to ϵ -Fe with an hcp structure [18, 95]. In the course of this transition, the lattice constants change from $a = 287$ pm in the bcc-phase to $a = 245$ pm and $c = 393$ pm in the hcp-phase [14].

Experimentally, the magnetic state of ϵ -Fe was investigated in diamond anvil cells. Macroscopically, the magnetic moment vanishes in ϵ -Fe [96]. Mössbauer spectroscopy in external magnetic fields ruled out the existence of magnetic moments of $> 0.05\mu_B$ in the material at 20 GPa [19]. However, DFT calculations predict a higher stability for spin-polarized states with antiferromagnetic order compared to a non-spin-polarized configuration [21, 22]. One of these states consists of antiferromagnetically coupled planes stacked along the c -axis with in-plane magnetization. In the other, the planes of parallel spins lie perpendicular to the [2110] direction [21]. Furthermore, an incommensurate spin spiral of $q = 2\pi/a(0.56, 0.22, 0)$ was motivated using first-principles calculations as another possible ground state, degenerate in energy with the antiferromagnetic configurations [23]. The magnetic moments of all these configurations were estimated to approximately $1 \mu_B$ [23], which is in contradiction to the Mössbauer result [19].

Canceling polarizations of core electrons and valence electrons in an antiferromagnetic state were proposed as a mechanism preventing the detection of hyperfine fields in Mössbauer spectroscopy [97]. Possible fast spin fluctuations in the magnetically frustrated hcp lattice pose an alternative explanation for this discrepancy [20]. Spin fluctuations were also proposed as an unconventional driving mechanism behind the superconducting transition in ϵ -Fe [98, 99] with a critical temperature of approximately 2 K [100].

While there is a broad consensus that ferromagnetic order is lost in the bcc to hcp transition, the magnetic state of hcp ϵ -Fe remains unclear. Spin-polarized scanning tunneling microscopy is a viable tool to search for indications of antiferromagnetic or non-collinear magnetic order on the surface of a compressed Fe-film, provided the ϵ -phase of Fe can be stabilized on a hexagonal substrate like Be(0001).

5 Preparation of the clean Be(0001) surface

A prerequisite for STM investigations of crystal surfaces is the ability to routinely clean the surface of interest. On the one hand, insufficient surface purity can impair the stability of STM and STS measurements through frequent adsorption of impurities onto the tip. On the other hand, impurities can change the electronic surface properties of tip and sample and thus impede the interpretation of experiments. This chapter provides an overview of the material properties of Be relevant for preparing a clean surface. Starting from procedures previously used in photoemission and electron diffraction measurements, a refined cleaning procedure yielding a Be(0001) surface suitable for STM experiments is presented. The experimental refinement of the cleaning procedure was conducted in the VT system because of its efficient turnover of samples discussed earlier. The reproducibility of this sample preparation was then verified in the LT system.

5.1 The beryllium crystals

The first step in preparing single crystal surfaces for STM experiments is usually mechanical polishing, or — in the case of layered materials — cleaving. Polished single crystals of most elemental metals are commercially available. However, there are elaborate regulations concerning the handling and distribution of Be because of its toxicity and its application in nuclear reactors [101, 102]. This is the reason for the limited commercial availability of Be and its compounds [101]. For example, standard providers of already polished single crystals like MaTecK or Alfa Aesar do not distribute Be crystals.

The hazard of handling Be lies in the toxicity of its vapor or dust particles smaller than 10 μm in diameter [102, pp. 499, 103]. If inhaled, those particles can deeply penetrate the lungs and cause chronic berylliosis, also known as chronic beryllium disease (CBD), a lung disease similar to asbestosis [101, 102, 104]. Because of this, equipment used to machine beryllium has to be thoroughly decontaminated afterwards, which leads to higher prices for cutting or polishing Be compared to other metals.

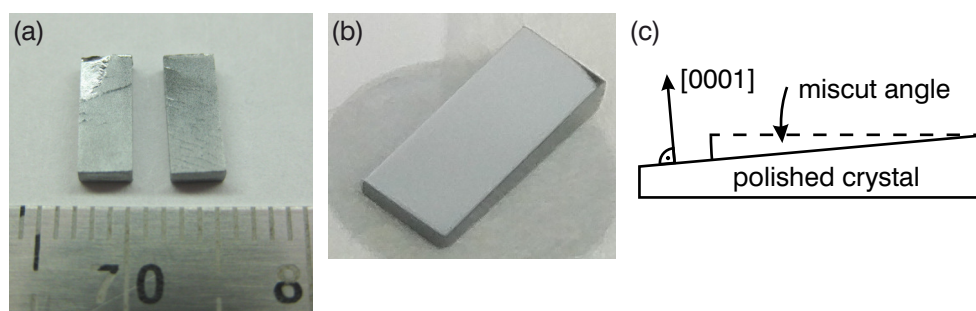


Figure 5.1: Photographs of the Be crystals studied in this work. (a) Crystals as received from the manufacturer Materion. (b) One crystal after correction of a surface miscut of 5.0° and polishing to a roughness $R_a < 0.03 \mu\text{m}$ by SPL. (c) Schematic side view of the crystal after polishing, showing the orientation of the polished surface and the miscut angle.

The crystals used in this study are depicted in Figure 5.1 (a) as received from the manufacturer Materion¹. They measure $3 \text{ mm} \times 7 \text{ mm}$ and were cut from an ingot by spark erosion. After that they were milled down to their thickness of approximately 1.4 mm . Evidently, their surfaces are macroscopically rough. The samples were then polished to a mirror finish with a roughness of $R_a < 0.03 \mu\text{m}$ by SPL². The result is depicted in Figure 5.1 (b). The polished crystals are not cuboid anymore but shaped like wedges. A schematic side view is provided in Figure 5.1 (c). The reason of this shape is a misalignment of the original crystal surface with respect to the (0001) surface. The miscut angles of the original crystals was determined to 4.5° and 5.0° , respectively, by SPL using Laue diffraction and corrected in the polishing process.

5.2 Previously established *in situ* cleaning procedures for Be surfaces

Mechanical polishing under ambient conditions can not produce atomically flat surfaces free of contaminants. For the best possible surface quality, further *in situ* preparation under UHV conditions has to be carried out. In the past, Be(0001) was investigated experimentally under UHV conditions for example by LEED, AES, and ARPES. In this section, the reported preparation techniques used in previous studies and the relevant material properties of Be(0001) will be discussed.

Beryllium is an alkaline-earth metal that is highly reactive with oxygen and

¹Materion Corporation, 6070 Parkland Blvd., Mayfield Heights, OH 44124, USA.

²Surface Preparation Laboratory B.V., Penningweg 69 F, 1507 DE Zaandam, The Netherlands.

water and thus readily builds an oxide layer in atmosphere. This layer protects the crystal bulk from further oxidation and its reported thickness ranges from five atomic layers [105] to 100 Å [106]. Common impurities in Be are C and Si [84, 107–109]. A common approach for *in situ* impurity depletion of single crystals is annealing in oxygen atmosphere in order to oxidize impurities (as for example C atoms) and subsequently desorb them at high temperatures. In the case of beryllium, this approach has small prospects of success because of beryllium's high reactivity. In addition, the oxide layer is only protective up to $\sim 700^\circ\text{C}$ [110] and higher temperatures under O_2 could lead to sustained oxidation of the crystal.

High temperature annealing in vacuum at $T \geq 1000^\circ\text{C}$ alone was sufficient to obtain clear hexagonal LEED patterns of the Be(0001) surface [39, 111]. However, mass spectrometry showed that this is not achieved by desorption of the oxide layer, but by diffusion of Be from the crystal bulk to the surface [112]. Another drawback of this method is the surface degradation of Be(0001), associated with its low melting point [39, 113].

In early LEED experiments, the Be(0001) surface was cleaned by sputtering with 1 keV Ar^+ ions and subsequent annealing to 750°C . This procedure produced hexagonal LEED patterns [39, 111]. AES measurements showed that simple cycles of sputtering at room temperature and subsequent annealing leave traces of C and O impurities on the surface [40, 109]. The residual oxygen contamination can be explained by promotion of impurities from the bulk to the surface during annealing [114]. Sputtering at elevated temperatures of 550°C - 800°C was successfully used to reduce the density of such surface contaminants [29, 40, 41, 115, 116]. In the following, the impact of the annealing temperature during and after sputtering on the surface quality is presented.

5.3 Refined sputter cleaning of Be(0001) for STM experiments

To refine cleaning procedures used previously in scattering experiments for STM experiments on pristine Be(0001), and also later for Fe films grown on this surface, demands on surface quality have to be formulated. First, the study of thin film growth, and even more so of surface magnetic properties, requires substrate terraces of sufficient width. The minimum size of terraces required is dictated by the growth mode and the size of magnetic domains. Terraces should be large enough to allow the study of surface relaxation in adlayers without the interference of boundary conditions set by substrate step edges. For magnetic

adlayers they are desired to be large enough to allow an observation of magnetic domains without a direct influence of step edges. In case of the well studied hexagonal surface Ir(111) for example, terraces of several tens of nanometers in width are sufficient to study the effect of lattice mismatch between the substrate and the Fe adlayers on the growth mode, and the nanoscale magnetism in dependence of local coverage [4, 6, 7].

Second, the terraces should preferably be free of lattice defects. To study the electronic properties of Be(0001), the surface should be uniform over an area large enough to observe the unperturbed spatial evolution of standing electron waves [37]. Moreover, the surface should be depleted of individual atomic-size impurities. The formation of a depletion zone near the surface is especially important for the goal of growing Fe adlayers on the Be(0001) substrate as smooth epitaxial growth of Fe films on metallic substrates often requires annealing of the sample during or after Fe deposition [117]. The annealing temperature may result in the recontamination of a surface by promotion of impurities from inside the crystal bulk onto the previously clean surface.

5.3.1 Interdependence of preparation parameters

The relevant parameters for sputter cleaning are the acceleration energy of the Ar^+ ions E_{Ar} , the pressure of the Ar gas p_{Ar} , and the sample temperature T during sputtering and after sputtering. A higher energy or pressure will generally inflict more damage on the sample surface and consequently a higher temperature or longer annealing time will be necessary to restore the surface. Simultaneously, higher temperatures will promote more impurities from the crystal bulk to the surface. With the right set of parameters, cycles of sputtering and annealing may lead to a decreasing impurity concentration in the surface layers of the crystal. Briner *et al.* reported to limit the annealing of Be(10 $\bar{1}$ 0) to "flashes" up to 630 °C for subsequent STM experiments in order to limit the promotion of bulk impurities to the surface [84]. This was at the expense of long-range ordering as indicated by LEED [84].

The Be(0001) sample was initially prepared by several cycles of Ar^+ -sputtering for 1 h ($E_{\text{Ar}} = 2 \text{ keV}$, $p_{\text{Ar}} = 8 \times 10^{-6} \text{ mbar}$) in the VT system using a SPECS IQE 11/35 ion gun and subsequent annealing to $T \leq 660^\circ\text{C}$ for 1 h. Figure 5.2 shows an STM image of the surface after this procedure. Step edges on the sub-nanometer scale can be identified as expected for a polished and annealed crystal surface. Heaps of impurities a few nanometers in diameter can be seen on the surface that obviously act as nucleation sites for step edges during the annealing. Holes in the surface that usually result from the sputtering are closed superficially but there are many screw dislocations and warping areas on the

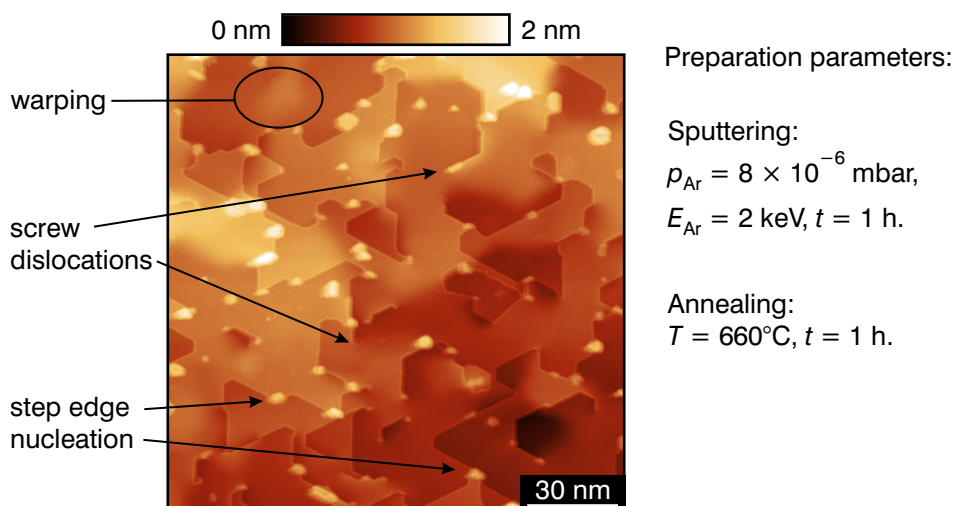


Figure 5.2: Constant-current STM image of Be(0001) after 1 h of Ar^+ sputtering with $E_{\text{Ar}} = 2$ keV, $p_{\text{Ar}} = 8 \times 10^{-6}$ mbar and annealing at $T = 660^\circ\text{C}$ for 1 h as the final cleaning step. Many screw dislocations are evident, indicating insufficient annealing. Experimental parameters: $I = 100$ pA, $U = 400$ mV, $T = 60$ K, Cr tip.

surface that indicate insufficient annealing. In this case, the final annealing of 1 h at 660°C was not suitable to produce a smooth surface of low defect density.

An example of better balanced sputtering and annealing parameters is given in Figure 5.3 (a). A similar annealing temperature of $T = 650^\circ\text{C}$ held for 1 h was sufficient to remove dislocations inflicted by the softer and shorter sputtering with lower ion energy and lower pressure ($E_{\text{Ar}} = 1$ keV, $p_{\text{Ar}} = 4 \times 10^{-6}$ mbar, $t = 30$ min). As a result, terraces of parallel orientation have formed. The caveat of this preparation is a high density of atomic-scale impurities on the surface, depicted in Figure 5.3 (c). This illustrates the difficulty of minimizing different kinds of detrimental defects simultaneously: lattice defects and atomic-scale impurities.

Following the approach of sputtering at elevated temperatures previously employed in photoemission experiments [41, 115], the impurity density could be decreased by sputtering for additional 10 min at a reduced pressure of $p_{\text{Ar}} = 1.7 \times 10^{-6}$ mbar and $T \approx 500^\circ\text{C}$. The resulting surface is shown in Figure 5.3 (b). Indeed, the density of atomic scale impurities D_i is significantly reduced by an order of magnitude from 2.7 nm^{-2} to 0.3 nm^{-2} . However, domed features have emerged in the surface as can be seen in the line profiles depicted in Figure 5.3 (d). Such features were observed before in STM on Al(111) [118] and by transmission electron microscopy of Be [119]. They originate from three-dimensional bubble defects below the surface caused by gas implantation,

5 Preparation of the clean Be(0001) surface

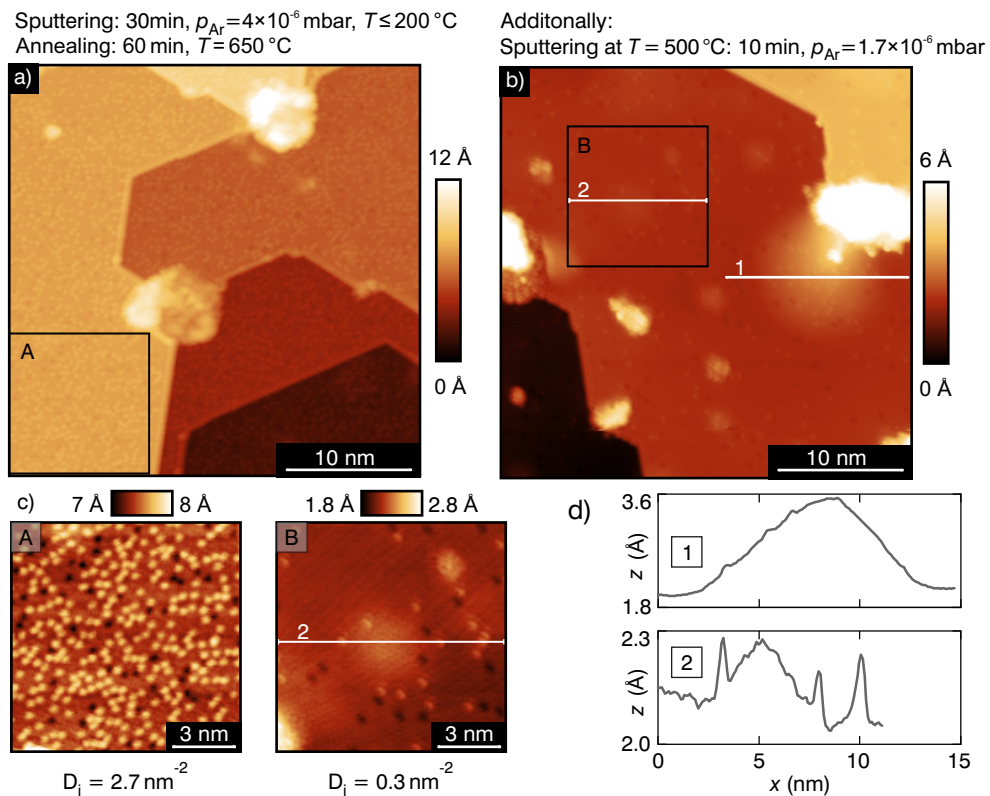


Figure 5.3: Constant-current STM images of the sputter-annealed Be(0001) surface. (a) The sample surface after a final preparation step of 30 min of sputtering ($E_{\text{Ar}} = 1 \text{ keV}$, $p_{\text{Ar}} = 4 \times 10^{-6}$ mbar, $T \leq 200^\circ\text{C}$) and subsequent annealing at $T = 650^\circ\text{C}$ for 1 h. (b) The same sample after additional 10 min of sputtering ($E_{\text{Ar}} = 1 \text{ keV}$, $p_{\text{Ar}} = 1.7 \times 10^{-6}$ mbar) at $T \approx 500^\circ\text{C}$. Experimental parameters: $I = 1 \text{ nA}$, $U = 200 \text{ mV}$, $T = 60 \text{ K}$, Cr tip. (c) Magnified details of the images above. The respective impurity densities D_i are indicated. (d) Line profiles showing the extent of warping areas in (b).

in this case Ar implantation during sputtering.

Hence, sputtering and annealing treatments both create surface defects, the removal of which requires the other treatment. This interdependence is described in Figure 5.4. Impurities or even oxide layers on the surface have to be removed by sputter cleaning. This can succeed but inevitably induces defects in the surface and leaves Ar atoms embedded below it. Annealing of the sputter damage requires heating of the crystal to high temperatures, which in turn promotes impurities to the surface. The removal of impurities requires further sputtering, which closes the circle. To make Be(0001) a suitable surface for STM experiments, a cleaning procedure has to be established that reproducibly minimizes sputter defects and impurities simultaneously.

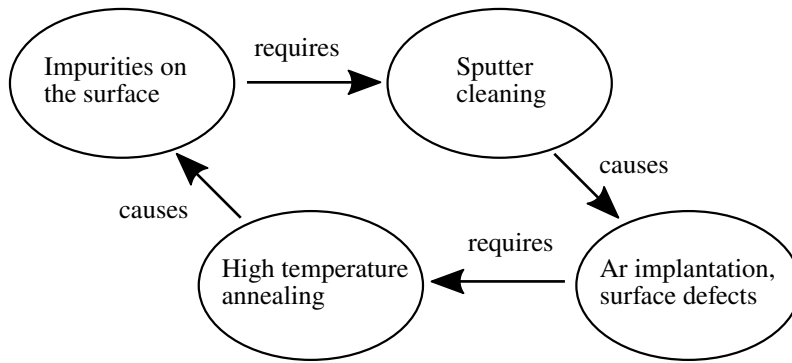


Figure 5.4: Schematic depiction of the problem of sputter cleaning the surface of a crystal with mobile impurities in the bulk.

In order to achieve large, defect-free surface areas with low impurity density, the cleaning procedure is split up into two separate steps as schematically depicted in Figure 5.5. The goal of the first step is to erase the oxide layer from the surface after the crystal was exposed to atmosphere, or to erase Fe adlayers deposited in previous experiments. This is done by cycles of "rough" sputtering with Ar^+ energies of 1 keV-2 keV and subsequent annealing of the sputter damage at relatively high temperatures. As a consequence of the high temperature, mobile impurities are promoted to the surface. To break the vicious circle outlined in Figure 5.4, a second, "soft" sputtering step is introduced. Here, the sputter energy and intensity has to be matched with the sample temperature to continuously remove impurities from the surface as they emerge without introducing too many sputter defects. The optimization of the relevant preparation parameters to yield a clean Be(0001) surface as the basis for sophisticated experiments is shown in the following.

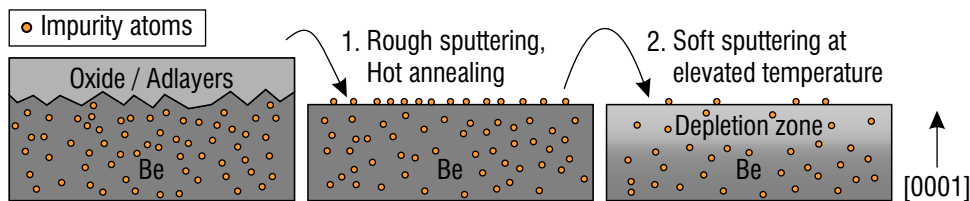


Figure 5.5: Schematic of surface preparation in two steps: 1. removal of adlayers from the crystal surface and 2. creation of an impurity-depleted zone on and below the surface.

5.3.2 Preparation step one: The influence of the annealing temperature

The mean terrace width of a single crystalline surface is basically dictated by the surface miscut. In case of the (0001)-surface that is the deviation of the surface normal from the [0001]-direction. However, the maximum size of terraces found on a surface depends on the crystal preparation procedure. Figure 5.6 (a) depicts an STM image of the Be(0001) surface after preparation by cycles of sputtering and subsequent annealing to a maximum temperature of $T_{\max} = 660^{\circ}\text{C}$. The result is a surface of terraces with parallel orientation. However, this surface is peppered with clustered impurities that likely act as nucleation sites for Be terraces during annealing. The numerous nucleation sites for edges lead to comparably small terraces.

For comparison, the surface after a similar preparation procedure with $T_{\max} = 810^{\circ}\text{C}$ is shown in Figure 5.6 (b). The higher temperature leads to larger but fewer impurity clusters, typically some nanometers in height. Coincidentally, the distribution of terrace widths has changed. Notably larger terraces and larger areas free of impurity clusters are created in the process. Also between

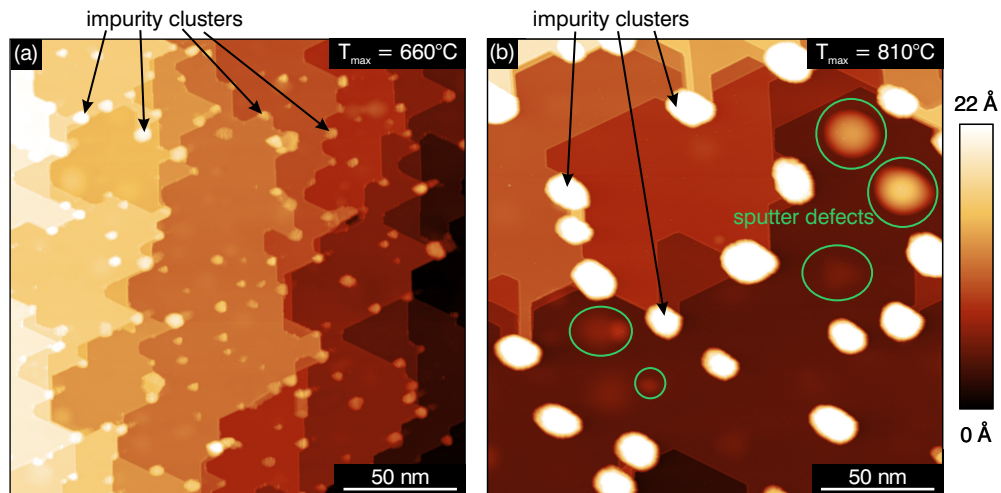


Figure 5.6: Influence of the annealing temperature on the distribution of terrace width and residual impurities. Constant-current STM images of the Be(0001) surface after several cycles of Ar^+ sputtering with $E_{\text{Ar}} = 2 \text{ keV}$ and a maximum annealing temperature T_{\max} of (a) 660°C and (b) 810°C , respectively, are shown. Impurity clusters that act as nucleation sites for step edges and bubble defects resulting from sputtering are exemplarily marked. Experimental parameters: (a) $I = 100 \text{ pA}$, $U = 400 \text{ mV}$, $T = 60 \text{ K}$; (b) $I = 100 \text{ pA}$, $U = 600 \text{ mV}$, $T = 40 \text{ K}$, Cr tip. The sample depicted in (b) was prepared and investigated together with Jan-Hendrik Schmidt [66].

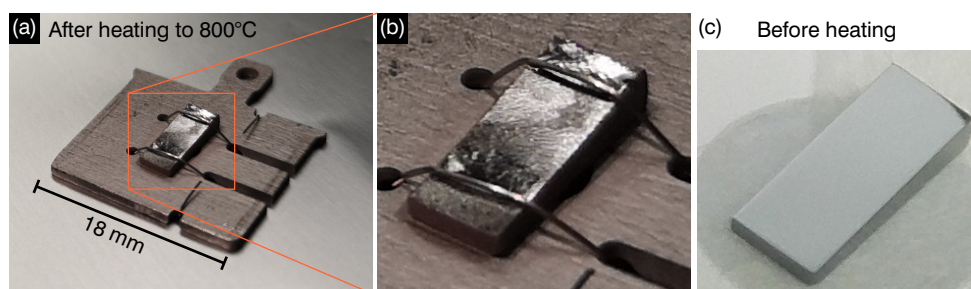


Figure 5.7: Photographs of a Be crystal after several sputter-anneal cycles with temperatures up to ca. 800 °C. (a) The crystal is bound onto a W sample plate using W wire. (b) Magnified view of the crystal showing a roughening of the surface. (c) A photograph of the polished crystal surface before heating for comparison.

warping areas, originating from subsurface sputter defects, distances of tens of nanometers are found in some instances.

In both cases, step edges run along directions of sixfold symmetry, in accordance with the symmetry of the Be(0001) surface. Interestingly, the step edges avoid forming acute external angles. Narrowing terraces will always end on an impurity. This can be explained by the lowered coordination number of Be atoms at external angles compared to internal angles. The surface morphology seen in Figure 5.6 (b) is preferable because it leaves larger areas unperturbed by defects and the STM enables selective studies of these areas.

Substantially higher temperatures than $\sim 800^\circ\text{C}$ were avoided because already at this temperature prolonged annealing causes a macroscopic roughening of the surface. The vapor pressure of Be at 800°C is on the order of 1×10^{-7} mbar [120, 121], so that evaporation from the crystal surface can be expected. This is supported by the observation of a steadily increased pressure inside the UHV chamber to 8×10^{-9} mbar during annealing at 800°C compared to the chamber's base pressure below 2×10^{-10} mbar. Another reason for a limitation of the temperature is the detrimental effect of high temperatures on the macroscopic surface morphology of the crystal. Photographs of a Be crystal that underwent several sputter-anneal treatments at temperatures up to ca. 800°C , bound to a W sample plate, are shown in Figure 5.7. A faceting of the surface and an increased roughness compared to the freshly polished surface in Figure 5.7 (c) is evident.

5.3.3 Preparation step two: Minimization of the impurity density

Unfortunately, the high annealing temperatures necessary to create extended flat Be(0001) terraces promote many impurities of atomic size from inside the crystal to the surface [114], as was observed in Figure 5.3 (a). To reduce their density on the surface, sputtering at elevated temperatures is introduced as a second preparation step after the first rough step erased oxide layers formed in atmosphere or adlayers deposited in previous experiments. Ideally, the parameters in this final cleaning step are to be matched, so that impurities can be promoted to the surface during sputtering from a zone below the surface at a sufficient rate, while continued sputtering leads to a depletion of impurities in this zone. Between the parameters there are interdependencies. The sputter yield should be high enough to erase impurities from the surface at a similar rate as they are promoted to the surface at a given temperature. Higher sputter energies, however, will lead to deeper implantation of Ar into the surface and consequently to bubble defects as seen in Figure 5.3 (b). Lastly, a sputter yield that is too high will lead to an erosion of the surface region that is faster than the temperature-driven impurity promotion, with the consequence that the impurity density on the surface will not significantly decrease during prolonged sputtering.

The parameter space for optimization is vast and multi-dimensional. But some considerations can be made to identify a promising subspace. First of all, this cleaning step should ideally only affect the top surface layer. The sputter ion energy can thus be lowered to limit the penetration depth of the Ar⁺ ions. The lower ion energy will lead to less severe subsurface implantation of Ar. Consequently, a lower temperature than the 800°C needed to create extended terraces should suffice to heal the sputter damage inflicted during this second step. Finally, with a fixed set of energy and temperature, the Ar pressure and the duration of this sputtering process can be varied to optimize the impurity density.

A summary of the tested parameters E_{Ar} and p_{Ar} in the temperature range $550^\circ\text{C} \leq T \leq 660^\circ\text{C}$ is compiled in Figure 5.8. An ion energy of $E_{\text{Ar}} = 300$ eV was found to be sufficient to reduce the surface impurity density in this temperature regime. The insets in Figure 5.8 compare the impurity densities on the Be(0001) surface after two such sputter treatments. One trial with only $E_{\text{Ar}} = 200$ eV (right) did not result in a reduction of the surface impurity density over the course of 60 min. The combination of $E_{\text{Ar}} = 300$ eV and a reduced Ar pressure (left) led to a significantly reduced impurity density. The reason for the different performance could be either a sputter yield that is overall too high at

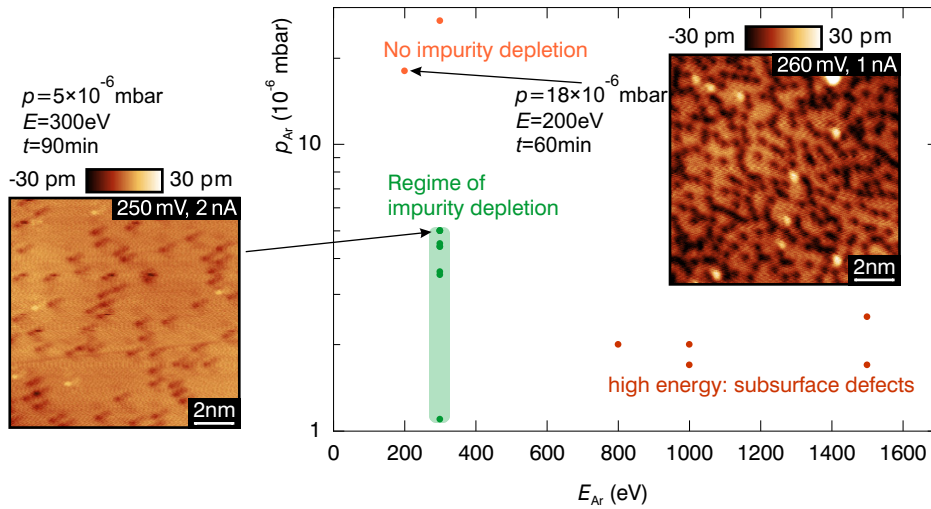


Figure 5.8: Summary of the investigated parameter pairs $[E_{Ar}, p_{Ar}]$ for impurity depletion in the temperature range $550^{\circ}\text{C} \leq T \leq 660^{\circ}\text{C}$. The scaling of the vertical axis is logarithmic. Exemplary STM images acquired at $T = 60\text{ K}$ for successful (left) and unsuccessful (right) impurity reduction are shown.

the increased pressure or a change in the preferentially sputtered atom species between $E_{Ar} = 200\text{ eV}$ and $E_{Ar} = 300\text{ eV}$.

In the following, the ion energy was fixed to 300 eV for further optimization of the cleaning procedure. An impurity depletion was achieved in the pressure range $(1.1 \times 10^{-6} - 5 \times 10^{-6})\text{ mbar}$, leading to ion currents of $(0.2 - 1.2)\ \mu\text{A}$. A combination of $E_{Ar} = 300\text{ eV}$ and $T = 580^{\circ}\text{C}$ was found to decrease the density of atomic-size impurities on the surface.

The evolution of the surface impurity density throughout this cleaning procedure is documented in Figure 5.9. Figure 5.9 (a) depicts a constant-current STM image of the Be(0001) surface after completion of the first cleaning step, ending with an annealing to a temperature of 650°C . A dense decoration with impurities is evident. An impurity density of $D_i = 1.9\text{ nm}^{-2}$ was counted. Introduction of a second, softer sputtering step for 1.5 h leads to a significantly reduced density of impurity atoms of $D_i = 0.5\text{ nm}^{-2}$, shown in Figure 5.9 (b), despite the higher annealing temperature of 800°C after the rougher sputtering. Lastly, the impurity density converges to $D_i = 0.1\text{ nm}^{-2}$ after 4 h of soft sputtering with $p_{Ar} = 5 \times 10^{-6}\text{ mbar}$ and $E_{Ar} = 300\text{ eV}$ at $T = 580^{\circ}\text{C}$, as depicted in Figure 5.9 (c). Here, also a standing wave pattern emanating from a step edge on the right edge of the image becomes visible. The impurities appear with different apparent diameters in the three images because different STM tips were used. The structures observed in constant-current STM images represent

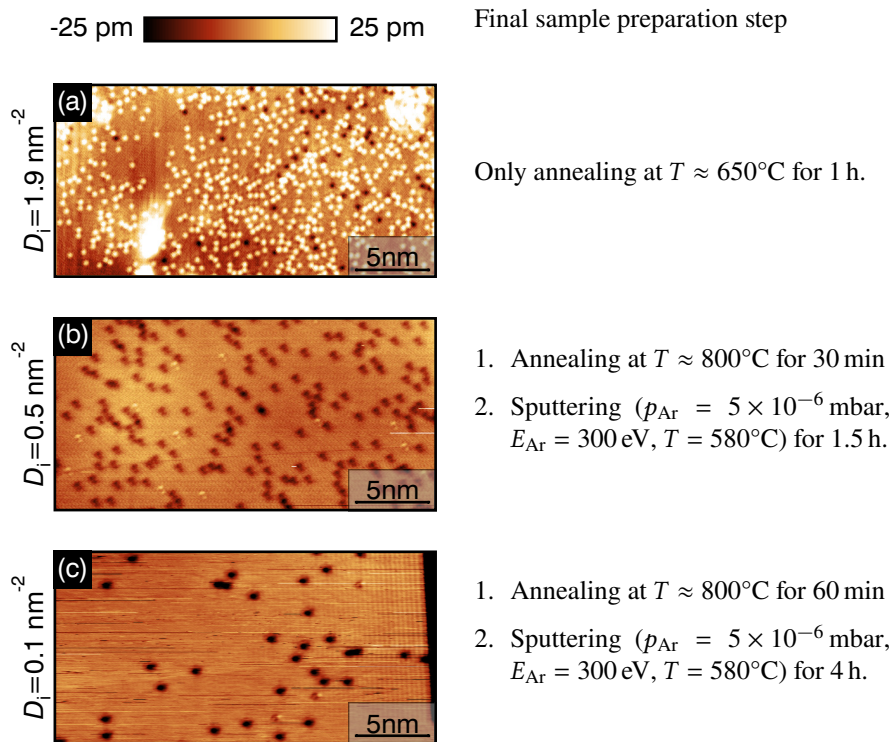


Figure 5.9: Constant-current STM images of Be(0001) showing the impurity density D_i for differently terminated cleaning procedures. (a) Typical impurity density on the surface after annealing. (b) The number of impurities is significantly reduced by soft sputtering at elevated temperatures for 1.5 h. (c) Extending the sputtering at elevated temperatures to 4 h improves the surface quality further. Experimental parameters: $T = 60$ K; (a) Cr tip, $I = 1$ nA, $U = 100$ mV; (b), (c) Pt/Ir tip, $I = 2$ nA, $U = 50$ mV.

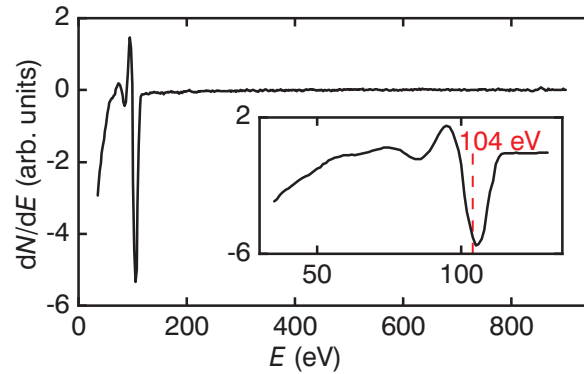


Figure 5.10: Auger spectrum of clean Be(0001) acquired with $E_p = 3$ keV, $I_p = 30$ mA, and $U_{\text{mod}} = 5$ mV. A single negative peak at 105 eV is the only distinguished peak in the spectrum. The inset depicts a higher-resolution spectrum acquired in the energy range around the peak. The literature value of 104 eV for the characteristic Be peak position is marked in red [60].

a convolution of the tip shape and the sample surface. Consequently, a blunter tip will lead to a smearing of the imaged impurities.

The success of the cleaning procedure was further verified by AES. An Auger spectrum acquired on a Be(0001) sample that was sputter-cleaned for $t > 4$ h with above-mentioned parameters is shown in Figure 5.10. A single peak at $E = 105$ eV is observed, in agreement with the literature value of 104 eV [60]. Peaks of Ar, C, or O, commonly observed in reference spectra [60], are not discernible in the spectrum. This demonstrates the quality of such-prepared Be(0001) surfaces

In conclusion, a reliable cleaning procedure to produce high-quality Be(0001) surfaces for STM investigations was developed in the VT system. The cleaning procedure consists of

1. Multiple cycles of rough sputtering and annealing, consisting of
 - a) Ar^+ sputtering with $p_{\text{Ar}} \leq 2 \times 10^{-5}$ mbar, $E_{\text{Ar}} = 1$ keV – 2 keV at room temperature for 30 min,
 - b) Annealing at $T \approx 800^\circ\text{C}$ for 1 h.
2. Softer Ar^+ sputtering with $p_{\text{Ar}} \leq 5 \times 10^{-6}$ mbar, $E_{\text{Ar}} = 0.3$ keV at $T \approx 580^\circ\text{C}$ for a minimum of 4 h.

5.3.4 Reproducibility in the low-temperature system

The reproducibility of the developed preparation routine was tested in the LT system. Because of a different sputter ion gun (SPECS IQE 12/38) equipped on

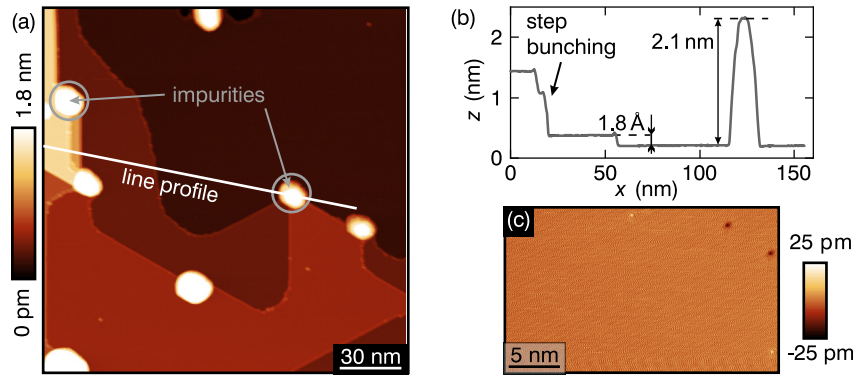


Figure 5.11: Preparation of Be(0001) in the LT system. (a) Overview STM image of the surface acquired in constant-current mode. Clusters of impurities act as nucleation sites for step edges. Parameters: $T = 4.2$ K, $I = 100$ pA, $U = 1.4$ V, Cr tip. (b) Line profile along the line indicated in (a). (c) Constant-current STM image of a single terrace showing the low density of atomic scale impurities. Parameters: $T = 4.2$ K, $I = 1$ nA, $U = 50$ mV, W tip.

this system with an integrated Ar valve close to the filament, the Ar pressure was limited to $p_{\text{Ar}} \leq 4 \times 10^{-7}$ mbar. The resulting incident ion current measured at the sample, however, was only reduced to $0.8 \mu\text{A}$ compared to $4 \mu\text{A}$ in the VT lab with $p_{\text{Ar}} = 2 \times 10^{-5}$ mbar.

Figure 5.11 (a) shows an overview STM image of the Be(0001) surface prepared in the LT system using the refined two-step cleaning procedure. Again, extended terraces can be seen in between impurity clusters. The graph in Figure 5.11 (b) shows a line profile across step edges and a large impurity cluster. The cluster appears with a corrugation of 2.1 nm. Such impurities were observed independently on two different crystals in two experimental UHV systems with base pressures below 2×10^{-10} mbar. Consequently, it appears probable that these impurities originate from contaminations in the original crystal material as for example carbon. With the generally lower sputter yield of C compared to Be [122], sputtering could lead to an enrichment of these contaminants at the surface. The evaporation of Be during high temperature annealing may also play a role in the concentration of intrinsic impurities with lower vapor pressure.

A single atomic step in the Be(0001) surface of 1.8 \AA is measured in Figure 5.11 (b) in agreement with the literature value of $c_{\text{Be}}/2 = 1.79 \text{ \AA}$ [24]. Nucleation of steps at the large impurity clusters leads to occasional step bunching of, for example, six consecutive steps in direct succession, also visible in Figure 5.11 (b).

Figure 5.11 (c) depicts a higher resolution STM image of the surface showing the low impurity density. An area of $10 \text{ nm} \times 10 \text{ nm}$ appears completely free of impurities. The low impurity density achieved in the LT system shows the

reproducibility of the developed cleaning procedure applied to different crystals across different laboratories. The only adaption made in the LT system was a lower Ar pressure due to the different sputter ion gun used there. Important for the success of the procedure is a sufficient annealing temperature of $T \approx 800^\circ\text{C}$ in the first step to properly heal sputter damage. In the second step, a low energy of $E_{\text{Ar}} = 0.3 \text{ keV}$ for preferential sputtering of impurities at $T \approx 580^\circ\text{C}$ is important. If no impurity depletion is observed in the second step, the ion beam intensity has to be lowered by variation of the Ar pressure. The resulting surface morphologies and impurity densities for well balanced parameters are satisfactory for further STM investigations of Be(0001).

6 Characterization of the Be(0001) surface by STM and STS

The investigation of iron adlayers on Be(0001) requires well defined experimental conditions in terms of substrate morphology and electronic structure. In this chapter, a characterization by means of STM and STS of the Be(0001) surface, prepared as described above, will be presented. The atomic lattice is identified in high resolution STM data, which ascertains the surface orientation. STS results are interpreted with respect to the band structure of Be(0001). Especially the influence of surface states will be explored in conjunction with phononic excitations. Parts of this study were published in Physical Review B [123].

6.1 Be(0001) imaged on the atomic scale

The detailed characterization of Be(0001) begins with STM at low bias voltages. Figure 6.1 displays high resolution STM images of a Be(0001) surface acquired under different experimental conditions together with their FFT. In Figure 6.1 (a) the hexagonal atomic lattice is resolved on pristine Be(0001). The FFT shown in the inset reveals six bright spots, corresponding to the reciprocal lattice. In the vicinity of impurities, a pattern of standing waves additionally appears on the surface as seen in Figure 6.1 (b). It is the interference pattern in the surface electronic DOS as a consequence of scattering from impurities as described in section 4.1.1. The wave pattern is reflected in the FFT as an additional ring feature.

Quasiparticle interference mapping

In order to interpret this standing wave pattern, the influence of a material's band structure on the resulting wave pattern will be discussed in the following. Equation (4.8) described the spatial variations in the DOS in the special case of intraband scattering of electrons with momentum $k_{||}$ in a single free-electron-like band in one dimension, leading to oscillations in the DOS with a wave number $q = 2k_{||}$.

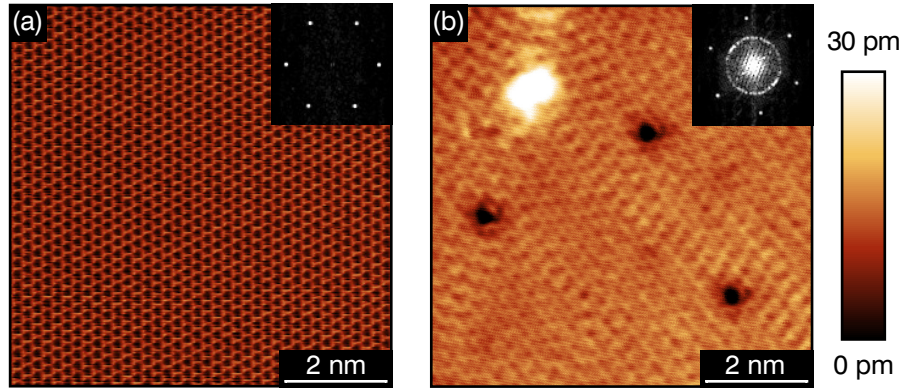


Figure 6.1: Atomic resolution STM images of the Be(0001) surface acquired in constant-current mode. a) An image taken in the absence of defects or impurities. The hexagonal atomic lattice is resolved. The inset depicts the fast-Fourier transform (FFT) of the image. Experimental parameters: $I = 1$ nA, $U = 50$ mV, $T = 4.2$ K, W tip. b) An image obtained in the presence of impurities acting as scatterers for surface electrons. A standing wave pattern superimposed on the atomic lattice is visible and appears as a ring in the FFT. Experimental parameters: $I = 8$ nA, $U = -10$ mV, $T = 4.2$ K, Cr tip.

For materials with more complex constant energy contours, elastic scattering will generally cause interference of states with different momenta \vec{k}_a and \vec{k}_b , leading to modulations in the density of states with wave vector $\vec{q} = \vec{k}_a - \vec{k}_b$ [124]. The situation is schematically depicted in Figure 6.2 for a surface with hexagonal symmetry and two states with concentric contours of constant energy. The scattering process can occur between states in a single band (intradband scattering) or between different bands (interband scattering) [125]. Corresponding wave numbers are exemplarily indicated along $\bar{\Gamma}-\bar{M}$ in the schematic. Consequently, the surface DOS can generally exhibit complex wave patterns resulting from a superposition of multiple scattering processes. The contributions of individual scattering vectors can be discriminated by FFT of STM or STS maps.

In constant-current mode STM, the resulting profile $z(x, y)$ at the bias voltage U is influenced by contributions of states in the interval $[E_F, E_F + eU]$. Consequently, constant-current images acquired at low bias voltages will reflect the Friedel oscillations at E_F [37, 126]. In the differential conductance dI/dU , the energy range of contributing states is limited to $[E_F + e(U - U_{\text{mod}}), E_F + e(U + U_{\text{mod}})]$. The electron dispersion can thus be reconstructed through Fourier analysis of dI/dU maps acquired at varying U . This technique called quasiparticle interference mapping was successfully employed to map the dispersion of the surface states on noble metals [36, 127].

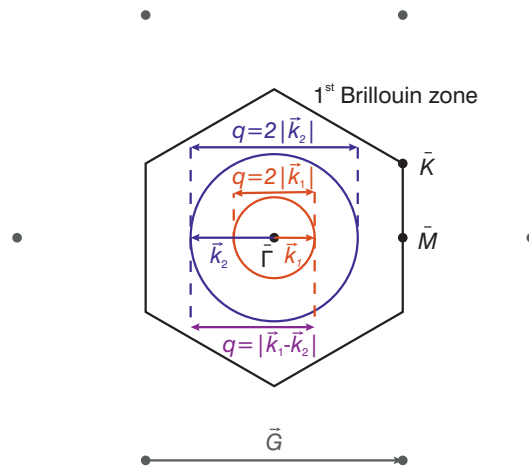


Figure 6.2: Schematic of scattering vectors in reciprocal space. The reciprocal hexagonal lattice is represented by gray dots and the reciprocal lattice vector \vec{G} . The Brillouin zone is depicted in black. The circles represent constant energy contours of two electronic states with momenta k_1 and k_2 . Different possible scattering vectors q are depicted along the $\bar{\Gamma}-\bar{M}$ direction for elastic intraband (blue, red) and interband scattering (violet).

Standing electron waves imaged in constant-current STM

With the small applied bias of $U = 10$ mV in Figure 6.1 (b), the STM is sensitive to electronic states close to E_F . The single dominant ring feature can be interpreted as the result of interference between states from a single band. Accordingly, the radius of the ring measures approximately $q = 2k_F$, with the Fermi wave vector k_F .

Figure 6.3 (a) again shows the FFT-STM picture of the standing waves and the atomic lattice. Here, the reciprocal lattice deviates from a perfect hexagon. It is distorted along the vertical axis, corresponding to the slow scan axis, by 4.9%. The reason is drift between tip and sample, caused for example by piezo creep of the tube scanner. The sharpness of the spots in the FFT signifies that the distortion is linear. This justifies a correction of the vertical axis in order to extract precise values for the q -vector of the standing waves.

The corrected data is depicted in Figure 6.3 (b). Here, the spots correspond to reciprocal lattice vectors \vec{G} of Be(0001). On careful inspection, deviations of the ring feature from a perfect circle are evident. This corresponds to an anisotropy of the standing electron waves. Line sections along $\bar{\Gamma}-\bar{M}$ and $\bar{\Gamma}-\bar{K}$ of the Fourier component's absolute values $|S|$ are shown in Figure 6.3 (c) and (d), respectively. The peaks in the Fourier spectra mark the wave vector of the standing waves seen in real space. Local fitting with Gauss profiles yields $q_F = (18.2 \pm 0.1) \text{ nm}^{-1}$ along $\bar{\Gamma}-\bar{M}$ and $q_F = (18.0 \pm 0.1) \text{ nm}^{-1}$ along $\bar{\Gamma}-\bar{K}$. The

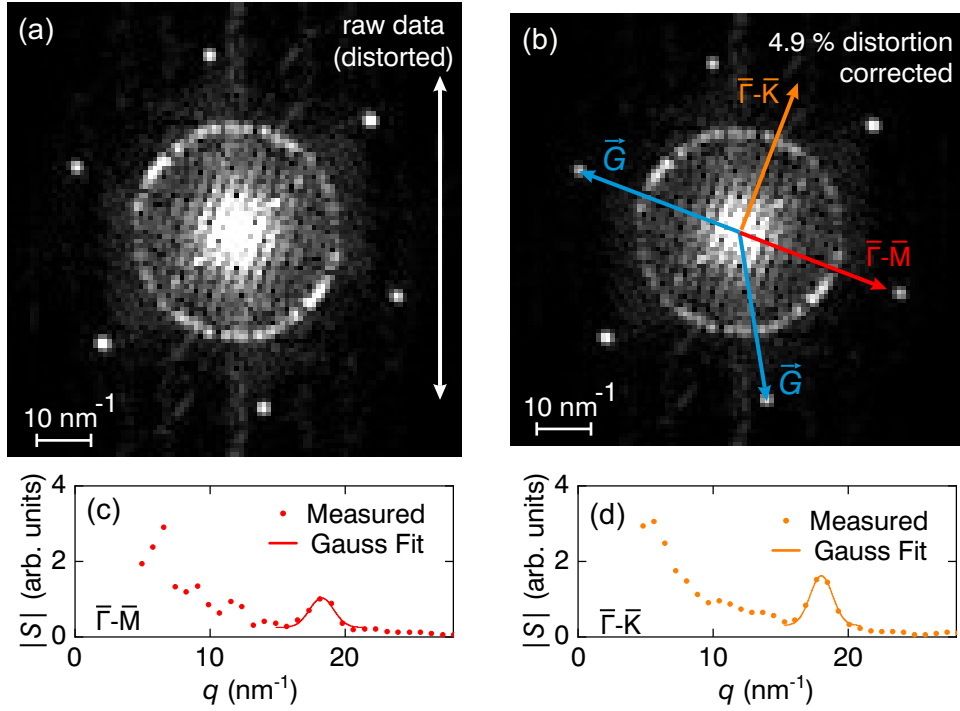


Figure 6.3: Analysis of the direction dependence of standing waves. (a) Enlarged depiction of the FFT in Figure 6.1 (b). The data is distorted along the vertical axis by 4.9%. (b) The data with corrected vertical dimensions. The reciprocal lattice vectors \vec{G} are indicated. (c), (d) Fourier spectra along $\bar{\Gamma}-\bar{M}$ and $\bar{\Gamma}-\bar{K}$, respectively, measured on the colored lines in (b). The standing waves' wave vector is deduced from a local Gaussian fit to the data.

falling background in $|S|$ was neglected in the fitting procedure. The deduced Fermi wave vectors of $k_{F,\bar{\Gamma}-\bar{M}} = 9.1 \text{ nm}^{-1}$ and $k_{F,\bar{\Gamma}-\bar{K}} = 9.0 \text{ nm}^{-1}$ agree well with the ARPES results of 9.2 nm^{-1} and 9.0 nm^{-1} , respectively, for the $\bar{\Gamma}$ -surface state [29].

The appearance of the sample surface depends on multiple parameters. Apart from impurities on the surface, also the chemical composition of the tip and its sharpness influence the tunneling process. For different terminations of the tip, contributions from different sample states to the tunneling process may vary, resulting in variations in the measured corrugation of standing electron waves and of the atomic lattice. A subtle change in the tip's electronic structure can change the measured corrugation or conductance modulation drastically, so that quantitative investigations of wave amplitudes are viable only with the same stable microtip.

The bias dependence of the standing wave corrugation can be seen in a series of STM images in Figure 6.4, obtained with a single tip in the vicinity of a

specific impurity [123]. The wave amplitude varies between 2 pm and 4 pm between $U = 87$ mV and $U = -1$ mV, with a general tendency towards higher corrugations for lower absolute bias. The enhancement of the wave amplitude is markedly smaller compared to the observation by Sprunger *et al.* [37], who observed an enhancement of the waves' amplitude by one order of magnitude at $|U| = 2.1$ mV compared to $|U| = 35$ mV. Beyond that, the z -corrugation is not suitable for a quantitative analysis of the bias-dependent wave amplitude or periodicity, as it includes contributions of sample states across a broad energy range.

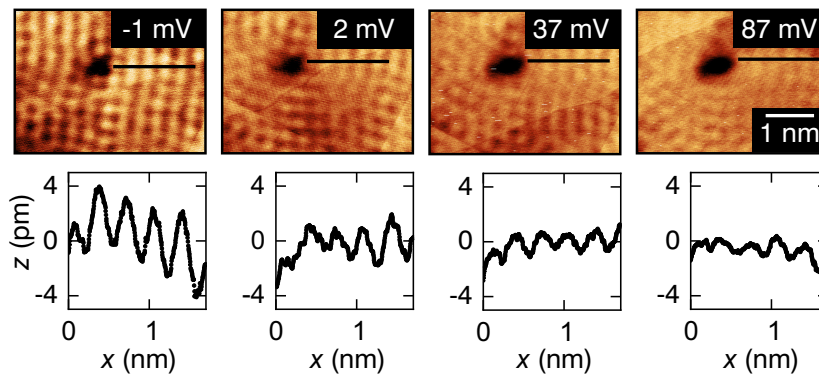


Figure 6.4: Constant-current STM images of standing electron waves in the vicinity of an impurity, imaged at varying bias voltage as indicated ($I = 1$ nA, $T = 40$ K, Cr tip). Line sections along the black lines in the images are displayed in the bottom row. They show a decreasing corrugation of the standing waves with increasing absolute bias [123]. Copyrighted by the American Physical Society.

6.2 Scanning tunneling spectroscopy results on Be(0001)

For an energy-resolved investigation of the electronic states of Be(0001), STS will be employed from here on to investigate the energy dispersion of the standing waves and their physical origin.

A typical tunneling spectrum of the Be(0001) surface, acquired inside the rectangle in Figure 6.5 (a) is depicted in Figure 6.5 (b) [123]. In the measurement, the tip was stabilized in z at $I = 7.75$ nA and $U = -4$ V. Then the z -feedback was disabled and dI/dU was measured in dependence of U at constant tip-sample distance. For comparison to the spectroscopy curve, the band structure of Be(0001) is depicted in Figure 6.5 (c).

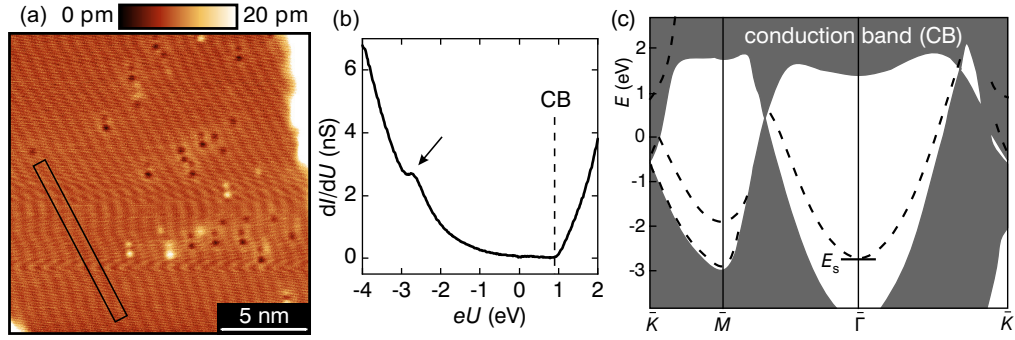


Figure 6.5: (a) Constant-current STM image of Be(0001). Parameters: $I = 1$ nA, $U = -400$ mV, $T = 4.2$ K, W tip (b) Broad range tunneling spectrum averaged over 25 query points inside the rectangle in (a). Stabilization conditions: $I = 7.75$ nA, $U = -4$ V, $U_{\text{mod}} = 10$ mV, $f = 4815$ Hz, W tip). A shoulder is visible inside the bulk band gap (arrow). A steep rise in dI/dU corresponds to the edge of the bulk conduction band. (c) Schematic of the band structure of Be(0001) for comparison. Shaded areas represent bulk states and broken lines are surface bands. (c) is adapted by permission from Springer [75] © 2000.

Several features in the spectrum can be related to the band structure. First, the steep conductance increase near $eU = 1$ eV signifies the onset of the bulk conduction band [77, 78]. Between E_F and $E = 1$ eV there is a region of relatively low conductance, corresponding to the partial bulk band gap of Beryllium [77]. Below E_F , there is a general trend of decreasing conductance with increasing U that can be explained by the likewise decreasing bulk DOS [78].

Another reason for the decreasing conductance can be found in the bias dependence of the decay constant [128]:

$$\kappa = \sqrt{\frac{2m_e}{\hbar^2} \left(\phi - \frac{|eU|}{2} + \frac{\hbar^2 k_{\parallel}^2}{2m^*} \right)}. \quad (6.1)$$

Due to the external bias voltage, the barrier height is effectively reduced by $|eU|/2$. In addition, the momentum parallel to the surface k_{\parallel} of electronic states in Be(0001) increases for eU approaching E_F [75]. The result is a further increase of the decay constant and a fast decay of electronic states into the vacuum for states close to E_F compared to states at much lower energy or inside the conduction band.

An additional striking feature in the tunneling spectrum is the shoulder on the falling background at negative energies, where the bottom of the $\bar{\Gamma}$ surface state band is found [75, 77]. In order to interpret this spectroscopic feature, the effect of scattering processes leading to a finite lifetime of surface states, and the implications for tunneling spectroscopy will be discussed.

Lifetime corrections to the free electron model

The DOS of parabolic surface state bands in two dimensions as found on Be(0001) were discussed idealistically in section 4.1.1. In experiments on real crystal surfaces, many-body interactions like electron-electron and electron-phonon scattering will influence the measurements and lead to variations from the free electron model. Namely, surface state electrons will scatter through electron-electron or electron-phonon interactions into different surface states or into bulk states. The influence of these interactions on the single particle state are described by the self-energy $\Sigma = \text{Re } \Sigma + i \text{Im } \Sigma$. The real part $\text{Re } \Sigma$ renormalizes the dispersion relation:

$$E_{\text{renorm}}(\vec{k}) = E(\vec{k}) + \text{Re } \Sigma(\vec{k}, E, T), \quad (6.2)$$

thus affecting the DOS [90]. Additionally, the many body interactions lead to a finite lifetime τ of the single particle states, which is quantified by $\text{Im } \Sigma$. Instead of τ , the inverse lifetime Γ is more customarily used as it represents the linewidth of states in spectroscopic measurements [90, 129]:

$$\Gamma = \frac{\hbar}{\tau} = 2|\text{Im } \Sigma|. \quad (6.3)$$

The self-energy, and consequently Γ , is generally energy- and temperature dependent. For the electron-electron contribution, the temperature dependence is explicit [130, 131]:

$$\Gamma_{\text{ee}}(E) = 2\beta \left[(\pi k_{\text{B}} T)^2 + (E - E_{\text{F}})^2 \right], \quad (6.4)$$

where β is a material-dependent prefactor. The electron-phonon contribution

$$\Gamma_{\text{ep}}(E) = 2\pi\hbar \int_0^{E_{\text{max}}} \alpha^2 F(E') \left[1 - f(E - E') + f(E + E') + 2n(E') \right] dE', \quad (6.5)$$

depends on the Eliashberg function $\alpha^2 F$, consisting of the phonon DOS F weighed with the interaction strength α [131, 132]. E_{max} denotes the energy of the highest occupied phonon mode. The temperature dependence enters via the Fermi-Dirac distribution function $f(E)$ and the Bose-Einstein distribution $n(E)$. Another important measure in this respect is the electron-phonon coupling parameter

$$\lambda = 2 \int_0^{E_{\text{max}}} \frac{\alpha^2 F(E)}{E} dE \quad (6.6)$$

describing the enhancement of the effective mass near the Fermi level by the factor $(1 + \lambda)$ [133].

The finite lifetime leads to a broadening of the DOS at the minimum of a parabolic surface band compared to the step function in Equation (4.5), where many-body interactions were neglected [129]:

$$\rho_{2D}(E) \propto \arctan\left(\frac{E - E_s}{\Gamma_s/2}\right). \quad (6.7)$$

Here, Γ_s is the inverse lifetime of the surface state at the band minimum E_s . Surface electron bands similar to those on Be(0001) exist on the (111) surfaces of the noble metals Cu, Ag and Au [129, 134]. These surfaces were studied intensively with STS in the past, exploiting the proportionality of the differential conductance dI/dU to the sample DOS (see section 2.2). In the following, experimental techniques to deduce the surface state lifetime and dispersion from STS data will be introduced.

Threshold spectroscopy around the band minimum

With the bias voltage U applied to the sample in an STM junction, only sample states in the energy window $[E_F, E_F + eU]$ will contribute to the tunneling process. In point mode STS, U is varied at constant tip-sample distance. When eU exceeds the onset energy of a surface band E_s , additional states abruptly become available for the tunneling process, leading to a stepwise increase in the measured differential conductance dI/dU analogously to Equation (6.7). At low temperatures, with the Fermi-Dirac distribution converging towards a step function, the thermal broadening of the tunneling spectrum can be neglected and the differential conductance can be modeled as

$$\frac{dI}{dU}(U) \propto \rho_{\text{bulk}} + c \arctan\left(\frac{eU - E_s}{\Gamma_s/2}\right), \quad (6.8)$$

with a constant scaling factor c , representing a broadened step on a background provided by bulk sample states [135]. This simple model neglects influences of the tip wave function. Additionally, for $eU > E_s$ the momentum parallel to the surface k_{\parallel} of the surface state will increase. This diminishes the surface state contribution to dI/dU because of the increasing decay into the vacuum region for high k_{\parallel} [136]. These distortions of the spectra complicate the interpretation in terms of linewidths.

Nevertheless, this technique was successfully applied to deduce E_s and Γ of surface states on noble metals from STS data [135, 137, 138]. The advantage

of this technique compared to photoemission is the lateral resolution of STS allowing for a reduced influence of impurity scattering on the linewidth. The linewidths found in STS [137] are in good agreement with theoretical Green's function calculations [137] and photoemission data [139], which shows the reliability of this approach.

Quantitative analysis of tunneling spectroscopy on Be(0001)

The broad range tunneling spectrum of Be(0001) is depicted again in Figure 6.6 (a) with electron energy along the vertical axis. Comparison to the band structure of Be(0001) showed that the falling background for $eU \lesssim 1$ eV can be interpreted as contributions of bulk states to the tunneling conductance. This background contribution to the spectrum was fitted with a 4-th order polynomial.

The difference between the experimental data and the fit to the background is shown in Figure 6.6 (b). The curve exhibits a sharp, step-wise increase of dI/dU followed by a slower decaying signal at higher energies. This spectral shape was observed on noble metal surfaces as well and interpreted as a signature of an incipient surface state band [135, 136]. In the case of Be(0001), the observed feature occurs in the energy range where ARPES experiments found

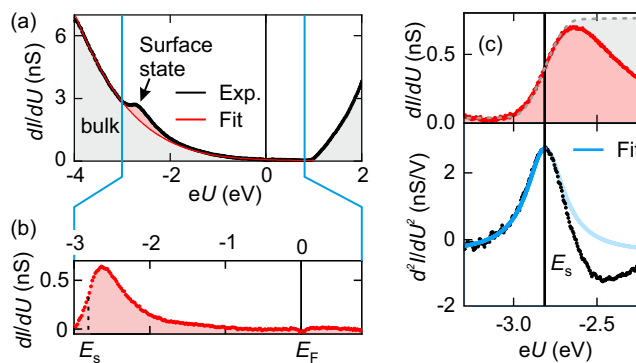


Figure 6.6: (a) Broad range tunneling spectrum of Be(0001) ($T = 4.2$ K, stabilization conditions: $I = 7.75$ nA, $U = -4$ V, $U_{\text{mod}} = 10$ mV, $f = 4815$ Hz, W tip). A shoulder is visible near the onset energy of the Γ -surface state. A 4-th order polynomial fit to the monotonously falling background is shown in red. (b) Difference of the experimental data and the background fit in (a), representing the surface state contribution to the tunneling spectrum. (c) Top panel: Tunneling spectrum around the surface state onset taken with higher resolution (stabilization conditions: $I = 1$ nA, $U = -2.2$ V, $U_{\text{mod}} = 5$ mV). The broken gray line represents a symmetric conductance step. Bottom panel: Numerical derivative d^2I/dU^2 of the data above. The onset energy E_s is determined as the peak position. A Lorentzian fit is shown in blue. The figure is reproduced from [123]. Copyrighted by the American Physical Society.

the onset of the $\bar{\Gamma}$ surface state. Consequently, Figure 6.6 (b) is interpreted as an approximation of the surface state contribution to the tunneling conductance.

A higher resolution spectrum in the respective energy range is given in Figure 6.6 (c), again after subtraction of the polynomial background. According to the model Equation (6.8), the point of inflection marks the surface state band minimum E_s . Within this model, the conductance should be symmetric (indicated by a gray dotted line) with respect to the point of inflection. This deviation from a symmetric step could be explained by the increasing momentum $k_{||}$ carried by surface state electrons with increasing energy $E - E_s$. The increasing values of $k_{||}$ will lead to a suppression of the tunneling probability for states with increasing energy due to their faster decay into the vacuum [45, 128].

The quantitative analysis of the spectrum is complicated by the deviations from the model as a direct fit of Equation (6.8) is not possible. However, the point of inflection E_s can be extracted as the peak position of the differentiated spectrum. The numerical derivative d^2I/dU^2 is given in the bottom panel of Figure 6.6 (c). The onset energy E_s was estimated to $E_s = (-2.81 \pm 0.01)$ eV by fitting the peak position locally with a parabola. For the surface state model, differentiation of Equation (6.8) leads to a Lorentzian profile:

$$\frac{d^2I}{dU^2}(U) \propto \frac{\Gamma_s}{4(eU - E_s)^2 + \Gamma_s^2}. \quad (6.9)$$

A fit of this profile to the d^2I/dU^2 data restricted to $E < E_s$, where the measurement is unaffected by the influence of finite $k_{||}$, is shown in blue. The fit yields a surface state linewidth of $\Gamma_s = (272 \pm 4)$ meV. This value is of the same magnitude as the ARPES value of $\Gamma_s \approx 350$ meV extrapolated to low temperatures [140]. A tentative explanation for the higher value found in laterally averaging ARPES experiments could be a stronger influence of impurity scattering compared to STS measurements. Our STM measurements revealed residual impurities on Be(0001) surfaces that coexist besides extended clean terraces even after extensive sputter treatment. ARPES measurements will average over extended surface areas including the surrounding of such impurities, whereas STS probes surface areas of a low local impurity density. In conclusion, the tunneling spectrum in its entirety can be explained by the bulk electronic structure of Be complemented by the surface DOS of Be(0001).

6.3 Mapping the surface electron dispersion

The standing electron waves on Be(0001) observed in STM for tunneling bias close to the Fermi level were discussed in section 6.1. In this section, the

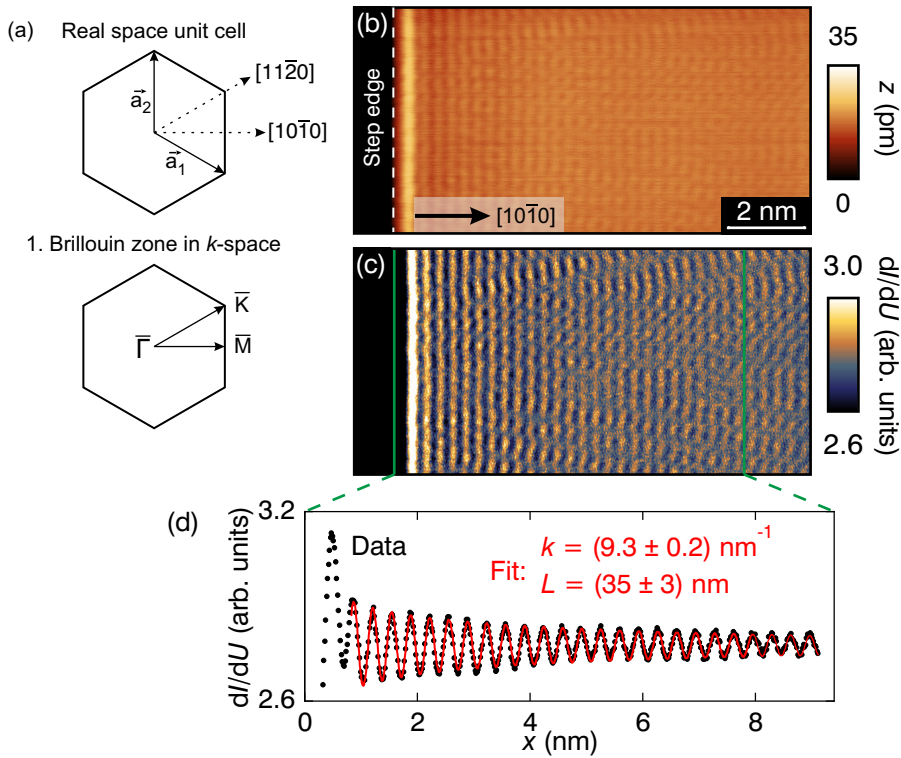


Figure 6.7: Decay of standing waves on Be(0001). (a) Sketch of the surface unit cell in real space and in k -space. (b) Constant-current STM image of standing waves on Be(0001) emanating from a straight step edge. (c) Simultaneously acquired differential conductance. A Gaussian filter with a FWHM of 2 px was used for better visibility of the standing wave pattern in dI/dU . (d) Graph of the unfiltered $dI/dU(x)$ averaged over horizontal lines in (c) together with a model fit of energy-resolved Friedel oscillations. Experimental parameters: $I = 1 \text{ nA}$, $U = -20 \text{ mV}$, $T = 4.2 \text{ K}$, $U_{\text{mod}} = 20 \text{ mV}$, $f = 4444 \text{ Hz}$, Cr tip.

standing waves will be explored using STS with respect to their spatial decay and their dispersion in energy.

Figure 6.7 (b) depicts an STM image of a Be(0001) terrace and a straight step edge imaged with $U = -20 \text{ mV}$. Directly at the step edge, an increased apparent height is measured. This may originate from an increased DOS at the step edge due to the lowered coordination number of Be atoms there. A standing wave pattern on the terrace is evident. The real space unit cell of Be(0001) and the first Brillouin zone are shown in Figure 6.7 (a). As the step edges in the Be sample run preferentially along the high-symmetry directions $\langle 11\bar{2}0 \rangle$, they act as well defined one-dimensional scatterers for electrons. Consequently, standing electron waves originating from scattering at step edges propagate along the directions $\langle 10\bar{1}0 \rangle$.

The simultaneously acquired differential conductance map is shown in Figure 6.7 (c). The standing wave pattern is reflected there in oscillations of dI/dU . Figure 6.7 (d) shows the spatial evolution of the oscillations averaged over horizontal lines. Similar to z , there is an increased dI/dU at the step edge.

As the differential conductance is a measure of the electronic sample DOS, the oscillations in dI/dU can be compared to the model of a free-electron-like surface state. The DOS at the surface band onset was found to be smeared out compared to a two-dimensional free electron gas due to finite lifetime effects. For the Friedel oscillations on surfaces, the finite lifetime leads to a finite coherence length $L(E) = \tau(E)k(E)\frac{\hbar}{m^*}$ and consequently to an exponential spatial decay of the Friedel oscillations' amplitude [141]. Consequently, Equation (4.8) has to be modified to yield a suitable approximation for the DOS at a real crystal step [141]:

$$\rho(E, x) = \rho_{\text{bulk}} + \rho_{2\text{D}} \left(1 - r(E) \exp\left(-\frac{2x}{L}\right) J_0\left(2k_{\parallel}x\right) \right). \quad (6.10)$$

Here, a finite reflectivity $r(E)$ of the step and a background term of bulk states were incorporated.

A fit of this model to the experimental $dI/dU(x)$ is shown in red in Figure 6.7 (d). The enhanced dI/dU directly at the step edge was excluded from the fitting procedure. The experimental data is well reproduced in the fit. Values of $k = (9.3 \pm 0.1)\text{nm}^{-1}$ and $L = (35 \pm 3)\text{nm}$ were extracted. The standing waves correspond to an interference pattern of quasiparticles propagating along $\bar{\Gamma}-\bar{M}$ in k -space, as can be seen from the sketch in Figure 6.7 (a). The deduced k -value is again in good agreement with the ARPES value of $k_{\text{F},\bar{\Gamma}-\bar{M}} = 9.2\text{nm}^{-1}$ [29]. This shows that the standing wave pattern reflected in dI/dU behaves like Friedel oscillations in a two-dimensional electron gas for low bias voltages, corresponding to electron energies close to E_{F} .

In the following, the evolution of the standing waves' period with varying bias voltage are presented. Figure 6.8 (a) exhibits three dI/dU maps of a surface area in the vicinity of an atomic step edge, acquired at $U = -1800\text{mV}$, $U = -800\text{mV}$, and $U = 200\text{mV}$, respectively. Standing electron waves are visible in all three images with a clearly varying wavelength. This is indicative of a dispersive behavior of the standing waves on Be(0001).

In order to map the dispersion of the surface state in more detail, a series of tunneling spectra was acquired at varying distance from a scatterer. The situation is depicted in Figure 6.8 (b). A straight step edge is exploited to study the dispersion of the wave pattern perpendicular to it. At successive setpoints x of the distance from the step edge, the feedback loop was opened at defined

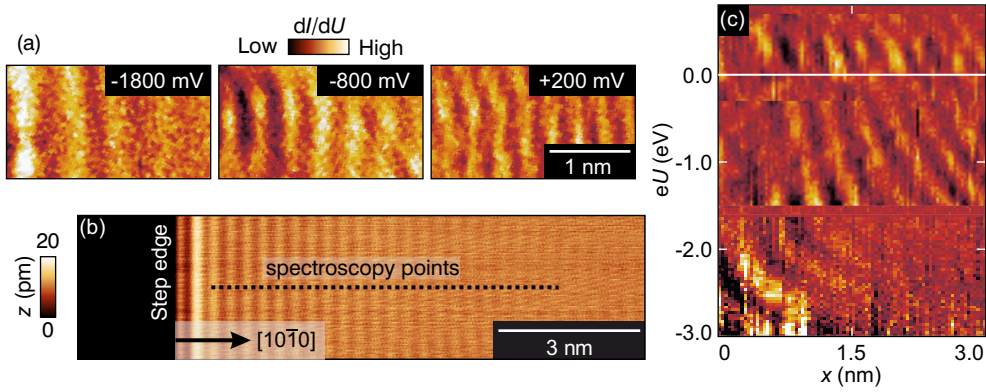


Figure 6.8: (a) Bias-dependent dI/dU maps of standing wave patterns, acquired at values of U as indicated. The periodic length clearly changes with U . ($T = 4.2$ K, $U_{\text{mod}} = 10$ mV, $f = 4815$ Hz, $I = 8$ nA, 5 nA, 3 nA). (b) Constant-current STM image of standing waves emanating from a step edge that runs along a high-symmetry direction of Be(0001) ($T = 4.2$ K, $I = 1$ nA, $U = -100$ mV). The propagation direction of standing electron waves is along $[10\bar{1}0]$. (c) Color plot of dI/dU from tunneling spectra taken as a function of distance x from an atomic step edge as schematically indicated in (b). Bias ranges: $[-3.0; -1.6]$ V; $[-1.5; -0.3]$ V; $[-0.3; 0.7]$ V. Stabilization conditions: $(-3.0$ V, 2 nA); $(-1.5$ V, 2 nA); $(-0.3$ V, 1 nA). Each horizontal row is normalized to its mean value. Adapted from [123]. Copyrighted by the American Physical Society.

stabilization conditions and the bias U was ramped between -3 V and 0.7 V. Figure 6.8 (c) depicts the color coded dI/dU -values as a function of U and x along $[10\bar{1}0]$. Because of the huge variations of the tunnel current associated with sweeping the bias voltage over a range of more than 3 V, the experiment was split into three smaller bias ranges. This guarantees a sufficient signal-to-noise ratio for the lock-in detection and prevents a saturation of the current amplifier. A continuous change in the periodicity of the spatial variation of dI/dU in dependence of the bias voltage U is evident.

In order to extract the energy dependence of the electron wave number k , Figure 6.8 (c) was analyzed using the 1D-FFT along x . The result is shown in Figure 6.9 (a). Absolute values of the Fourier components $|S(k)|$ for every bias voltage \bar{U} are plotted against the wave number k in the first Brillouin zone along $\bar{\Gamma}-\bar{M}$. Note that this wave number corresponds to half the wave number q of the observed standing waves (see Equation (6.10)). Evidently, the major Fourier components follow a parabola in agreement with the model of energy resolved Friedel oscillations of a free-electron-like surface state.

Using the dispersion relation

$$E(k) = E_s + \frac{\hbar^2 k_{\parallel}^2}{2m^*}, \quad (6.11)$$

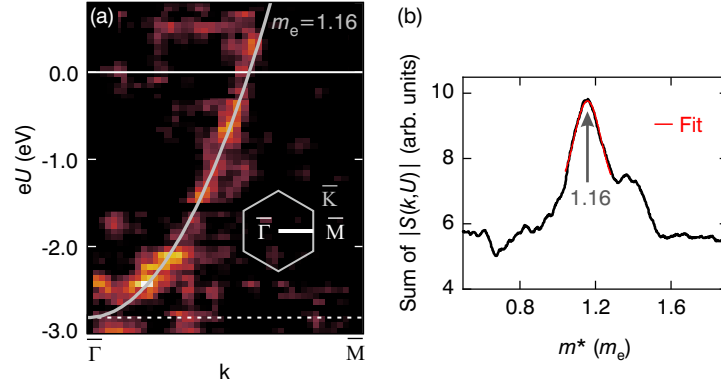


Figure 6.9: (a) Color map of normalized Fourier components along the $\bar{\Gamma}-\bar{M}$ direction calculated from the data in Figure 6.8 (c) using one-dimensional FFT along x . (b) Cumulative sum of Fourier components in (a) along parabolic dispersion curves with $E_s = -2.81$ eV in dependence of m^* . A Gaussian fit to the peak is given in red. (a) is adapted from [123]. Copyrighted by the American Physical Society.

the effective mass m^* of the surface state electrons can be extracted from the data. For this purpose, the sum of Fourier components $|S(k, U)|$ along supposed parabolic dispersion curves with varying m^* and $E_s = -2.81$ eV fixed to the value found in section 6.2 is displayed in Figure 6.9 (b). The maximum cumulative weight in the FFT, corresponding to the best accordance with the model, can be found by local fitting of the peak in Figure 6.9 (b) with a Gaussian profile. The fit yields $m^* = (1.16 \pm 0.01) m_e$. This value is in good agreement with values between $1.19 m_e$ [86] and $1.27 m_e$ [142] found along $\bar{\Gamma}-\bar{M}$ in photoemission studies. Consequently, the observed standing waves show a dispersion characteristic for Friedel oscillations of the $\bar{\Gamma}$ -surface state on Be(0001).

The analysis was limited to the $[10\bar{1}0]$ direction (corresponding to $\bar{\Gamma}-\bar{M}$ in reciprocal space) because the dominant directions of step edges favors the propagation of coherent standing waves along this direction. The resolution in k -space depends on the extent of the probed standing waves in real space. Standing waves along $[11\bar{2}0]$ of a similar extent to those in Figure 6.8 (a) are scarce to nonexistent, so that an analogue analysis for the $\bar{\Gamma}-\bar{K}$ direction was omitted.

Comparison of the results to previous STM studies

The standing wave pattern on Be(0001) exhibits a parabolic energy dispersion that corresponds to the dispersion relation of the free-electron-like $\bar{\Gamma}$ -surface

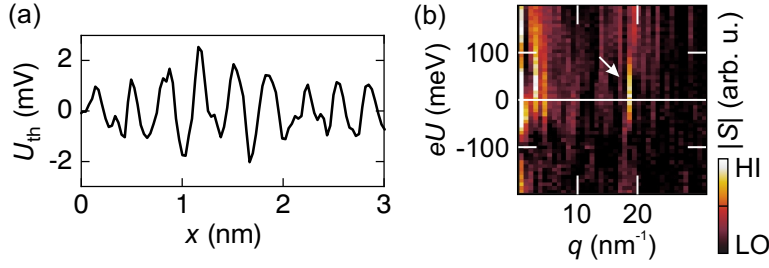


Figure 6.10: (a) Profile of U_{th} in dependence of step edge distance and energy derived from Figure 6.8 (c) for the case of $T_{\text{T}} = 300$ K and $T_{\text{S}} = 150$ K. Significant variations of U_{th} are evident across the standing wave pattern. (b) Cutout from Figure 6.9 (a) around E_{F} . The standing waves show an enhanced spectral weight in the vicinity of E_{F} . (b) is adapted from [123]. Copyrighted by the American Physical Society.

state. No drastic bias dependence of wave amplitudes was found for values of U within a few mV of E_{F} , in contrast to a previous STM study by Sprunger *et al.* [37], in which this enhanced amplitude was interpreted as a possible manifestation of a CDW. The dispersive behavior of the standing waves observed in this work is in contradiction to a CDW [143]. A difference between this study and the previous experimental approach is that in this study tip and sample are thermally coupled to a cryostat, while only the sample was effectively cooled to 150 K in the previous one [144].

Remembering Equation (2.11), a temperature difference between tip and sample creates a thermovoltage of

$$U_{\text{th}} = \frac{\pi^2 k_{\text{B}}}{6e} (T_{\text{T}}^2 - T_{\text{S}}^2) \left. \frac{\sigma'}{\sigma} \right|_{U=0} \quad (6.12)$$

across the tunnel junction. Here, $\sigma = dI/dU$ is the conductance and $\sigma' = d\sigma/dU$. Consequently, the thermovoltage can be deduced from a tunneling spectrum and its numerical derivative.

Spatially resolved values for $\sigma(U = 0)$ and $\sigma'(U = 0)$ were deduced from the STS data in Figure 6.8 (c). Figure 6.10 (a) shows the resulting values of U_{th} for the situation of a sample at $T = 150$ K and a tip at $T = 300$ K. One can see that the standing wave pattern is reflected in the data with significant spatial variations of U_{th} . The variations amount to $|U_{\text{th}}| \lesssim 2$ mV. For the situation in [37] with $U \approx -2$ mV this means that the effective bias $U_{\text{eff}} = U + U_{\text{th}}$ will vary laterally between 0 mV and -4 mV. In constant-current mode, this will have a significant influence on the measured corrugation of the standing waves, as explicitly demonstrated by Homoth *et al.* in the case of Ag(111) [145]. For larger bias values, the magnitude of the thermovoltage becomes comparably

smaller and its influence on the integrated tunneling current becomes gradually less severe. Accordingly, the influence of the spatially varying thermovoltage on the tip-sample separation in constant-current mode is diminished for larger absolute bias values. Consequently, the enhanced standing wave amplitudes observed by Sprunger *et al.* for small bias values can be explained by a difference in the experimental setup.

However, an enhanced magnitude of the standing waves on the energy scale of $eU \lesssim \pm 80$ meV was observed in this work, as shown in Figure 6.10 (b). The data exhibits a relative enhancement of the spectral density of the standing waves' q -vector in this energy window. A similar observation was made concerning the surface state on Ag(111) [146]. There, the enhancement is attributed to inelastic tunneling effects.

6.4 Inelastic tunneling effects on Be(0001)

So far, the electronic structure of the Be(0001) surface and its manifestation in STS were discussed in this chapter. Now the discussion will be extended to inelastic tunneling processes.

6.4.1 Results of inelastic tunneling spectroscopy

The tunneling spectrum over a broad bias range (Figure 6.6), showed a relatively low tunneling conductance within $|eU| < 1$ eV. This was explained by the partial bandgap of Be(0001) in this range hosting only electronic states of large parallel momenta k_{\parallel} . Carefully inspecting Figure 6.6 (b), one notices a further reduced conductance at E_F . On the same surface region, a tunneling spectroscopy study with higher resolution in this energy range was conducted. The data, averaged over 25 spectroscopy points on the clean Be(0001) surface is shown in Figure 6.11 (a). The spectrum exhibits a reduced dI/dU within ± 80 meV on a decreasing background.

Upon closer examination, two symmetric steps on both, the positive and the negative bias side become evident. Figure 6.11 (b) exhibits d^2I/dU^2 derived from numerical differentiation of the spectrum. Incidental with the symmetric steps in dI/dU , asymmetric peaks at ± 41 meV and at ± 67 meV can be identified in d^2I/dU^2 . Such an enhancement of the tunneling conductance symmetric around $U = 0$ V is indicative for inelastic tunneling processes, as described in section 2.4 and sketched in the insets. A schematic picture of inelastic tunneling processes in STM in the case of tunneling from the surface state band of the sample into unoccupied tip states is shown in Figure 6.11 (c). Below a threshold

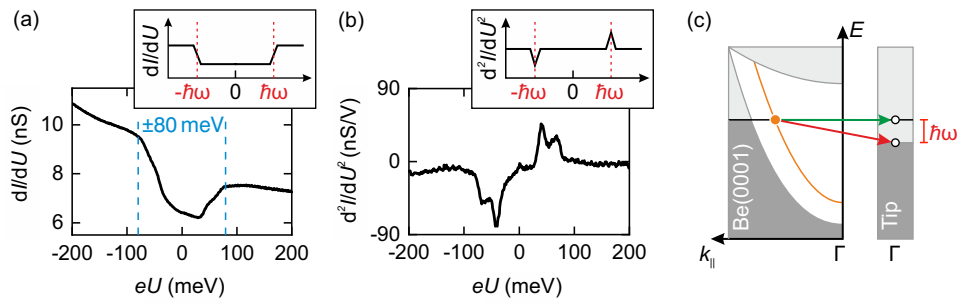


Figure 6.11: (a) High resolution scanning tunneling spectrum of Be(0001) ($T = 4.2$ K, stabilization conditions: $I = 1.83$ nA, $U = -200$ mV, $U_{\text{mod}} = 2$ mV, $f = 4815$ Hz, W tip). (b) Numerical differentiation of the spectrum in (a). The insets exemplify signatures of inelastic excitations of energy $\hbar\omega$ in dI/dU and d^2I/dU^2 , respectively. (c) Schematic of surface state electrons in Be(0001) tunneling into tip states via elastic (green) and inelastic (red) processes. Light (dark) shaded areas represent filled (empty) bulk states. Adapted from [123]. Copyrighted by the American Physical Society.

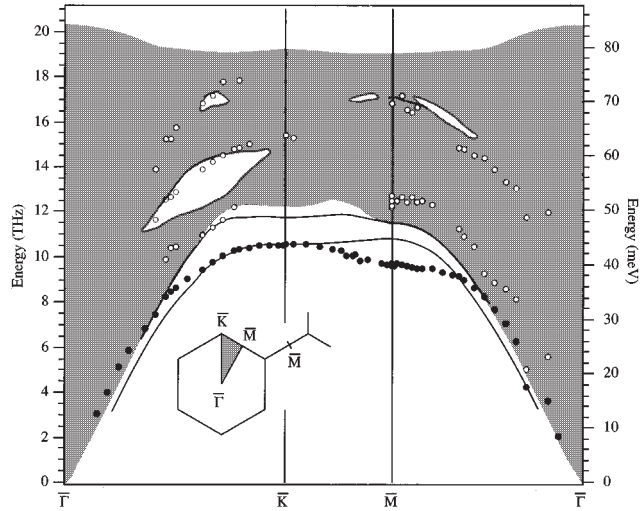
energy ($|eU| < \hbar\omega$) only elastic tunneling of electrons is possible (green). Here, $\hbar\omega$ is the lowest energy of possible inelastic excitations that could be for example vibrational modes in molecules or phonon modes in solids. If the energy of the tunneling electron at least equals $\hbar\omega$, it can tunnel into unoccupied states in the opposite electrode under excitation of such a mode and loss of the respective energy. This inelastic tunneling process is depicted in red. Consequently, the inelastic process adds to the elastic tunneling probability and leads to a stepwise increase in the tunneling conductance at $eU = \hbar\omega$.

6.4.2 Influence of electron-phonon coupling on the tunneling process

In order to elucidate the origin of the inelastic tunneling processes, the phononic properties of Be(0001) are presented in the following as they pose a possible cause for the observed phenomena. The phonon spectrum of Be(0001) is depicted in Figure 6.12 [74]. Phononic states exist for energies up to ~ 80 meV. The bulk phonon DOS is high for phonon energies $E_{\text{ph}} > 50$ meV [78, 147]. Below this energy, a mode appearing with high intensity in electron energy loss spectroscopy exists, marked by filled circles in Figure 6.12. This so-called Rayleigh mode is highly surface-localized for k -values away from the $\bar{\Gamma}$ -point and is associated with atom displacements perpendicular to the surface [74, 147]. Another surface mode, the shear horizontal mode, is found at higher energies, crossing the \bar{M} point at ca. 50 meV [74, 76, 147].

The electronic properties of Be(0001) are influenced by coupling to these

Figure 6.12: Phonon dispersion of Be(0001). Filled and open circles represent intense and weak features found in electron energy loss spectroscopy measurements, respectively. Solid lines represent calculated surface phonon modes. Reprinted with permission from [74]. Copyright (1996) by the American Physical Society.



phonon modes. On the one hand, the electron-phonon coupling influences the electron self-energy. Its imaginary part, and with it the linewidth Γ of electronic states, rises continuously for electron energies up to the maximum phonon energy of $E_{\max} \approx 80$ meV, according to Equation (6.5). Above E_{\max} , the phonon contribution to Γ is nearly constant [76]. Consequently, the lifetime of surface states outside of ± 80 meV around E_F is reduced, leading to a faster decay of energy-resolved Friedel oscillations at these energies. This can explain the enhanced spectral weight observed in Figure 6.10 (b) [146]. Additionally, the real part of the self-energy flattens the surface state dispersion within this energy range, locally reducing the effective mass and enhancing the DOS. Due to the limited resolution in momentum space associated with the decay of the standing waves, the subtle change in m^* is not resolved in Figure 6.10 (b).

Interpretation of the inelastic tunneling spectroscopy

The role of electron-phonon coupling in IETS can be understood through the schematic in Figure 6.13 (a). As discussed previously, for energies close to E_F , the electron momentum parallel to the sample surface is large and hence the absolute elastic tunneling probability is low. In an inelastic tunneling process, a phonon with momentum k_{ph} equal to the difference of momenta of initial and final electronic states $k_i - k_f$ is generated. Thus, the number of possible transition processes, including final states closer to the $\bar{\Gamma}$ point, increases, leading to a higher tunneling probability and a higher conductance. Within this picture, the inelastic effects seen in the IETS can be related to the phonon spectrum.

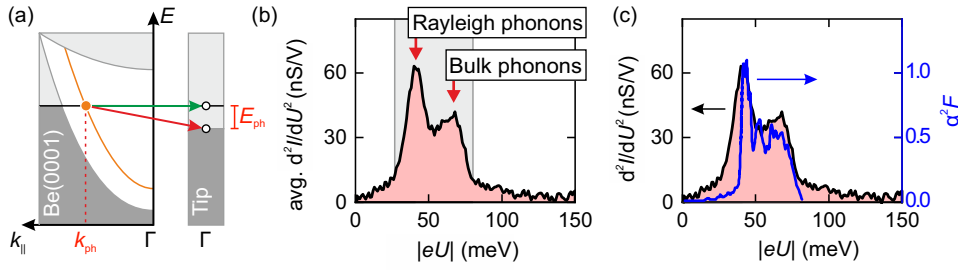


Figure 6.13: (a) Schematic of surface state electrons in Be(0001) tunneling into tip states via elastic (green) and phonon-mediated inelastic (red) processes. Light (dark) shaded areas represent filled (empty) bulk states. (b) Absolute values of d^2I/dU^2 from Figure 6.11, averaged over positive and negative bias values. The peaks at 41 meV and 67 meV are marked by arrows and assigned to Rayleigh phonons and bulk phonons, respectively. The range of sizable inelastic contributions to the spectrum is shadowed in gray. (c) Comparison of d^2I/dU^2 measured in IETS (black) with the Eliashberg function α^2F (blue) derived by DFT from [79]. Images adapted from [123]. Copyrighted by the American Physical Society.

Figure 6.13 (b) shows the absolute d^2I/dU^2 values from Figure 6.11 (b) averaged over the positive and negative bias values. The bias range of sizable d^2I/dU^2 values and hence of considerable inelastic contributions to the tunneling process is shadowed in gray. Comparison to the phonon spectrum in Figure 6.12 exposes that there is a high phonon DOS in the corresponding energy range. Peaks in d^2I/dU^2 appear at 41 meV and 67 meV. On Be(0001), the Rayleigh phonon mode disperses up to approximately 40 meV for large momenta parallel to the surface [78, 79]. Consequently, the first peak in Figure 6.13 (b) is assigned to inelastic tunneling via coupling to Rayleigh phonons. The peak at higher energy will be attributed to the opening of an additional inelastic conduction channel via different phonon modes.

The magnitude of the inelastic tunneling contribution depends on the involved initial and final electronic states, as well as on the DOS of participating phonons of the sample and their coupling strength to electrons. Influences of phonons in the W tip on the d^2I/dU^2 spectrum can be neglected due to the small electron-phonon coupling of W [56]. The electron-phonon coupling in the sample as a function of energy is described by the Eliashberg function α^2F of Be(0001), reflecting the continuous phonon spectrum. From Equation (2.17) we see that d^2I/dU^2 can be qualitatively compared to α^2F [55, 56]:

$$\frac{d^2I}{dU^2}(U) \propto \alpha^2F(eU). \quad (6.13)$$

A comparison of the experimental IETS data and α^2F as derived from DFT for electron-phonon coupling of the $\bar{\Gamma}$ -surface state at E_F [79] is depicted in

Figure 6.13 (c). Both quantities exhibit similar shapes with respect to energy: a low intensity at $eU = 0$ meV followed by a steep rise and a low intensity again for $eU > 80$ meV. Also the relative intensities are well reproduced. A deviation exists at low energies, where the IETS data exhibits a higher intensity compared to the theory.

The IETS peak at 41 meV coincides with a peak in α^2F that was also attributed to strong coupling of the Rayleigh phonon mode to the surface state in DFT [79]. A peak at the same energy was also observed experimentally in ARPES for states with momentum along $\bar{\Gamma}-\bar{M}$ [90]. For the peak at 67 meV there was a pendant previously observed in ARPES experiments [76] and attributed to coupling via bulk phonon modes [148]. Consequently, there is a good qualitative agreement between d^2I/dU^2 measured in IETS and previous experimental, as well as theoretical studies of the electron-phonon coupling in Be(0001).

When comparing IETS and ARPES measurements, the experimental differences of these approaches have to be kept in mind. In ARPES, the renormalized electron dispersion is measured along a set of directions in reciprocal space. From the deviations compared to the bare particle dispersion, the real part of the electron self-energy $\text{Re } \Sigma(E, \vec{k})$ can be deduced (see Equation (6.2)). α^2F is then reverse engineered by inversion of the integral [149]

$$\text{Re } \Sigma(E, \vec{k}, T) = \int_0^\infty \alpha^2F(\omega, E_F, \vec{k}) K(E, \omega) d\omega, \quad (6.14)$$

$$K(y, y') = \int_{-\infty}^\infty \frac{2y'}{x^2 - y'^2} f(x - y) dx, \quad (6.15)$$

with the temperature dependence implicit in the Fermi distribution function $f(x)$. This measurement depends on the many-body interactions of the probed band, such as electron-phonon and electron-electron interactions, governing the self-energy. The initial and final states involved in the electron-phonon scattering processes are exclusively states in the sample. For Be(0001), α^2F derived in this way from the renormalized surface state dispersion will represent the phonon-mediated scattering of surface state electrons with energy close to E_F into all available electronic final states. Eiguren *et al.* calculated that intraband scattering of the $\bar{\Gamma}$ -surface state together with scattering into the surface state around \bar{M} contribute 90 % to the Eliashberg function.

In IETS the situation is different. The inelastic tunneling process comprises an initial state in one electrode and a final state in the other. Furthermore, the STM geometry favors states with $k_{\parallel} = 0$. Consequently, for metal surfaces without a projected gap in the center of the Brillouin zone, d^2I/dU^2 is in

good approximation proportional to the momentum resolved Eliashberg function $\alpha^2F(\omega, E_F, k_{\parallel} = 0)$ [150]. Be(0001), however, has a partial bandgap at E_F , meaning that the (elastic) transmission probability is diminished according to Equation (2.6). Inelastic processes open additional tunneling channels for electrons that enhance the total tunneling probability, given a sufficient excess energy to excite a phonon mode in the sample. With the excited phonon ensuring conservation of momentum, tip states with low k_{\parallel} that decay slower into the vacuum region can contribute to the inelastic tunneling processes [151, 152]. This could lead to a further enhanced tunneling probability at energies eU corresponding to energies of phonon modes with momenta matching the electronic sample states. Accordingly, these modes may appear with an enhanced intensity in the d^2I/dU^2 spectrum, compared to α^2F deduced from ARPES or density functional theory. Additionally, the IETS spectrum contains contributions from all possible \vec{k} values, while ARPES analyzes specific directions in \vec{k} -space.

6.4.3 Bias dependence of the tunneling barrier height

The bias-dependent contributions of elastic and inelastic tunneling events to the tunnel current also influence the effective decay of the current perpendicular to the sample plane. In order to investigate the different decay at energies where bulk and surface states, respectively, contribute primarily to the sample DOS, the tunnel current as a function of tip-sample separation was recorded for different bias setpoints. In the experiment, the tip position in z was stabilized at $I = 3$ nA and a fixed value of U , before disabling the feedback loop and withdrawing the tip from the stabilization position by $\Delta z = 367$ pm. According to Equations (2.4) and (2.5), the tunnel current decays exponentially and the apparent barrier height can be extracted as

$$\phi = \frac{\hbar^2}{8m_e} \left(\frac{d}{dz} \ln(I) \right)^2 + \frac{|eU|}{2}. \quad (6.16)$$

Here, adding $\frac{|eU|}{2}$ compensates for the shift in Fermi levels of tip and sample relative to each other by the external bias. Effects of parallel momenta according to Equation (6.1) were neglected in this consideration.

The resulting values of ϕ over a bias range between -5 V and 5 V are presented in Figure 6.14 (a). There is a general trend of a reducing barrier height with increasing bias voltage and an increase in the barrier height around $U = 0$ V. At $U \approx 1$ V there is a sudden drop in ϕ by more than 1 eV. This drop marks the onset of the bulk conduction band and can be explained by sample states with $k_{\parallel} = 0$ becoming available for tunneling into this band. Consequently, this plateau in Figure 6.14 (a) is interpreted as the apparent barrier height for states

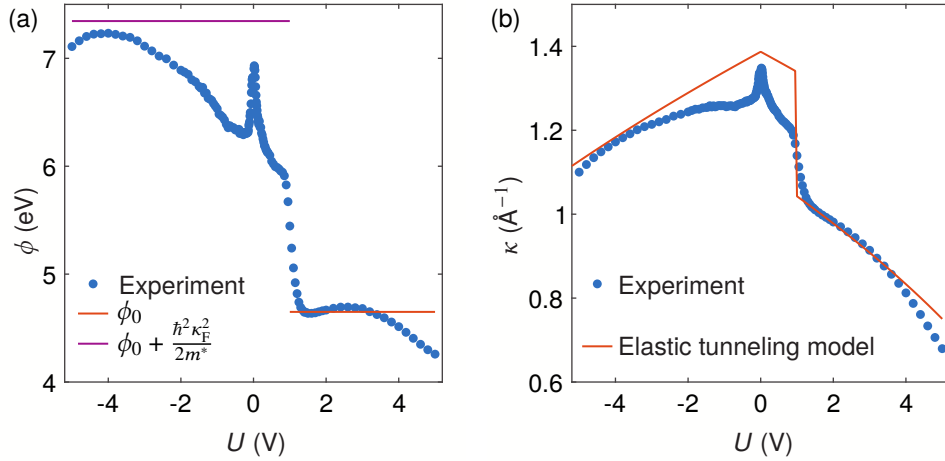


Figure 6.14: (a) Apparent barrier ϕ as deduced from $I(z)$ curves. Sweep distance $\Delta z = 367$ pm; current setpoint for stabilization $I = 3$ nA, tip material: W. (b) Decay constant κ deduced from the experimental data in (a) and the theoretical value calculated based on Equation (6.18).

without a momentum component parallel to the surface plane $\phi_0 = 4.65$ eV. For $U \in [-2.8 \text{ eV}, 1 \text{ eV}]$, there are no states at the $\bar{\Gamma}$ point of the sample and the sample states of minimum parallel momentum are of surface state character. At negative bias, the tunnel current is carried mainly by electrons from states near the Fermi level of the sample [45]. These states in the surface band have a Fermi wave number k_F far away from $\bar{\Gamma}$, enhancing the apparent barrier height. Taking this into account, the enhanced barrier height, calculated as $\phi_0 + \hbar^2 \frac{k_F^2}{2m^*}$ based on the surface state dispersion found in section 6.3 [151], is indicated in Figure 6.14 (a) as well. The measured apparent barrier height approaches this value in the limit of high negative bias values. For bias voltages close to 0 V, the barrier height is markedly enhanced.

To elucidate the origin of this enhancement, we will compare the experimental data to the expected bias dependence of the decay for elastic tunneling. The experimentally acquired decay constant

$$\kappa = -\frac{1}{2} \frac{d \ln I}{dz} \quad (6.17)$$

as a function of U is shown in Figure 6.14 (b) together with the values calculated using the elastic tunneling model from Equation (6.1) by setting $\phi = \phi_0$ and $k_{||} = k_F$ [128]:

$$\kappa = \sqrt{\frac{2m_e}{\hbar^2} \left(\phi_0 - \frac{|eU|}{2} + \frac{\hbar^2 k_F^2}{2m^*} \right)}. \quad (6.18)$$

The model reproduces the experimental results quite well, apart from bias values, where a sizable inelastic contribution to the tunnel current is to be expected: The difference between measured decay constants for elastic tunneling into the bulk conduction band at $U > 1$ eV and into the surface state band at E_F is well reproduced in the model. Away from E_F , the measured decay constant is reduced, which can be explained by inelastic tunneling processes carrying a sizable portion of the tunneling current. In inelastic tunneling processes, momentum parallel to the surface is transferred to phonons and consequently the decay constant is diminished [151]. Towards the onset of the surface state at -2.81 eV, the elastic tunneling model approaches the experimentally observed values of κ again. This can be understood as a reduced contribution of inelastically tunneling electrons to the current as electron-phonon coupling in Be(0001) weakens for negative energies with respect to E_F [79].

Summary of the STS investigation of Be(0001)

To summarize, the electronic properties of Be(0001) as probed by STS were presented in this chapter. Contributions of bulk and surface electrons to the tunneling spectrum were discussed. The nearly isotropic standing waves on Be(0001) were identified as Friedel oscillations of the parabolic $\bar{\Gamma}$ surface state. No experimental indications for the presence of a CDW on this surface were found. Nevertheless, a reduced conductance around the Fermi level was measured. Its origin is the relatively high contribution of inelastic tunneling processes to the total conductance for $|eU - E_F| > 80$ meV. The d^2I/dU^2 spectrum measured on Be(0001) reveals that these inelastic contributions originate from phonon excitations. Conclusively, the Be(0001) surface presents a two-dimensional electron gas that is strongly coupled to phonon modes.

7 Growth of Fe on Be(0001)

In this chapter, the fundamental principles of thin film growth will be discussed. The actual growth of Fe on Be(0001) was studied in dependence of the substrate temperature and the deposited amount of Fe using STM and AES. In the course of this work, the bachelor thesis of Jan-Hendrik Schmidt [66] and the master thesis of Karoline Oetker [153] were supervised. Further, Vojtěch Přikryl and Radek Dao contributed to this study within the framework of their Erasmus program.

7.1 Mechanisms of thin film growth of Fe/Be(0001)

Under ambient conditions, Fe crystallizes in the bcc structure. This structure is referred to as α -Fe. At high temperatures of ~ 910 °C, a transition to the face-centered cubic (fcc)-phase occurs [154]. For pressures of $p > 13$ GPa, there is a transition from the α -phase to an hcp-phase called ϵ -Fe [15, 18, 93]. The lattice constants of the conventional unit cells of these phases are compiled in Table 7.1.

Element	Phase	Lattice	a (pm)	c (pm)
Fe	α	bcc	286	
	γ	fcc	359	
	ϵ (at 19.2 GPa)	hcp	245	393
Be	α	hcp	228	358

Table 7.1: Lattice constants of Be and Fe in different structural phases [14, 24, 155].

Heteroepitactic growth of films on a substrate material poses a possibility to realize structural phases that would not form under equivalent conditions in the absence of the substrate. Thin films of fcc-like Fe were for example realized by growth on Cu(111), which has only a marginal lattice mismatch compared to the γ -phase [156]. Accordingly, the formation of ϵ -Fe on a suitable substrate material can be imagined without the need of externally applied pressure. The

nearest neighbor distance on the hexagonal Cu(111) surface is 255 pm and thus still unapt to simulate the compression in ϵ -Fe. Fe film growth in continuation of a hcp substrate was achieved for example on Re(0001), but in this case with a larger basal lattice constant of $a_{\text{Re}} = 276$ pm [12]. With its smaller surface lattice constant of $a_{\text{Be}} = 228$ pm, Be(0001) is a candidate material to host Fe films in a compressed configuration. A prerequisite to realizing ϵ -Fe grown on Be(0001) is that the growth occurs either pseudomorphically, meaning in direct continuation of the substrate's crystal structure, or in a relaxed hcp-structure with a basal lattice constant of $a \leq 245$ pm. The lattice mismatch between the basal planes of Be and ϵ -Fe is 7.5 %, putting compressive stress on hypothetical pseudomorphic Fe films.

The growth mode of films on substrates depends on which configuration minimizes the total free energy. A wetting of the substrate by an adlayer will be favored if

$$\gamma_s > \gamma_a + \gamma_i + \gamma_e, \quad (7.1)$$

where γ_s and γ_a are the substrate and adlayer free energies per surface unit, respectively, γ_i is the interfacial energy per surface unit, and γ_e is the strain energy in the adlayer per surface unit [155, 157]. This is the prerequisite for the Frank-van der Merwe growth mode, in which each adlayer is fully closed before growth of the next layer commences.

Adversely, for

$$\gamma_s < \gamma_a + \gamma_i + \gamma_e, \quad (7.2)$$

the Volmer-Weber growth mode is favored. In this growth mode, islands of multiple atomic layers in height form on the substrate instead of a closed layer. Generally, interfacial and strain energies may vary based on the adlayer thickness, leading to the Stranski-Krastanov mode: island growth that sets in after a number of full atomic layers are completed. Also in the Volmer-Weber mode, with increasing amount of deposited material, islands will eventually coagulate and fully cover the substrate surface.

Apart from the growth mode as described above, the atomic configuration of films or islands is of interest. Even for crystalline adlayers or islands, there exists another degree of freedom, namely the stacking with respect to the substrate lattice. For Be(0001) there would be the possibility of adatoms to occupy sites that continue the hcp substrate's A-B-A stacking, where atoms in every second layer align along the c -axis. Likewise, overgrown structures may assume the A-B-C stacking, where atoms in every third basal layer match up. In principle, for every additional atomic layer added to a film — or island — two different stacking scenarios exist. Nucleation of adlayers may happen simultaneously in

different adsorption sites, leading to coexistence of differently stacked structures on a surface.

For the Be(0001) substrate, DFT calculations yield $\gamma_{\text{Be}} = 1.8 \text{ J m}^{-2}$, while γ_{Fe} ranges from 2.2 J m^{-2} to 2.7 J m^{-2} for different high-symmetry surface terminations of the bcc-phase [158]. For the fcc Fe(111) and the hcp Fe(0001) surfaces $\gamma_{\text{Fe}(111)} = 2.7 \text{ J m}^{-2}$ and $\gamma_{\text{Fe}(0001)} = 2.9 \text{ J m}^{-2}$ were calculated [159]. This means that — according to the considerations above — a smooth layer-by-layer growth of Fe on Be(0001) can generally not be expected. However, the surface free energies alone are insufficient to thoroughly predict the growth behavior of an element on a substrate as they correspond to equilibrium conditions. MBE growth is a dynamical process, in which adatoms condense on the substrate one at a time and coalesce to ever growing structures. The equilibrium configuration can only form if the mobility of the adatoms is high enough to allow the required dynamics [157]. The surface mobility can be influenced by the temperature during Fe deposition. Even after deposition, the surface morphology can be influenced by post-annealing. It is to note that even for the same substrate temperature, the resulting surface configuration may differ depending on whether the adatoms are deposited at this temperature or whether the temperature is increased after deposition. This is because the energetically preferred state may depend on the number of adatoms or adlayers already present on the surface. Also, the activation energy needed to transfer once-formed structures or clusters into the equilibrium configuration may exceed the thermal energy [157]. Accordingly, a state forming dynamically on a hot substrate for initially small coverages may not be attained if the sample is heated only after cold deposition of the same total amount of deposit.

7.2 Growth for room temperature deposition of Fe

To study the actual growth, Fe was deposited by evaporation from a rod onto the clean Be(0001) surface prepared as described in section 5.3. Values for the deposited Fe amount are given as the number of MLs it would create on Be(0001) in case of pseudomorphic growth with one Fe atom per surface unit cell of Be(0001).

First, an amount of Fe equivalent to 1 ML was deposited at room temperature at a rate of 0.5 ML/min without further post-annealing of the film. The sample was then transferred into the cold VT-STM and imaged at $T = 60 \text{ K}$. Figure 7.1 (a) depicts the resulting sample surface. Compared to the clean substrate surface, separated islands of approximately 10 nm in diameter formed on extended terraces. Along step edges, traced by the broken line, elongated islands

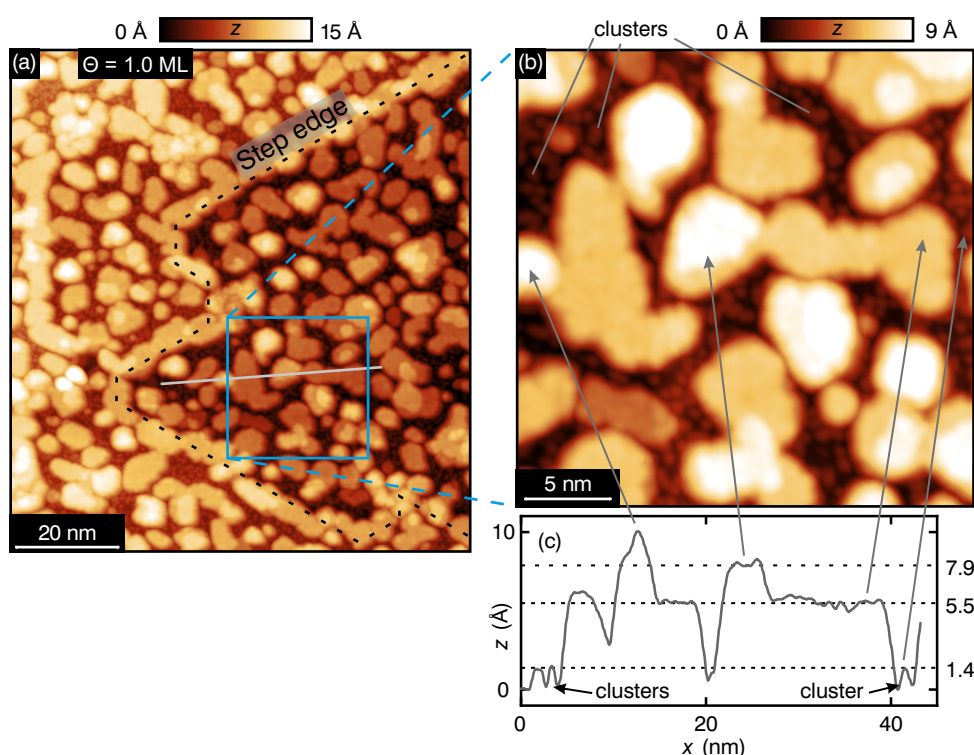


Figure 7.1: (a) Constant-current STM image of 1 ML Fe/Be(0001) deposited at room temperature. The broken line traces a step edge in the substrate. Islands grow on terraces and at step edges. (b) Higher resolution image of the area inside the blue square in (a). Small clusters are visible in between the larger islands. (c) Height profile along the gray line in (a). The apparent heights of clusters and islands are traced with broken lines. Experimental parameters: $I = 1$ nA, $U = 700$ mV, $T = 60$ K, Cr tip.

that trace the step edge are found. In between the islands on the terraces there are small clusters of approximately 1 nm in diameter as can be seen in the zoom-in image in Figure 7.1 (b). A height profile along the gray line in Figure 7.1 (a) is depicted in Figure 7.1 (c). There, $z = 0$ is fixed to the lowest z -value along the line. The corrugation of the clusters measures 1.4 Å. The islands appear most abundantly with a corrugation of approximately 5.5 Å and more scarcely with 7.9 Å. Occasionally, small islands of smaller height can be observed.

Consequently, the islands grow in a three-dimensional fashion with higher layers forming before a closed single layer is achieved, according to the Volmer-Weber mode. Islands with a corrugation of ~ 5.5 Å seem to appear preferentially at an effective coverage of 1 ML. Based on the apparent height difference to the next highest islands of $\Delta z \approx 2.40$ Å, these islands can be interpreted as two layers of Fe. However, there is a substantial variation in the corrugation of islands and

some appear peaked like three-dimensional clusters instead of flat-topped. The appearance of rough islands and clusters indicates that pseudomorphic growth of Fe on Be(0001) does not occur in extended structures for room temperature deposition.

Effects of post-annealing after growth at room temperature

Post-annealing at higher temperatures than the deposition temperature is a common way of achieving more uniformly grown thin films. The increased thermal energy enables deposited atoms to overcome possible energy barriers hindering a rearrangement into a structure that minimizes the total energy. A sample of $\Theta = 1$ ML was subjected to a series of annealing treatments summarized in Table 7.2. The sample was heated on a resistive heating element and then held in the respective temperature range for the quoted duration. The spread in the temperatures is caused by the slow heating-up of the element for low heating powers.

Treatment #	Annealing temperature (°C)	Duration
1	200-240	20 min
2	300-310	30 min
3	350-370	20 min
4	400-415	20 min

Table 7.2: Compilation of the post-annealing treatments applied to a sample of $\Theta = 1$ ML of Fe/Be(0001).

STM images of islands on the sample surface after treatments 2 and 4 are exemplarily shown in Figure 7.2. Compared to the morphology before heating (cf. Figure 7.1), at $T \leq 310$ °C the islands are observed to roughen, as can be seen in Figure 7.2 (a). The granular structure of the islands surface can be seen in the differentiated image. At higher temperatures of up to 415 °C and for longer elapsed annealing duration, smooth areas form in between these granular structures (see Figure 7.2 (b)). The higher-resolution image in the inset reveals standing waves on such a smooth, low lying area. A period of the standing waves of (337 ± 8) pm, or a wave vector of $q = (18.7 \pm 0.4) \text{ nm}^{-1}$, was deduced from the line profile across this standing wave pattern. This wave pattern can be compared to the expected wave number for Friedel oscillations in the $\bar{\Gamma}$ surface state on Be(0001) at $U = 60$ mV as deduced in section 6.3. Comparison yields a good agreement with the expected value of $q = (18.6 \pm 0.2) \text{ nm}^{-1}$ along $[10\bar{1}0]$. The line profile investigated here deviates from the $[10\bar{1}0]$ direction by 25° , but

the data is still comparable because of the small anisotropy of the surface state near E_F of $\sim 2\%$ [29]. Accordingly, the area exhibiting the wave pattern can be interpreted as bare Be(0001).

An increase in temperature allows or accelerates the formation of energetically stable structures on the surface that were hindered by an activation energy at lower temperatures. Instead of the intended smoothing, post-annealing of room temperature-grown islands roughens the surface morphology for temperatures up to 310°C . A further increase of the temperature to 415°C leads to the exposure of Be(0001) in parts of the sample. This can be understood by the gain in energy associated with the lower surface energy of Be compared to Fe [158,

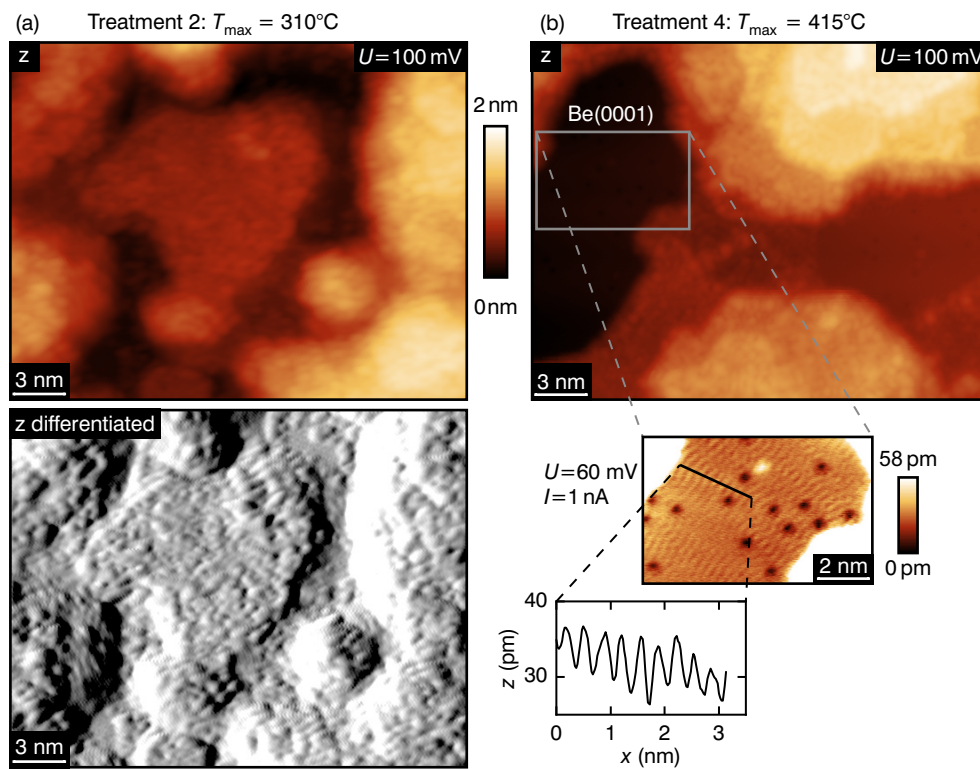


Figure 7.2: Post-annealing of a room temperature-grown sample of $\Theta = 1$ ML Fe/Be(0001). (a) STM image of an island on the sample after annealing treatment 2 at 300°C . The constant-current z contour (top) and its numerical differentiation (bottom) are shown. The island's surface has roughened compared to before the heat treatment. (b) STM image of an island on the sample after annealing treatment 4 at 400°C . Smooth areas appeared between rough island. Experimental parameters: $I = 1$ nA, $U = 100$ mV, $T = 60$ K, W tip. The inset shows a zoom to a smooth area, exhibiting a standing wave pattern of 337 pm (see line profile) characteristic for the Be(0001) surface ($I = 1$ nA, $U = 100$ mV). The data was acquired together with Vojtěch Příkryl.

159]. An increase in temperature furthers the agglomeration of Fe, leaving a higher total surface area of the energetically favored Be(0001).

7.3 Growth for Fe deposition at elevated temperatures

After extended films of Fe/Be(0001) were not achieved by room temperature deposition and subsequent annealing, the deposition of Fe onto a substrate held at elevated temperatures was studied. A higher substrate temperature increases the mobility of deposited atoms and may lead to better ordering during the growth process compared to deposition at room temperature. This is due to the fact that the nucleation density decreases with increasing substrate temperature and consequently larger, continuous films may form instead of many small clusters [160]. The growth at elevated temperatures will be presented with increasing Fe coverage Θ in the following.

7.3.1 Growth for Fe coverages ≤ 0.2 ML

Figure 7.3 (a) shows an image of 0.2 ML of Fe deposited onto Be(0001) at $T = 300^\circ\text{C}$. The temperature was held for 10 min after deposition before removing the sample from the manipulator. Despite the lower coverage, the resulting islands are wider compared to the deposition at room temperature in Figure 7.1. Another qualitative difference lies in the islands' edges that follow the high-symmetry directions of the substrate. Again, elongated islands have formed along a step edge, indicated by an arrow.

A histogram of z evaluated on the large upper terrace is plotted in Figure 7.3 (b). Three peaks can be identified, corresponding to the substrate and to islands of two dominant levels in apparent height. The shoulder on the first peak is caused by clusters scattered between islands. In certain areas these clusters appear especially dense. These areas are identified as warped parts of the surface due to underlying bubble defects originating from Ar^+ sputtering (cf. Figure 5.6). One peak in the histogram, labeled with H1, is measured with a corrugation of 2.96 \AA above the substrate and corresponds to two free-standing islands in Figure 7.3 (a). The second kind of islands, corresponding to peak H2, appears more abundantly and is measured 1.77 \AA higher. Interestingly, this height difference corresponds to one atomic distance in Be along the c -axis ($c/2$) = 1.79 \AA .

A magnified image of one H2 island and the surrounding area is shown in

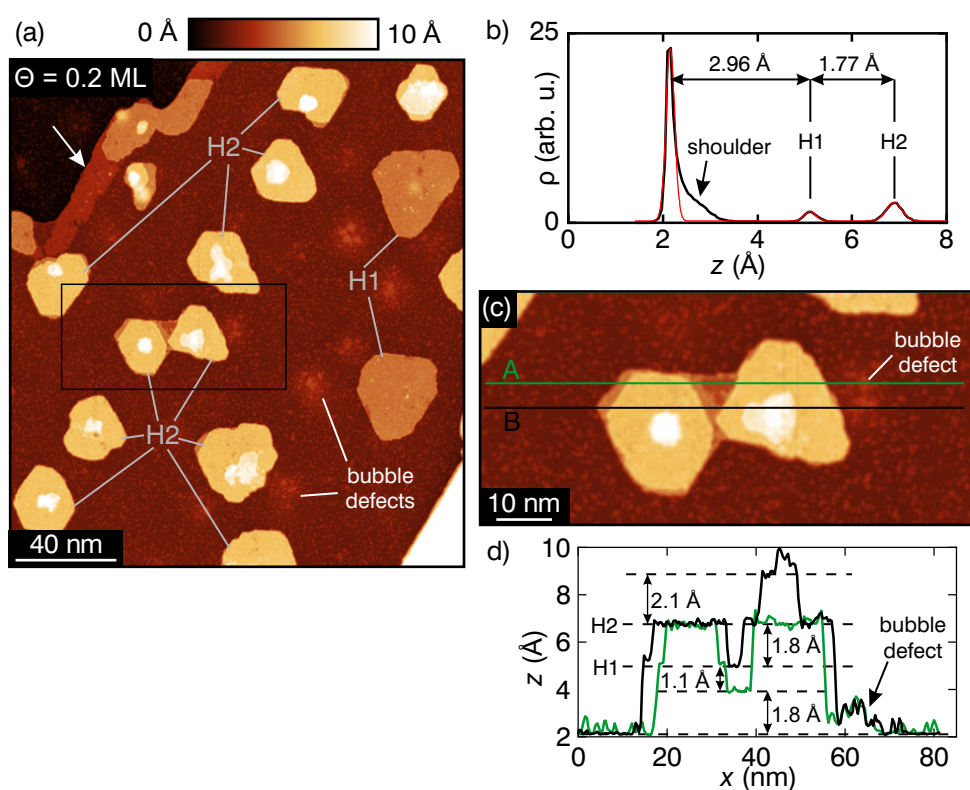


Figure 7.3: (a) Constant-current STM image of a Be(0001) terrace after deposition of 0.2 ML of Fe at $T = 300\text{ }^{\circ}\text{C}$ at a rate of 0.04 ML/min. Elevated regions appear along a step edge (arrow). On the terrace, islands of two dominant levels in apparent height H1 and H2 are found. Additionally, small clusters exist on the terrace, especially densely on bubble defects. Experimental parameters: $I = 0.2\text{ nA}$, $U = 400\text{ mV}$, $T = 40\text{ K}$, Cr tip. (b) Histogram of z evaluated on the large terrace in (a). The three peaks correspond to the substrate and to islands of the two different apparent heights. (c) Magnification of an island in (a) of dominant apparent height H2. (d) Line sections across this island reveal three additional levels of z within this island: A small area of height H1 and additional terraces offset by 1.8 \AA from the substrate and 2.1 \AA from H2.

Figure 7.3 (c). The surface of the island is not uniform in height as multiple nuances in the constant-current STM image reveal. Two line sections across the island are depicted in Figure 7.3 (d). They reveal discrete steps in z . The center of the island measures $\Delta z = 1.8\text{ \AA}$ with respect to the substrate. Further offset by 1.1 \AA is a narrow terrace corresponding to the apparent height H1. The largest areas on the island are of height H2, offset by another 1.8 \AA . And a small terrace approximately 2.1 \AA higher exists. To understand this growth mode, we will in turn examine the clusters scattered across the surface, the stripes growing at step edges of Be(0001) and the free-standing islands in more detail.

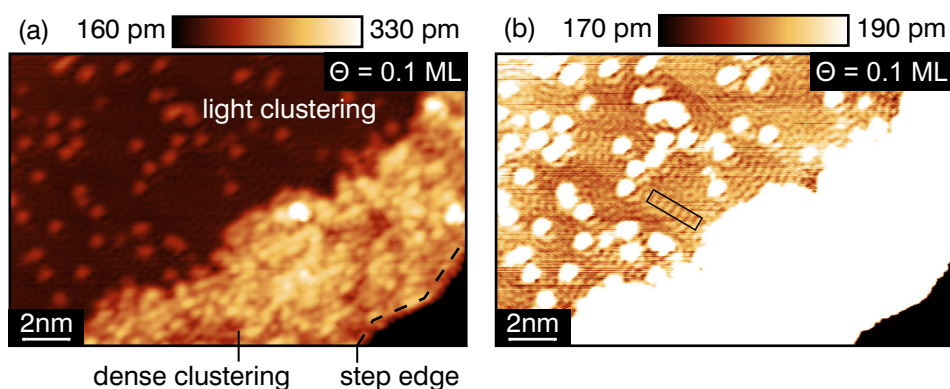


Figure 7.4: Constant-current STM image of a step edge separating Be(0001) terraces with a coverage of 0.1 ML Fe deposited at $T = 300\text{ }^\circ\text{C}$ at a rate of 0.2 ML/min. (a) Color scale chosen to identify clusters. On the upper terrace clusters form densely at the step edge and more sparsely away from it. (b) The same image with the color scale adapted to emphasize details between the clusters away from the step edge. A standing wave pattern with $q = (17.9 \pm 0.4)\text{ nm}^{-1}$, evaluated over six periods inside the marked rectangle can be seen. It is characteristic for Be(0001) surface state electrons scattering from the clusters. Experimental parameters: $I = 100\text{ pA}$, $U = -100\text{ mV}$, $T = 40\text{ K}$, Cr tip.

To examine the clustering, a sample with a lower coverage $\Theta = 0.1\text{ ML}$ of Fe grown at $T = 300\text{ }^\circ\text{C}$ was prepared. Figure 7.4 (a) shows the clustering on the Be(0001) substrate near a step edge. Dense clustering is observed in an approximately 7 nm wide stripe on the upper terrace at the step edge. Further away from the edge, individual clusters of sub-nanometer size can be seen. In Figure 7.4 (b) the color scale is adjusted to reveal details on the upper terrace. A standing wave pattern with $q = (17.9 \pm 0.4)\text{ nm}^{-1}$ is found in between the clusters. This value agrees with the wave vector $q = (18.2 \pm 0.2)\text{ nm}^{-1}$ of Friedel oscillations in the Be(0001) surface state at $U = -100\text{ V}$. In this respect, the surface in between clusters retains the expected substrate properties.

For $\Theta = 0.2\text{ ML}$, the stripes at step edges grow already in multiple layers, as was observed in Figure 7.3. A higher resolution image is shown in Figure 7.5. Films of different apparent height are marked H0-H2. Line profile 1 shows the step height of the substrate of 1.8 \AA . Clusters on the substrate appear with corrugations of up to 0.8 \AA . The films grown in stripes along the step edge have occasional depressions in them. The line profiles 2 and 3 cross the films through such depressions. The film's surface appears rough compared to the substrate. H0 appears with a corrugation of 1 \AA relative to the substrate. H1 has a corrugation of 2.8 \AA and a depression inside it that is offset by 1.8 \AA from the substrate. The apparent height of H2 is 4.6 \AA . Interestingly, the films grow in a layered structure with an apparent height of $1.0\text{ \AA} + n \times 1.8\text{ \AA}$ with the layer

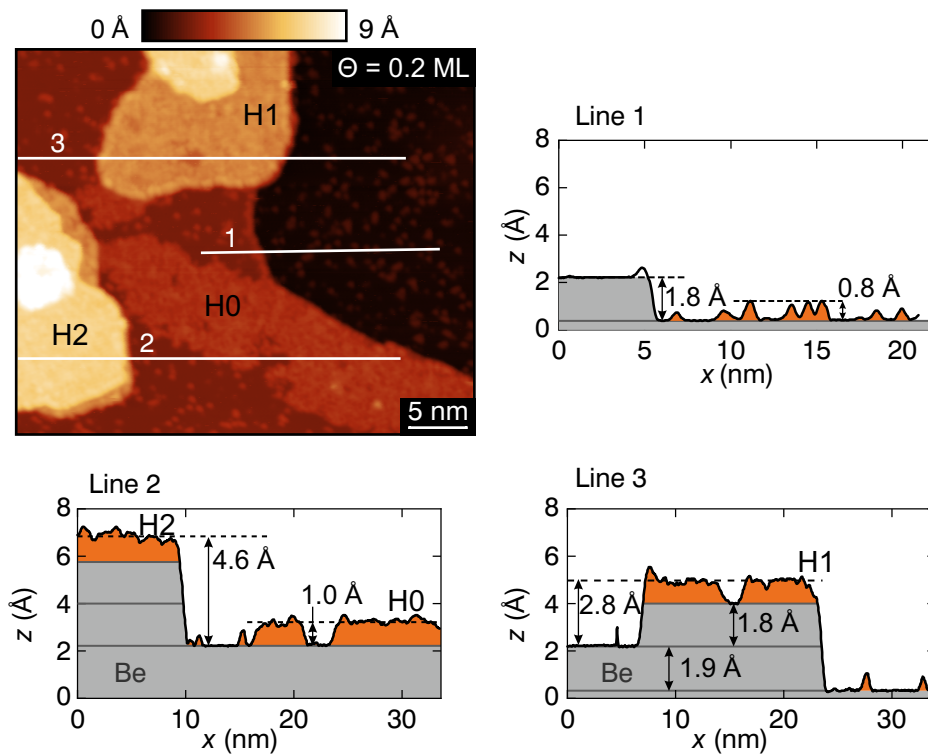


Figure 7.5: Detailed constant-current STM image of the step edge in Figure 7.3. Line profile 1 crosses a step in the Be(0001) substrate of height 1.8 Å. Clusters appear with an apparent height of up to 0.8 Å. Lines 2 and 3 cross various areas where films have formed. The films on the upper terrace appear with an apparent height of ca. 1 Å (orange). Steps of $\Delta z \approx 1.8$ Å are colored in gray and interpreted as layers of Be. Experimental parameters: $I = 1$ nA, $U = 400$ mV, $T = 40$ K, Cr tip, $\Theta = 0.2$ ML.

index $n = 0, 1, 2$. The offset of $\Delta z = 1.8$ Å between layers corresponds to the height of one layer of Be(0001). The areas below the line profiles are colored accordingly.

In order to understand this phenomenon, a comparable analysis of a free-standing island of height H1 is shown in Figure 7.6 (a). Also on this island depressions are evident. The line sections reveal that the depressions in the island's surface appear again 1 Å in depth, same as for the films at step edges. The island itself has an apparent height of 2.8 Å with respect to the substrate, differing by ~ 0.1 Å compared to Figure 7.3. This difference may stem from the higher setpoint current of 1 nA in this case, compared to 0.2 nA in the latter.

With the high apparent barrier height of Be(0001), the current falls off more rapidly with tip-sample separation compared to structures of lower barrier height like Fe. The decay constant of the tunnel current into the vacuum κ_{Be} for the

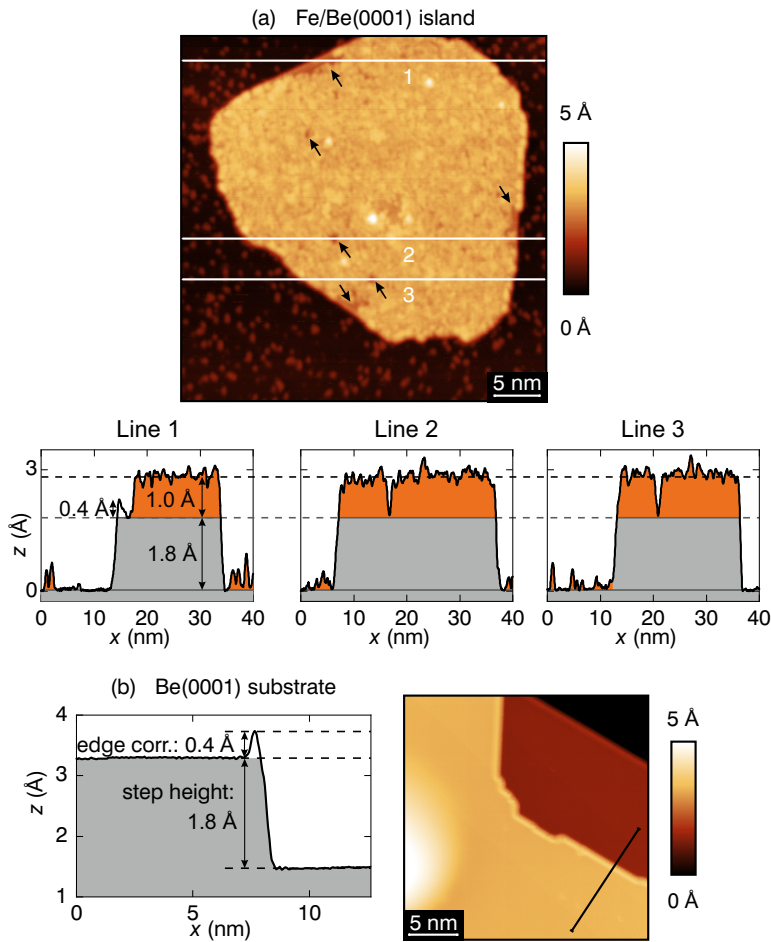


Figure 7.6: (a) Detailed constant-current STM image of a free-standing island grown at $T = 300\text{ }^\circ\text{C}$ with $\Theta = 0.2\text{ ML}$. Large depressions on the island are exemplarily marked by arrows. Line sections across the island including the depressions are shown below. (b) For comparison: STM image taken with the same tunneling parameters on Be(0001) and line section across a step edge. The step height of 1.8 \AA is reflected in the island in (a), and also the ridge of 0.4 \AA at the Be(0001) step is found at the edge of the island as well. Experimental parameters: $I = 1\text{ nA}$, $U = 400\text{ mV}$, $T = 40\text{ K}$, Cr tip.

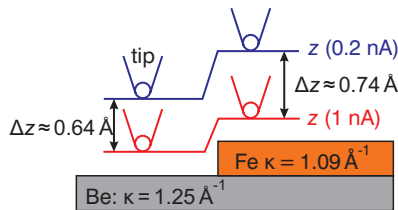


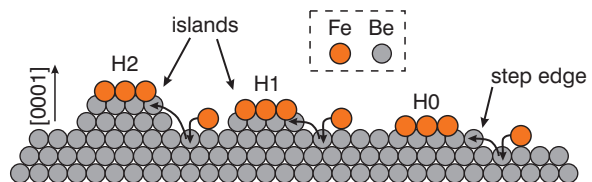
Figure 7.7: Sketch of the influence of a change in current on the constant-current contour across materials with different decay constants. Changing the current setpoint by a factor of 5 from 0.2 nA to 1 nA leads to a decrease in the measured corrugation of Fe on Be(0001) by 10 pm .

Be(0001) substrate was measured in section 6.4.3. At $U = 400$ mV it amounts to $\kappa = 1.25 \text{ \AA}^{-1}$. For Fe, $\kappa_{\text{Fe}} = 1.09 \text{ \AA}^{-1}$ can be deduced from the literature value of the work function $\phi = 4.7$ eV [161]. The situation in STM is schematically depicted in Figure 7.7. When the current is increased from 0.2 nA to 1 nA, the tip approached the sample surface according to $I \propto \exp(-2\kappa z)$ [45]. On Be(0001), the necessary difference is 0.64 \AA , while it is 0.74 \AA for Fe. Consequently, the measured corrugation of Fe films is diminished by 0.1 \AA . This means that the observed corrugation of Fe films in STM with respect to the substrate is highly dependent on the tunneling parameters. Furthermore, the films' surfaces are rough with grains varying by approximately $\pm 0.2 \text{ \AA}$ in apparent height from the mean value.

Line 1 in Figure 7.6 (a) crosses an edge of the island where a wide depression occurs. The height profile exhibits a 0.4 \AA high ridge at this edge. Comparable ridges are found at step edges of bare Be(0001), as can be seen in Figure 7.6 (b). We have seen that the offsets in height between layers of Fe/Be(0001) islands correspond to the step height of Be(0001). This motivates that the islands may indeed consist of layers of Be topped with Fe at the surface. The characteristic ridge observed at an edge of an island where the underlying layer is exposed substantiates this theory. Interesting in this respect is that films on islands have a corrugation of at least 2.8 \AA while thinner films of only 1 \AA exclusively grow at step edges. During preparation of the substrate, free-standing Be islands were never observed to arise during heating. Consequently, the supposed Be content inside the islands seems to stem from the interactions with deposited Fe.

A model for growth of islands with Be content is shown in Figure 7.8. In this model, Fe sinks into the Be(0001) surface and freed Be atoms form islands or migrate to step edges. Fe settles preferentially on these dynamically growing areas, leading to densely covered films of height H0, H1, H2, and so forth. In this model, films of different thickness are expected to have identical physical properties. Tunneling spectra acquired on islands of different height would hence be expected to show similar characteristics.

Figure 7.8: Model for growth of Fe/Be(0001) islands based on intermixing. Deposited Fe atoms sink into the substrate. Be atoms in turn move to step edges or form islands. Fe atoms form more densely on the upper side of step edges or on islands.



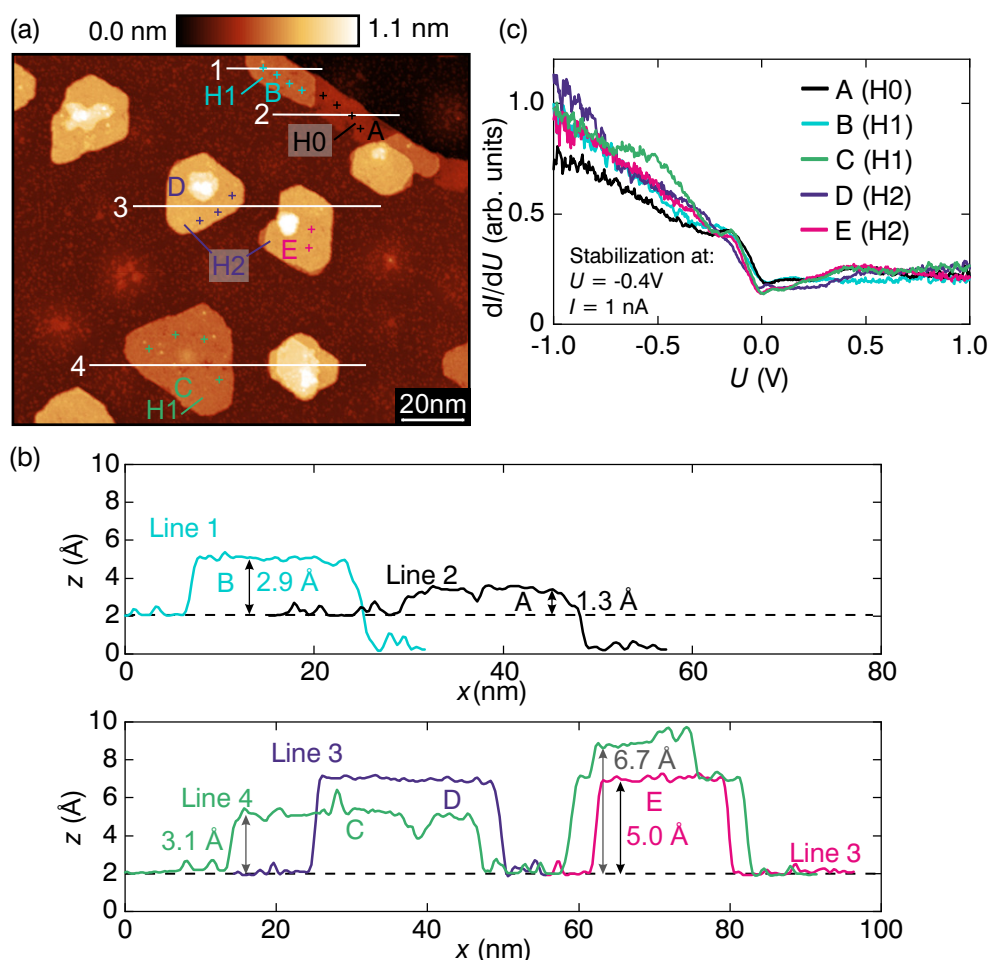


Figure 7.9: Scanning tunneling spectroscopy of Fe/Be(0001) islands and films of various height. (a) Constant-current STM image showing various islands classified as H0-H2 based on their apparent height found in the line profiles shown in (b). Experimental parameters: $I = 0.1$ nA, $U = -400$ mV, $T = 40$ K, Cr tip. (c) STS performed on five different areas labeled A-E in (a). The spectra are averaged over 2-4 points, marked by crosses. Stabilization conditions: $I = 1$ nA, $U = -400$ mV, $U_{\text{mod}} = 20$ mV, $f = 4815$ Hz. The data was acquired jointly with Radek Dao.

STS on Fe/Be(0001) islands and films

Tunneling spectra were acquired on areas of different apparent height, both on free standing islands, and at step edges. The results are displayed in Figure 7.9. Figure 7.9 (a) shows the areas under investigation labeled A-E. Based on the line profiles shown in Figure 7.9 (b), area A is classified as a film of height H0, B and C as H1, and D and E as H2.

The spectra were averaged over several points per area, indicated by crosses

in Figure 7.9 (a). The results are displayed in Figure 7.9 (c). All spectra share common features, namely a steep increase in tunneling conductance for increasing negative bias values, and a relatively constant conductance for positive bias. In spectrum C, there is a hump at around $U = -0.5$ V. Apart from that, no characteristics of specific film thicknesses or differences between free-standing islands and films at step edges can be attested within the measurement accuracy. In contrast to spectra on Be(0001), the conductance is not falling continuously for $0.1 \text{ V} < U < 1 \text{ V}$, but rather constant. Tunneling spectra acquired on Fe(001) exhibit a sharp peak at ~ 0.2 V that is not reflected in the experimental spectra either [162]. In this respect, the spectra of Fe/Be(0001) deviate from both, typical Be(0001) and typical Fe spectra.

We have seen that deposition of Fe at 300°C led to growth of laterally more extended islands compared to room temperature deposition. The vertical spacing of these islands and tunneling spectra suggest that layers of Be exist in these islands.

Effect of post-annealing on Fe/Be(0001) islands

The same sample discussed in the previous section was further annealed for 90 min at temperatures between 380°C and 400°C to investigate the influence of higher temperatures on the growth and if this leads to more extended or better ordered films.

An STM image of an island after the annealing is shown in Figure 7.10. The surface morphology of the island differs from the state before annealing. Most of the island's surface is smooth with rough areas on its rim and in its center. The inset of Figure 7.10 (a) shows a zoom-in on the island's surface with an adjusted color scale. Standing waves with $q = (19.2 \pm 0.4) \text{ nm}^{-1}$ are revealed on the smooth area. This value deviates from the Friedel oscillations on pristine Be(0001) with $q = 18.5 \text{ nm}^{-1}$ by only 4%.

Figure 7.10 (b) depicts a height profile along the white line in Figure 7.10 (a). The smooth part of the island lies 5.36 \AA above the substrate, corresponding to exactly three atomic steps in Be along the principal crystallographic axis. The disordered part at the edge of the island appears with an apparent height of 6.10 \AA . This indicates that the island's surface is actually Be(0001), which is a peculiar observation as free-standing islands were not observed on the substrate prior to Fe deposition.

Figure 7.10 (c) depicts the simultaneously acquired dI/dU -image of the island and the surrounding substrate. We see that the annealing lowered the density of clusters on the substrate surrounding the island. The dI/dU values measured on the island show more spatial variations compared to the lower lying substrate,

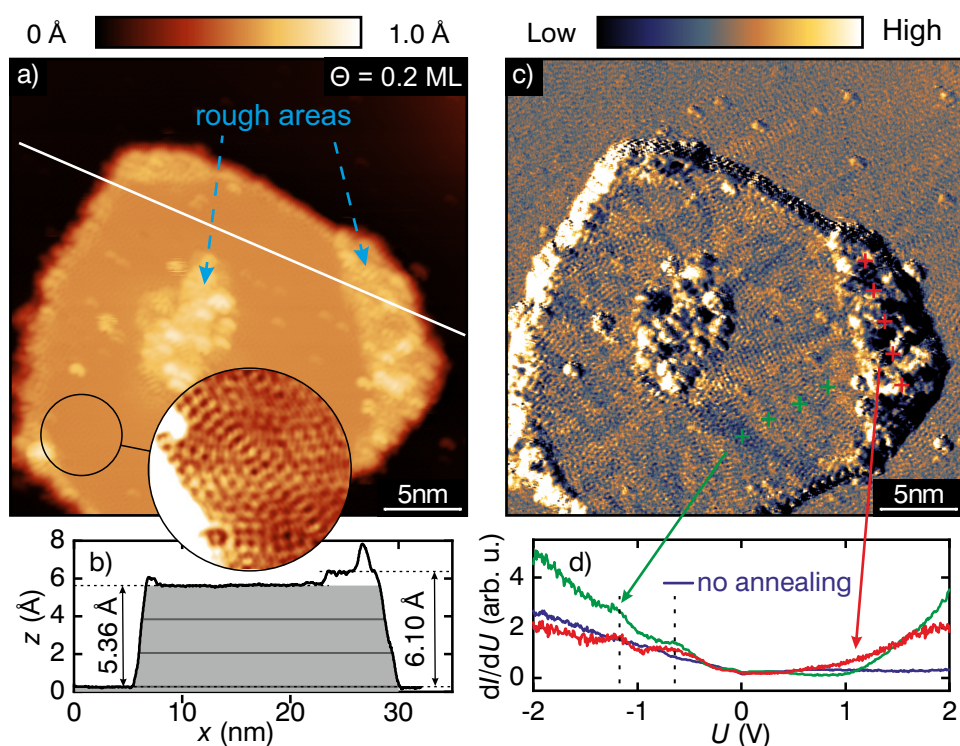


Figure 7.10: Effect of higher temperature annealing on islands. (a) An island observed after deposition of 0.2 ML Fe at $T = 300\text{ }^{\circ}\text{C}$ and annealing to $380\text{ }^{\circ}\text{C}$ - $400\text{ }^{\circ}\text{C}$ for 90 min. The island exhibits disordered apparent elevations in the center and at edges. The inset highlights standing waves observed on the smoother part of the island. (b) Height profile across the line indicated in (a). (c) Differential conductance map acquired simultaneously with (a). The deviations of dI/dU on the island are considerably larger than on the surrounding substrate. Experimental parameters: $I = 1\text{ nA}$, $U = 40\text{ mV}$, $U_{\text{mod}} = 40\text{ mV}$, $f = 4185\text{ Hz}$, $T = 40\text{ K}$, Cr tip. (d) Tunneling spectra averaged over several points on the smooth part of the island (green) and on the elevated edge (red). For comparison, a spectrum taken on island "C" in Figure 7.9 before post annealing is shown (blue). Broken lines mark peaks in the spectrum after annealing. Stabilization conditions: $I = 1\text{ nA}$, $U = -400\text{ mV}$, $U_{\text{mod}} = 20\text{ mV}$. The data was acquired jointly with Radek Dao.

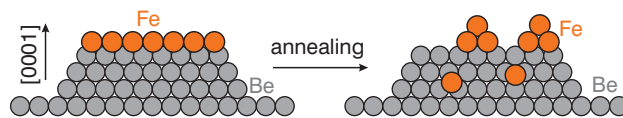
indicating differences in the electronic structure, despite the observed standing wave pattern on the island's surface.

Scanning tunneling spectra obtained on the Be(0001)-like parts of the island (green) and on the rough edge of the island (red) are shown in Figure 7.10 (d). The increase of conductance at $U \approx 1\text{ V}$ in the green curve is a characteristic of Be, marking the onset of the bulk conduction band. This sudden increase is not found in the red curve. Both curves differ from the spectrum obtained before annealing. For comparison, a spectrum acquired on island C in Figure 7.9 is displayed in blue. On the negative bias side it is similar to the spectrum acquired

on the island's edge after annealing. Both spectra taken after annealing display peaks, indicated by broken lines, on the negative bias side that were not found before annealing and do not occur for pristine Be(0001), either [123]. These peaks may originate from electronic states of the tip as the tip's microscopic configuration has changed in between the experiments.

The combined observation of the characteristic standing wave pattern, spectroscopic evidence, and a step height of multiple atomic distances indicates that Fe deposition onto Be(0001) followed by annealing to $T > 380^\circ\text{C}$ produces islands on the surface with a terminal layer of high Be content. The deviations in dI/dU may be a hint on foreign atoms in these islands, possibly Fe. Apparently, deposition at 300°C leads to the creation of larger islands of well defined height and shape compared to room temperature deposition. But annealing at higher temperatures eventually overcomes the activation energy to bare Be(0001) in favor of Fe. A model of this interpretation of the growth is depicted in Figure 7.11. Fe incorporation into the island's volume could explain the observed deviation of 4% in the standing wave period compared to the pristine surface due to doping or modification of the effective electron mass. For example different ARPES studies found significant variations in the effective mass of the Be(0001) $\bar{\Gamma}$ surface state between $1.19 m_e$ and $1.27 m_e$ [86, 142]. Even during deposition at $T \leq 300^\circ\text{C}$, this diffusion may already take place at a lower rate.

Figure 7.11: Model for the effect of annealing at $T > 380^\circ\text{C}$ on Fe/Be(0001) islands grown at $T = 300^\circ\text{C}$. Fe atoms cluster or diffuse into the islands, baring areas of Be(0001) at the island's surface.



7.3.2 Ordered Fe/Be(0001) films forming for Fe coverages $\geq 0.5 \text{ ML}$

The deposition temperature will be limited to approximately 300°C in the following to allow for growth of extended structures, and the heating after deposition will be kept as short as possible to prevent the grown structures from disintegration. The heater is switched off directly after deposition and the sample is taken from the heating stage in under five minutes. The morphology of the films was studied in dependence of Fe coverage with the goal of identifying extended, ordered films.

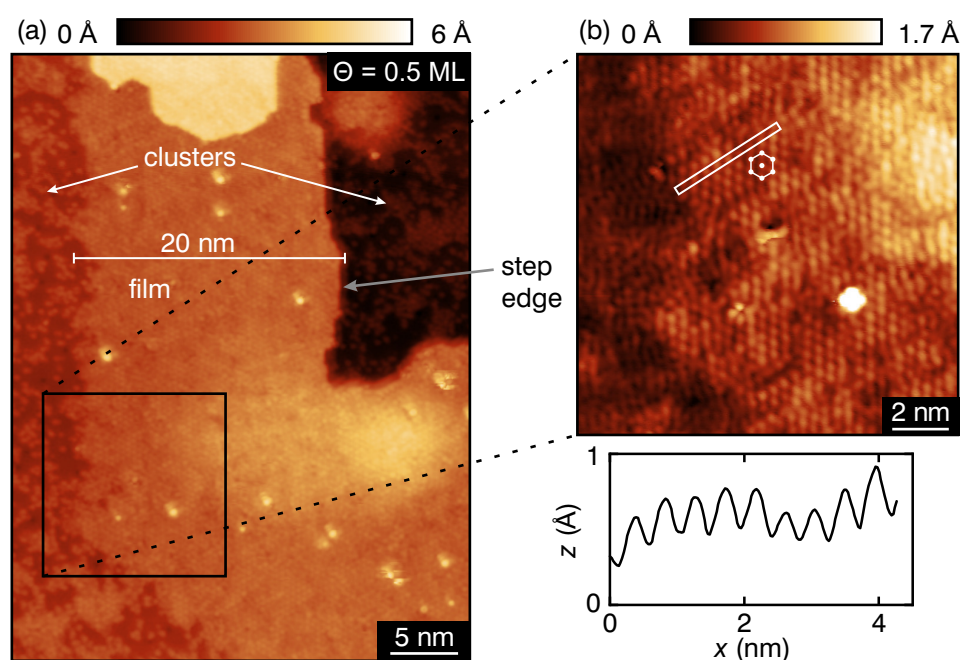


Figure 7.12: (a) Constant-current STM image of a step edge in the Fe/Be(0001) surface after deposition of 0.5 ML of Fe at $T = 300\text{ °C}$. A closed film, approximately 20 nm wide has formed at the edge. On the terraces left and right of this edge, the growth occurred in clusters. Experimental parameters: $I = 100\text{ pA}$, $U = 600\text{ mV}$, $T = 60\text{ K}$, Cr tip. (b) Higher resolution STM image of the border between cluster and film growth. A local ordering in a hexagonal pattern is visible. A line section of the image across the pattern is visible below. The oscillations in the z -corrugation have a period of $(450 \pm 20)\text{ pm}$. Experimental parameters: $I = 1\text{ nA}$, $U = -100\text{ mV}$, $T = 60\text{ K}$, Cr tip.

Deposition of 0.5 ML of Fe

Figure 7.12 (a) depicts a step edge on the sample surface after deposition of $\Theta = 0.5\text{ ML}$ of Fe. The first striking feature of this step edge is that it shows kinks and notches, in contrast to the usually straight running step edges on the Be(0001) surface after the cleaning procedure described in section 5.3. Discontinuous clusters are found on both sides of the step edge. In between, a continuous film of approximately 20 nm in width exists on the upper terrace, following the course of the step. In this respect the growth behaves comparable to the sample with a coverage of only 0.2 ML (cf. Figure 7.5). The stripe grown at the step edge grew wider with the increased deposited amount, and the substrate farther away is more densely covered with small clusters.

But the structure of the film along the step edge has changed. In Figure 7.12 (b), the border between cluster and film growth on the upper terrace is

shown in more detail and with tunneling parameters ensuring a closer tip-sample separation. On the continuous film, dots appear that form an ordered hexagonal pattern (indicated by a white hexagon). The pattern aligns with the directions of step edges and accordingly with the high-symmetry directions of the Be(0001) substrate. A height profile measured along these locally ordered dots reveals a periodicity of (450 ± 20) pm, approximately twice the basal lattice constant a of Be. Hence, for deposition of at least 0.5 ML of Fe at 300 °C, an ordered growth reflecting the underlying Be(0001) lattice commences. The evolution of this growth with increasing Fe coverage is presented in the following.

Deposition of 1 ML of Fe

The Fe coverage was increased to $\Theta = 1$ ML. On extended terraces, this leads to the growth of stepped pyramidal islands as can be seen in Figure 7.13 (a). The islands exhibit up to six consecutive terraces (labeled with numbers) that are separated by steps of atomic height. The basal layer is labeled "B". This layer shows a rougher corrugation in z compared to the islands, as can be seen in the exemplary line profile (green). A possible explanation of this roughness could be that the deposited Fe does not exclusively form islands but also resides on or in the basal layer. This can be understood as a consequence of the clustering observed for lower Fe coverages growing denser.

A histogram of z -values measured on the labeled island in the upper left corner and the basal layer around it is plotted in Figure 7.13 (b). The frequency of occurrence of data points ρ for a certain z -value is given in arbitrary units. The peaks in the histogram corresponding to the basal layer and the five labeled layers of the island are indicated accordingly. The peak positions z_{abs} as determined by Gaussian fits and the height differences z_{rel} between them are compiled in the adjacent table. It is apparent that the layers of the island are not uniformly spaced. The steps between second and third, as well as between third and fourth layer measure approximately 180 pm, coincident with the lattice spacing in Be. The other step heights range from 159 pm to 223 pm, well in the range expected for monatomic steps. The large deviation of consecutive step heights motivates that the growth mechanism of islands may be more complex than pure layer-by-layer growth with a single preferred stacking.

Figure 7.13 (c) depicts zoomed STM images of consecutive terraces of layers B to 4. Hexagonally ordered patches can be seen on layers 3 and 4. On layers 1 and 2, the ordering can be seen to emerge in patches spanning only a few lattice points. The basal layer appears completely disordered.

The island in the top left corner of Figure 7.13 (a) was used as the basis for an exemplary spectroscopic study of the Fe/Be(0001) system. Constant-

current z and dI/dU data obtained at a bias voltage of $U = -100$ mV is shown in Figure 7.14 (a) and (b), respectively. Layers 1 and 2 exhibit a differential conductance similar to the basal layer at this bias voltage. Layers 3 and 4 show a higher dI/dU and layer 5 appears with an intermediate level in dI/dU . Important to note is, that the ranges of measured dI/dU values on all areas are strongly overlapping. This indicates that the spread in dI/dU found on an individual layer is greater than the difference between average values for different layers.

Tunneling spectra in the range of -1.5 V $< U < 1.5$ V acquired on all five layers of the island in addition to the basal plane are shown in Figure 7.14 (c). The spectra acquired on the basal plane and the two consecutive layers are similar to the spectra measured on islands for $\Theta = 0.2$ ML of Fe (cf. Figure 7.9). Spectra

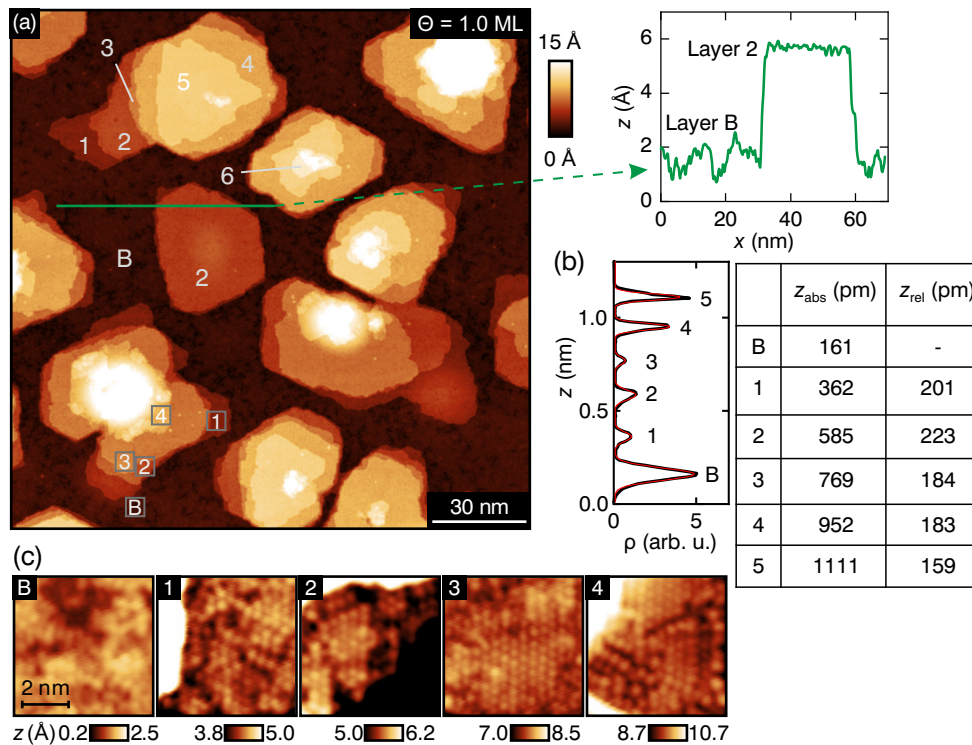


Figure 7.13: (a) Constant-current STM image of Be(0001) after deposition of 1.0 ML of Fe at $T = 300$ °C at a rate of 0.24 ML/min. The line section shows the roughness of layer B compared to an island. (b) Histogram of z measured on and around the stepped island in the top left corner of (a) with a fit of six Gaussians to it (red). The resulting peak positions z_{abs} and differences between consecutive peaks z_{rel} are compiled in the table. The maximum standard deviation of the peak positions is 3 pm. (c) Zoom-ins on a stepped Fe/Be(0001) island in (a) showing a local ordering on consecutive terraces. Experimental parameters: (a) $I = 0.2$ nA, (c) $I = 1$ nA; $U = -200$ mV, $T = 40$ K, Cr tip. The data acquisition was done jointly with Radek Dao.

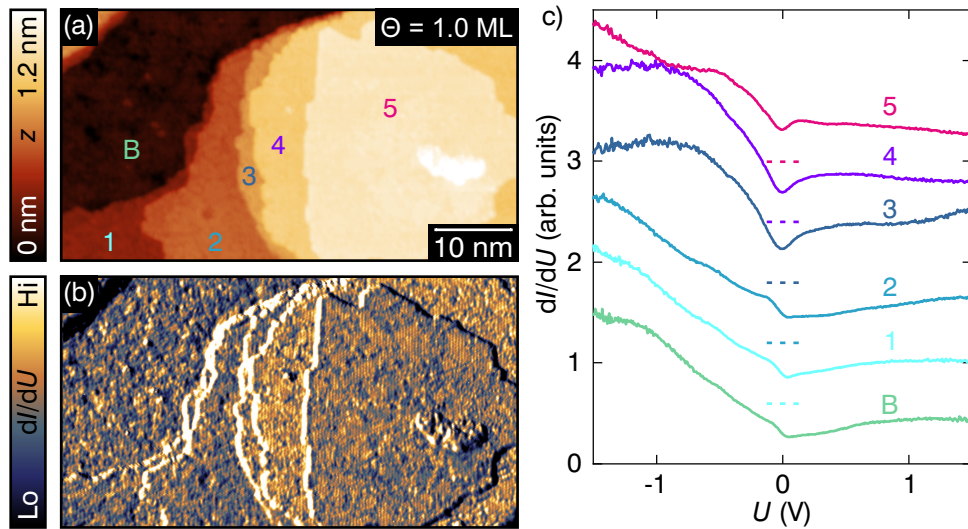


Figure 7.14: STS on a stepped Fe/Be(0001) island. Constant-current STM image (a) of an island with a maximum height of five atomic layers relative to the basal plane B and the simultaneously acquired differential conductance (b). Local layer heights are indicated by numbers. Parameters: $U = -100$ mV, $I = 1$ nA, $T = 40$ K, $U_{\text{mod}} = 40$ mV, $f = 3667$ Hz, Cr tip. (c) Tunneling spectra acquired on all the areas labeled in (a). The spectra are vertically offset for clearer separation. Broken lines indicate offset zero points in dI/dU . Stabilization conditions: $I = 1$ nA, $U = -100$ mV, $U_{\text{mod}} = 40$ mV, $f = 3667$ Hz. The tunneling spectra were acquired by Radek Dao.

of layers 3 and 4 are similar to each other but deviate from spectra B, 1, and 2 by a stronger slope for negative bias values. Spectrum 5 resembles spectrum 4 apart from a rising flank at $U < -1$ V. None of the spectra is similar to the spectrum of pristine Be(0001) in Figure 6.6 (a) with a strongly increasing conductance at the bulk conduction band onset near $U \approx 1$ V. The height of the first layer with respect to the Be(0001) substrate can not be ascertained as the substrate is densely covered by Fe clusters. Consequently, the growth of Fe on Be(0001) at elevated temperatures of $T \approx 300$ °C takes place on an extended basal plane in addition to island growth.

Influence of prolonged annealing on the growth mode

In order to understand the dynamic processes governing the growth, this same sample with a nominal coverage of $\Theta = 1$ ML of Fe was further annealed at the deposition temperature of $T = 300$ °C for a total of 3.5 h. The surface morphologies before and after annealing are compared in Figure 7.15 (a) and (b). While individual stepped islands on a common basal layer can be seen

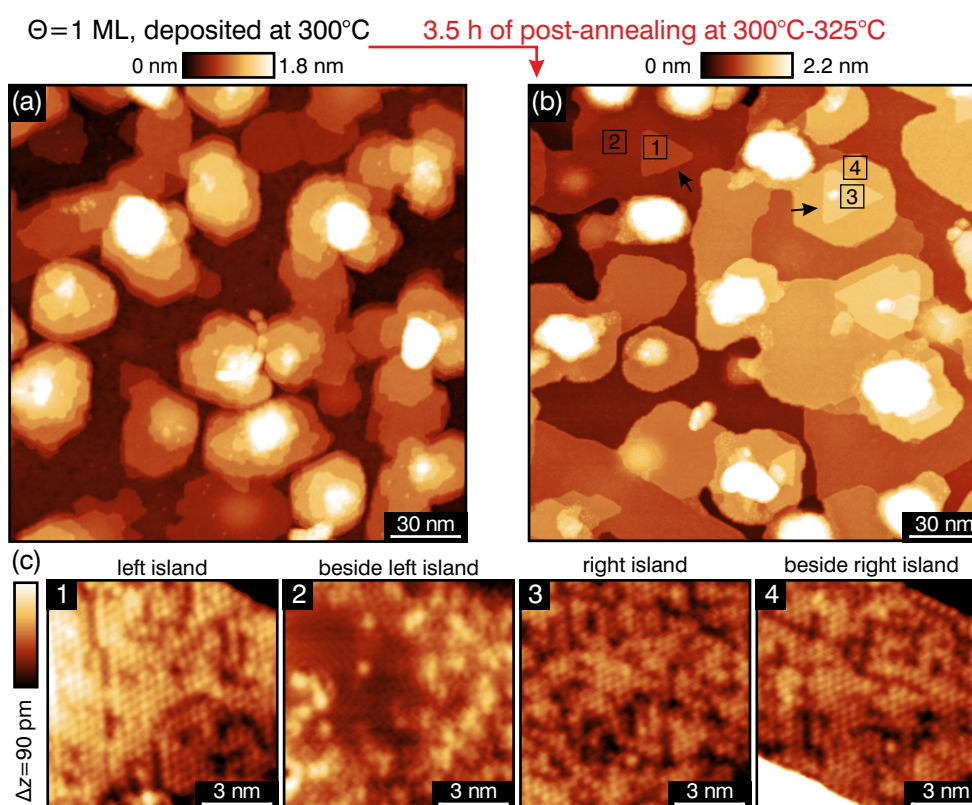


Figure 7.15: Changing morphology with longer heating after Fe deposition. (a) Constant-current STM image of $\Theta = 1$ ML Fe on Be(0001) deposited at $T = 300^\circ\text{C}$. (b) The same sample after additional annealing at $300^\circ\text{C} - 325^\circ\text{C}$. Individual islands have merged to form extended structures. Occasionally triangular islands formed on top (marked by arrows). (c) Higher resolution STM images of the triangular islands and the underlying terraces. Both islands exhibit local order in the surface (panels 1 and 3). The left island is surrounded by a terrace showing no order (panel 2), while the terrace below the right island is ordered as well (4). Experimental parameters: (a) $U = 400$ mV, $I = 200$ pA, (b) $U = 400$ mV, $I = 100$ pA, (c) $U = -200$ mV, $I = 1$ nA; $T = 40$ K, Cr tip.

before annealing, after annealing more interconnected, and wider structures are found.

Occasionally, islands with straightened edges are observed after the annealing, culminating in triangular islands indicated by arrows in Figure 7.15 (b). The formation of triangular islands on hexagonally ordered substrates is a common observation. It is driven by two different atomic configurations occurring for step edges that meet at an angle of 120° . If one edge configuration is energetically favorable over the other, those will end up longer during growth with the ultimate result of triangular islands and step edges meeting at 60° [163].

Detailed images, acquired with higher resolution, of the triangular islands and the lower lying surroundings are shown in Figure 7.15 (c). Both islands show patches of hexagonally ordered areas on their surface. In case of the left island (panel 1), the surrounding area shown in panel 2 appears disordered. The right island in panel 3 on the other hand grows on top of a likewise ordered layer (panel 4).

We have seen that prolonged annealing at the deposition temperature of 300 °C changes the surface morphology. It furthers the interconnection of islands and favors wider terraces. Disordered and hexagonally ordered surface areas coexist. Some islands assume a triangular shape during the prolonged annealing, independent of them growing on top of an ordered or a disordered area.

The electronic properties of the surface after annealing were probed by STS. Constant-current z and dI/dU data of an island are shown in Figure 7.16 (a) and (b), respectively. The differential conductance image shows contrast between different areas on the island. The dI/dU contrast is not singularly dependent on the apparent height of the area as can be seen in the line profile. A higher resolution image in Figure 7.16 (c) reveals ordered structures on the bright part of the terrace. On the basal layer in close vicinity of the island, rather homogeneously appearing areas can be identified (highlighted by a green circle in Figure 7.16 (b)). The tunneling spectra presented in Figure 7.16 (d) reveal that this homogeneous area shows spectroscopic signatures of Be(0001), namely the surging conductance when the bias crosses 1 V and tunneling into the bulk conduction band of Be becomes possible (cf. section 6.2). This is in contrast to the spectrum observed on the basal layer before annealing shown in Figure 7.14. Also, the investigated areas on the island, marked by black and blue circles, still lack this feature after the prolonged annealing.

This behavior has implications for the interpretation of the observed growth mode. Be(0001) is first covered at $T = 300$ °C but laid bare again in places after prolonged annealing at this same temperature. Apparently, bare Be(0001) is energetically favorable but the diffusion of Fe is too slow at this temperature to yield only island growth. Instead, during deposition, the sample assumes a metastable state with locally varying degrees of atomic order that slowly disintegrates when maintaining the temperature for longer periods of time.

Growth of extended films for higher Fe coverages

The density of ordered patches forming during deposition and their size both increase with increasing Fe coverage. Figure 7.17 (a) depicts the Be(0001) surface after deposition of 1.6 ML of Fe at 300 °C. Instead of compact islands on a disordered basal layer, the substrate is covered by a continuous film of

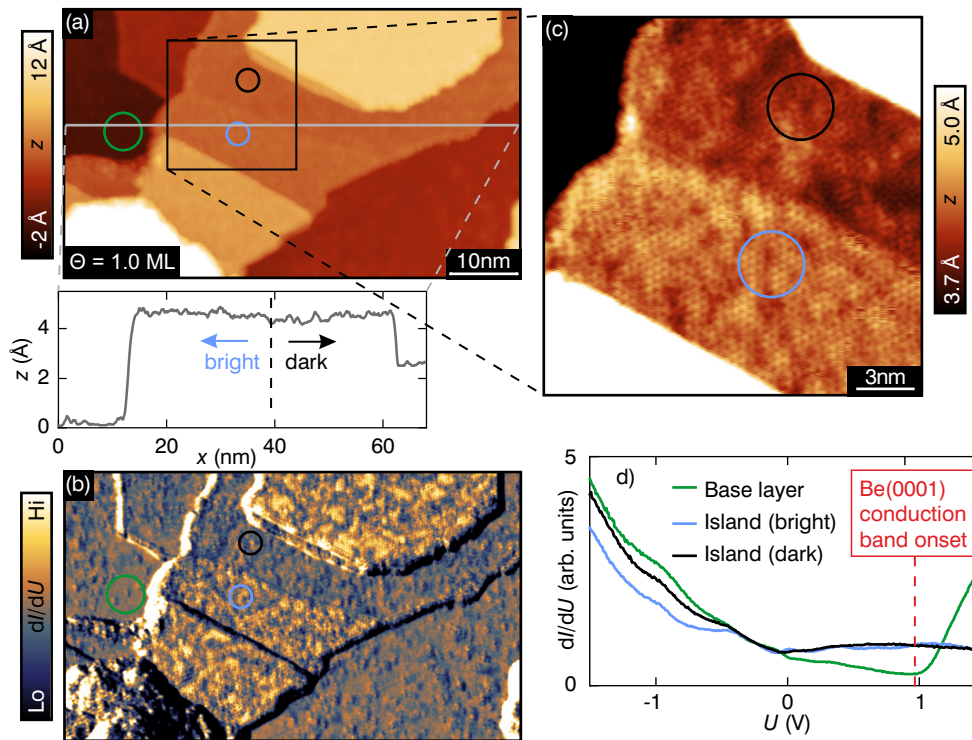


Figure 7.16: STS on a sample of 1 ML Fe/Be(0001) after annealing at 300 °C-325 °C for 3.5 h. (a) Constant-current STM image of an island at a step edge after the annealing. (b) Simultaneously acquired dI/dU channel. One terrace of an island appears split into two dI/dU levels (cf. gray line profile). Parameters: $U = -200$ mV, $I = 1$ nA, $T = 40$ K, $U_{\text{mod}} = 40$ mV, $f = 3667$ Hz, Cr tip. (c) Higher resolution image of the areas appearing bright and dark in (b). A short-range ordering on the bright area is visible. Parameters: $U = -400$ mV, $I = 1$ nA, $T = 40$ K, Cr tip. (d) Tunneling spectra acquired on the basal layer and on areas of the island appearing bright and dark in dI/dU , respectively. Stabilization conditions: $I = 1$ nA, $U = -400$ mV, $U_{\text{mod}} = 40$ mV, $f = 3667$ Hz. The Investigated areas are marked with colored circles in (a-c). After the annealing, the tunneling spectrum acquired on the basal layer exhibits an increase in dI/dU at the onset of the Be(0001) bulk conduction band. The experiment was carried out by Radek Dao.

varying local thickness. The magnified image in Figure 7.17 (b) shows the microscopic surface morphology on extended terraces. Both terraces exhibit a patched hexagonal superstructure with a lattice constant of $a_{\text{FeBe}} \approx 450$ pm, that was observed to start forming at $\Theta = 0.5$ ML in Figure 7.12. The lattice constant is twice as large as the basal lattice constant of Be. Furthermore, the ordered patches are oriented parallel to high-symmetry directions of the substrate.

Apparently, the hexagonal crystal structure of Be(0001) is reflected in the film grown at elevated temperatures, although the film does not grow pseudomorphically. To characterize the ordered structures in the Fe/Be(0001) films

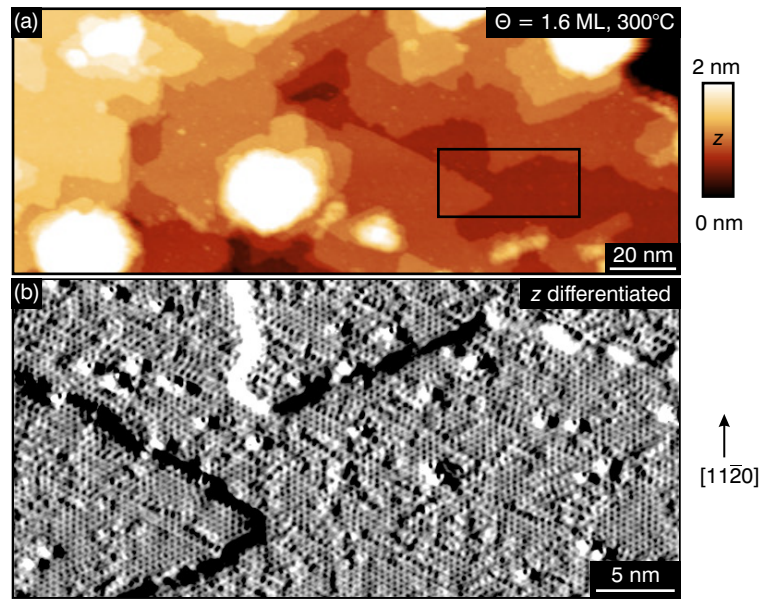


Figure 7.17: (a) Constant-current STM image of 1.6 ML of Fe on Be(0001) deposited at $T = 300^\circ\text{C}$ at a rate of 0.23 ML/min. A magnified image of the low lying terraces inside the black rectangle is shown in (b). Depicted is the numerically differentiated z -signal after application of a Gaussian filter of 2σ . Hexagonal ordering is observed even on an extended terrace. Experimental parameters: (a) $I = 50\text{ pA}$ (b) $I = 1\text{ nA}$; $U = -200\text{ mV}$, $T = 40\text{ K}$, Cr tip. The data was acquired together with Jan-Hendrik Schmidt.

in terms of symmetry and commensurability with the substrate, high-resolution STM images with differing directions of the fast scan axis were acquired. In STM, the slow scan direction is prone to distortions due to random movements of the tip relative to the sample that are induced by thermal expansion. Avoidance of distortions is important to exclude the misinterpretation of, for example, a distorted bcc(110) surface as a hexagonal lattice or vice versa. Three images with the fast scan direction successively rotated by 60° are shown in Figure 7.18 (b). It is evident that the (horizontal) fast scan direction is nearly parallel to high-symmetry directions of the structures in the film in all three cases.

Line profiles along all three directions of high symmetry were extracted from the scans and fit with a sine function to extract the periodicities λ_i in these directions. The results of $\lambda_1 = (455 \pm 2)\text{ pm}$, $\lambda_2 = (459 \pm 3)\text{ pm}$, and $\lambda_3 = (454 \pm 5)\text{ pm}$ show that the structure is indeed a regular hexagonal lattice. Within the measurement accuracy, the lattice constant measures twice the lattice constant of Be(0001): $a_{\text{film}} = 2a_{\text{Be}} = 456\text{ pm}$. Consequently, it can be concluded that commensurable (2×2) superstructures exist locally inside the film.

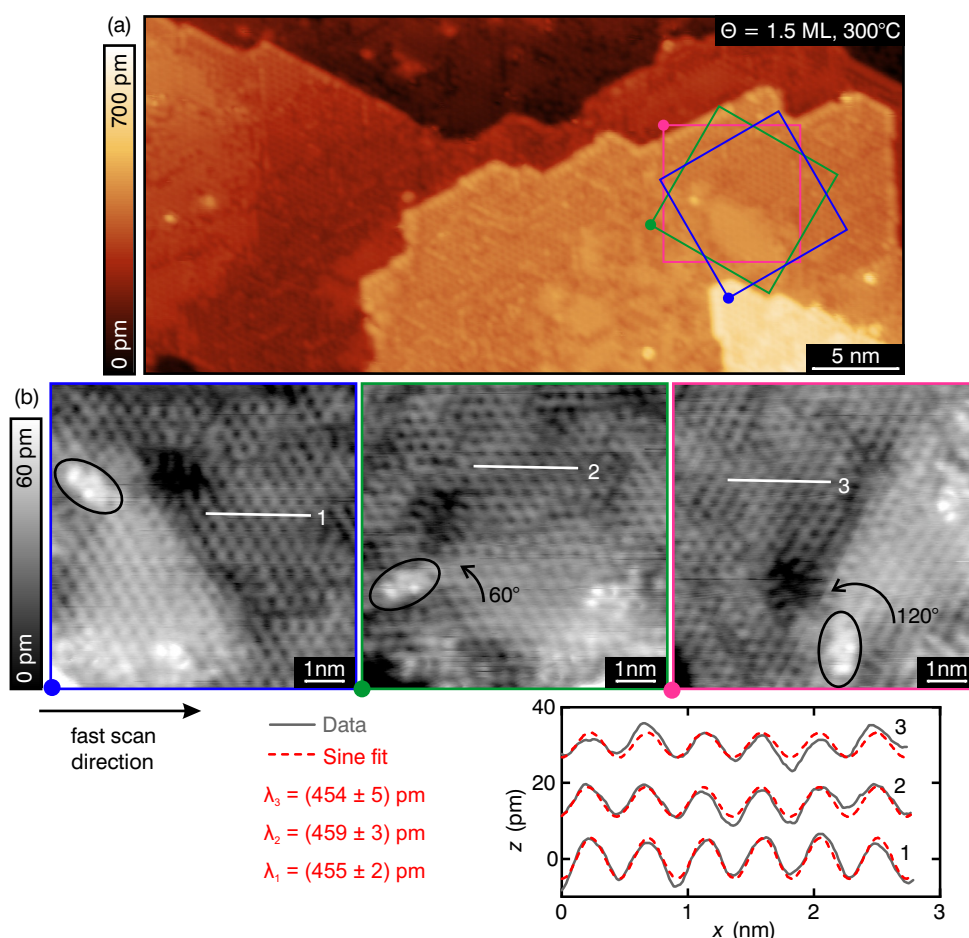


Figure 7.18: (a) Constant-current STM image of 1.5 ML Fe on Be(0001) deposited at 300 °C at a rate of 0.13 ML/min. Experimental parameters: $I = 1$ nA, $U = 400$ mV, $T = 60$ K, Pt/Ir tip. (b) Three higher resolution STM images ($I = 2$ nA; $U = -200$ mV) of an area in (a) with the fast scan direction incrementally changed by 60°. An impurity is encircled for orientation. The fast scan directions are nearly parallel to high-symmetry directions of the ordered surface structure. Height profiles taken along the three high-symmetry directions are shown below in gray with sine fits to the experimental data in red. The fitted periods λ_i of the lattice in the three directions are indicated.

LEED investigation of Fe/Be(0001)

A LEED experiment was performed to further characterize the superstructure forming during Fe deposition at 300 °C. Figure 7.19 (a) and (b) show diffraction patterns of clean Be(0001) and 2 ML of Fe/Be(0001), respectively, for a beam energy of 80 eV. The clean Be(0001) surface shows only the hexagonal first-order (1×1) diffraction spots of the reciprocal atomic lattice. For the Fe covered

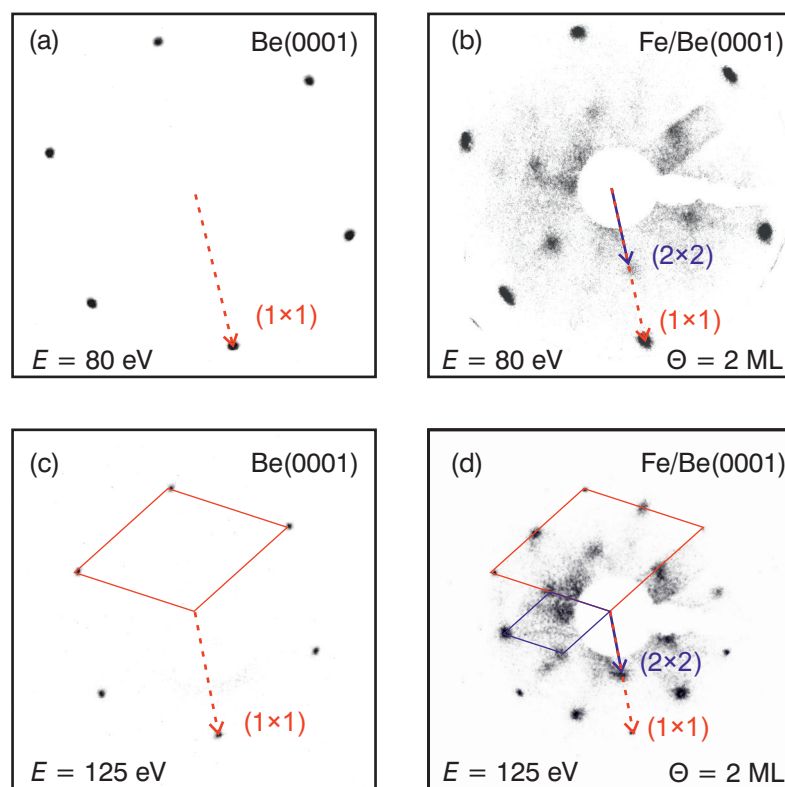


Figure 7.19: LEED patterns acquired with $E = 80$ eV of (a) clean Be(0001) and (b) 2 ML of Fe on Be(0001). Six spots corresponding to the (1×1) reflection peaks of the Be(0001) lattice are visible. After Fe deposition, additional spots corresponding to a (2×2) superstructure appear. (c), (d) LEED patterns of the same samples but acquired with $E = 125$ eV. On Fe/Be(0001) the second-order spots of the (2×2) structure become visible at this energy. The reciprocal unit cells of the (1×1) and (2×2) structures are indicated in red and blue, respectively. The contrast in the images is artificially increased for better visibility of the smeared out (2×2) spots.

surface, additional faint spots appear at half the distance from the center of the screen, corresponding to the (2×2) superstructure seen in STM. LEED patterns of the same samples acquired with $E = 125$ eV are depicted in Figure 7.19 (c) and (d). At this energy, the diffraction pattern on the screen appears smaller and second-order spots of the superstructure are visible. The (2×2) diffraction spots appear very faint in the experiment and are smeared out over a wider area on the screen compared to the (1×1) structure. This can be interpreted as a consequence of the only locally ordered superstructure. Because of the high degree of mosaicity in the film, atomic distances are less well-defined, compared to the long-range ordered substrate and the diffraction spots smear

out accordingly. Nevertheless, the orientation of the superstructure is well defined with reciprocal lattice vectors parallel to the reciprocal lattice vectors of Be(0001).

Saturation of ordered film growth

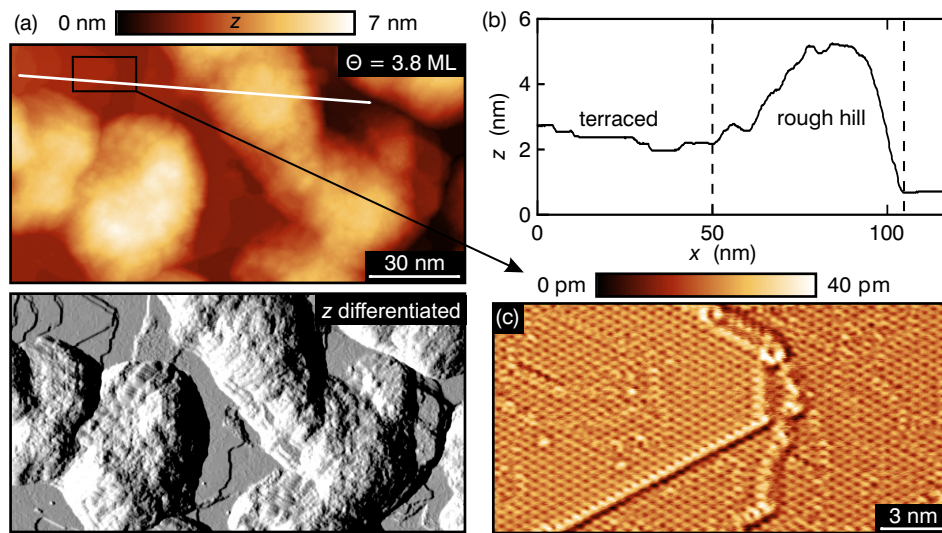


Figure 7.20: (a) Constant-current STM image (top) and its numerical derivative (bottom) of 3.8 ML Fe deposited onto Be(0001) at $T = 300\text{ °C}$ at a rate of 0.27 ML/min. Flat terraces coexist on the surface together with rough hills, several nanometers in height ($I = 100\text{ pA}$, $U = 600\text{ mV}$, $T = 40\text{ K}$, Cr tip). (b) Height profile across terraces and hills along the white line in (a), showing the different magnitudes in z -corrugation. (c) High resolution STM image of a terraced area in (a) ($I = 2\text{ nA}$, $U = 175\text{ mV}$, $T = 40\text{ K}$, Cr tip). Fourier filtering with a maximum cutoff periodicity of 1 nm was applied to the image to highlight atomic-scale corrugations on multiple terraces. The flat terraces in between hills exhibit a well ordered (2×2) surface structure with respect to the Be(0001) lattice.

The Fe coverage was further increased to investigate the range in which this growth mode persists. This experiment was performed together with Jan-Hendrik Schmidt [66]. An STM image of a sample with $\Theta = 3.8\text{ ML}$ can be seen in Figure 7.20 (a). Because of the protruding structures of several nanometers on the surface, the differentiated image is additionally supplied. The line profile in Figure 7.20 (b) shows the coexistence of a flat terraced film, as observed at lower coverages, and steep, three-dimensional upheavals.

A high-resolution STM image of the terraces is depicted in Figure 7.20 (c). The image is Fourier filtered to highlight atomic-scale structures on multiple terraces. The terraces exhibit again a (2×2) structure of improved order compared

to samples with lower Fe coverages (cf. Figure 7.17). From the coexistence of these well-ordered areas with three-dimensional growth occurring at this Fe coverage, it can be inferred that there is a maximum local thickness for films in the (2×2) structure. Excess Fe deposited onto the surface gathers in three-dimensional structures.

Volume analysis of Fe/Be(0001)

We have seen that at an effective Fe coverage of $\Theta = 0.5$ ML, films with a hexagonal atomic order start to form on Be(0001) that spread over an increasing portion of the surface with increasing coverage and assume a (2×2) superstructure on the Be(0001) substrate. For coverages $\Theta \geq 3.8$ ML, these ordered areas are gradually superseded by disordered 3D structures. Still, the origin of the ordered superstructure remains unclear. There are several possible explanations for the observed (2×2) structure. One would be a bcc-like Fe growth with a (111) termination. Another explanation would be a pseudomorphically grown Fe film under compressive stress with a (2×2) surface reconstruction. This would lead to an observed surface coverage smaller than the nominal coverage Θ as the deposited material would need to form a pseudomorphic film plus a relaxed structure on top. This scenario is in contradiction to the observation of a larger surface area of Be(0001) being covered than would be expected for a pseudomorphic film of coverage Θ . This is evident in the instance of 1 ML of Fe in Figure 7.13 (a), covering the Be(0001) surface nearly completely and additionally exhibiting multilayer islands.

In order to quantify the Be(0001) surface area covered per deposited Fe atom, an analysis of the volume of Fe/Be(0001) islands was carried out. Figure 7.21 (a) displays a sample of $\Theta = 1$ ML Fe deposited on Be(0001) at $T = 300$ °C. The sample preparation is identical to the surface area depicted in Figure 7.13 (a). Here, an exceptionally large surface area of $300 \text{ nm} \times 300 \text{ nm}$ without steps in the basal layer was chosen to analyze the volume of the grown islands. The lack of step edges circumvents the ambiguous assignment of islands grown at step edges to thicknesses of one atomic layer more or less on the upper or lower terrace. Inside the blue circle in Figure 7.21 (a), there is an island visible with its flat surface destroyed by a preceding contact with the tip. This island was excluded from the analysis due to its uncertain original thickness.

The islands exhibit stepped surfaces with step heights on the order of distances between atomic lattice planes. Areas exhibiting corrugations of ≥ 1 , ≥ 2 , ..., ≥ 5 lattice planes are marked in Figure 7.21 (b)-(f). The projected surface areas of the marked features were analyzed and divided by the total area of the image. The result is compiled in Table 7.3.

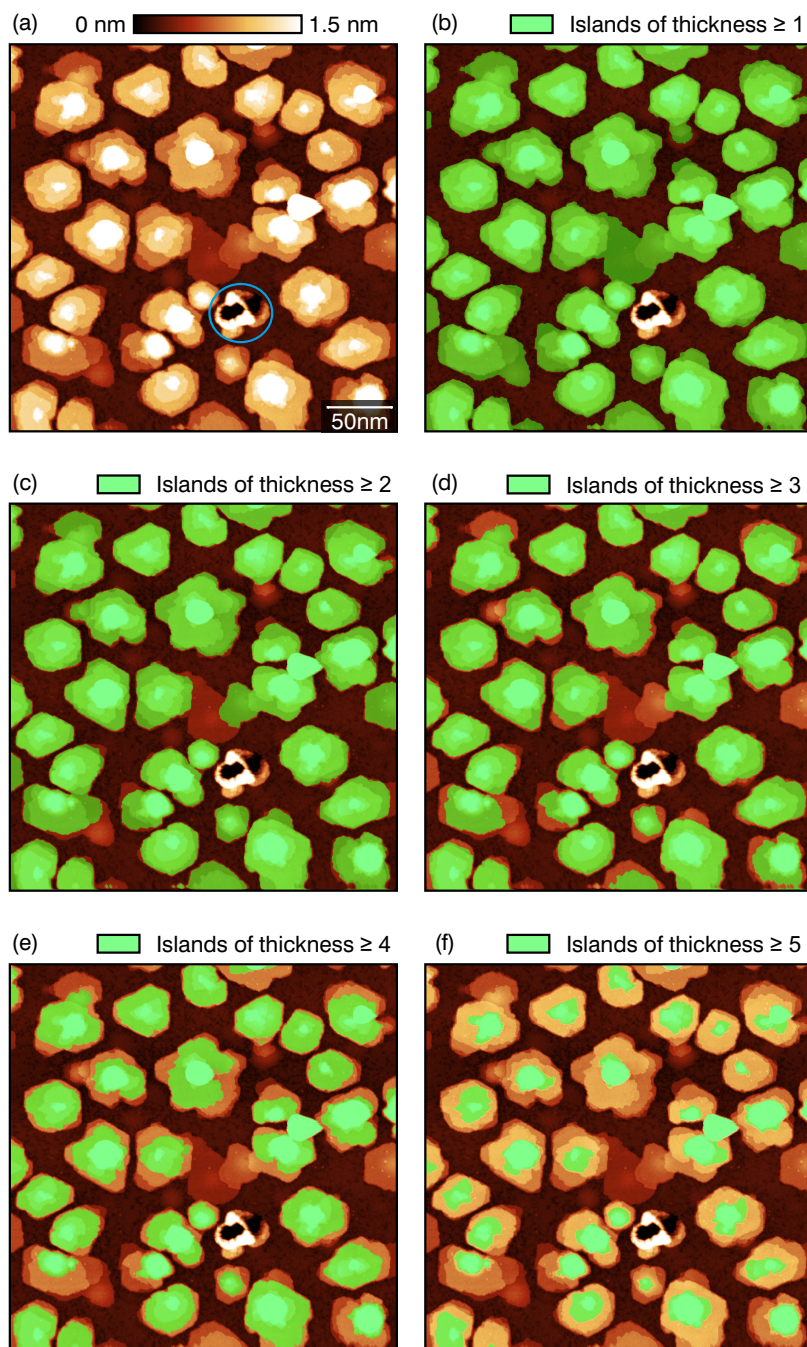


Figure 7.21: Analysis of the volume of islands for a nominal coverage of $\Theta = 1$ ML of Fe grown at $T = 300$ °C. (a) $300 \text{ nm} \times 300 \text{ nm}$ constant-current STM image of multilayer islands grown on Be(0001). Parameters: $U = -200 \text{ mV}$, $I = 200 \text{ pA}$, $T = 40 \text{ K}$, Cr tip. The projected surface areas of islands with corrugations corresponding to thicknesses of 1-5 atomic layers are marked in green in (b)-(f). A defect encircled in blue in (a) was excluded from the analysis.

Local island thickness (atomic layers)	Covered surface area (unity)
≥ 1	0.59
≥ 2	0.52
≥ 3	0.44
≥ 4	0.33
≥ 5	0.14
Sum	2.02

Table 7.3: List of relative covered surface areas by islands in Figure 7.21 in dependence of local island thickness. The combined island volume amounts to the equivalent of at least 2.02 atomic layers.

While 59 % of the surface area is covered by islands of at least one atomic layer in thickness, the areas covered by five or more layers make up only 14 percent of the total area. Above five steps, the surface of the islands do not retain a flat finish and the excess volume is neglected, so that the analysis poses a lower limit for the real achieved coverage of the substrate. In total, the stepped islands grown above the basal layer contain enough material to cover the analyzed surface area at least 2.02 times. Including the area of the defect and assuming it to originally have been five layers thick would enhance the result to only 2.07-fold coverage, a negligible difference considering the necessarily imprecise nature of this analysis.

Counting the basal layer as additionally fully covering the Be(0001) substrate, it can be concluded that deposition of Fe at $T = 300\text{ }^\circ\text{C}$ leads to structures covering around 3 times the surface area Θ expected for pseudomorphic growth.

Intermixing of Fe and Be forming an alloy with a surface unit cell of $2a_{\text{Be}}$ appears as a plausible explanation for this observation, especially in view of the low surface free energy of Be(0001) [158]. In this interpretation, Fe is diluted in an alloyed phase that covers the surface of pure Be(0001). Depending on the stoichiometry and interatomic spacings inside the alloyed phase, the covered surface area will be larger compared to pseudomorphic growth. In the following section, an AES study comparing the chemical surface composition of Fe grown in islands at room temperature (RT) on the one hand, and of ordered films grown at $T = 300\text{ }^\circ\text{C}$ on the other hand, is presented.

7.4 Coverage-dependent Auger electron spectroscopy

In the previous section, we saw that the substrate temperature during Fe deposition has critical influence on the observed growth mode. Deposition of small amounts of Fe at 300 °C leads to larger islands compared to room temperature deposition. These larger islands were also observed to develop a $p(2 \times 2)$ superstructure and to coalesce into extended films for higher coverages. These films disintegrate during prolonged annealing at 300 °C, uncovering pure Be(0001) again on the surface. Whether the Fe is concentrated in certain areas on the surface or diffuses into the Be matrix during the disintegration remains unclear. Given the low surface free energy of Be(0001), the intermixing of the deposited Fe with the substrate is plausible. Accordingly, the observed (2×2) structures may already originate from an intermixed state. In order to elucidate this hypothesis, an AES study was carried out on samples grown at room temperature and $T = 300$ °C, respectively. AES provides a chemical sensitivity of a few atomic layers at the sample surface with decreasing sensitivity for layers lying deeper below the surface. In case of intermixing at elevated temperatures of Fe and Be, the decreased Fe content compared to room temperature growth should be reflected in Auger spectra. The AES study presented here was part of the master thesis of Karoline Oetker [153] that I supervised in the context of this work. The experiments were carried out jointly.

For reference of the evaporant material, an Auger spectrum acquired on 20 ML Fe/W(110) is presented in Figure 7.22. Four major peaks characteristic for Fe are observed: The measured values of the LMM peaks at 48 eV, 598 eV, 651 eV,

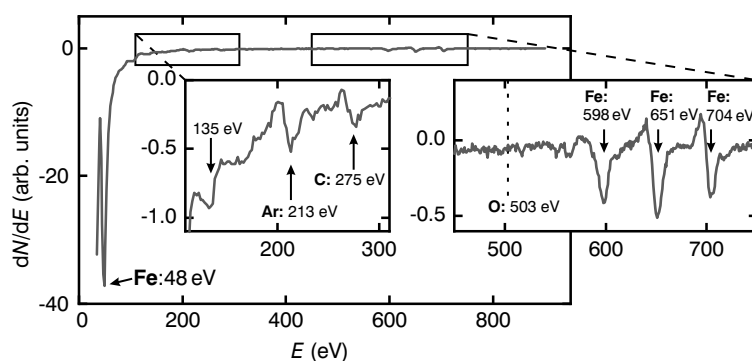


Figure 7.22: Auger spectrum of 20 ML Fe on W(110). Parameters: $E_p = 3$ keV, $I_p = 30$ μ A, $U_{\text{mod}} = 5$ mV. Peak positions are indicated by arrows and related to elements where possible. The insets depict zooms to peaks of low intensity. Four peaks characteristic for Fe are labeled.

and 704 eV are in good agreement with the literature values of 47 eV, 598 eV, 651 eV, and 703 eV [60].

Additionally, three minor peaks are observed. The peaks at 213 eV and 275 eV correspond to Ar and C contaminations found in reference spectra of Fe samples at 212 eV and 272 eV, respectively [60]. The origin of the peak at 135 eV is unclear with no corresponding peak of common surface contaminants at that energy. Noteworthy is the absence of a peak around 503 eV that would indicate an oxygen contamination. Consequently, AES of the Fe film shows no major contaminations of foreign metals. The residual surface contaminants found also exist in reference spectra in literature [60].

After verification of the evaporator material as Fe, an AES study of Fe/Be(0001) was conducted. Figure 7.23 (a) depicts Auger spectra of Fe/Be(0001) samples of $\Theta = 1.0$ ML grown at room temperature and at 300 °C, respectively. Exemplary STM images accompany the Auger spectra to show the surface morphology in the two growth modes. Auger spectra for $\Theta = 2$ ML together with STM images of samples in this coverage regime are depicted in Figure 7.23 (b). The spectra obtained on samples in both growth modes and in both investigated coverages show the peak at 48 eV characteristic for Fe, as well as the characteristic Be peak at 105 eV.

The volumetric structure of the investigated Fe/Be system is unknown to us. For the low coverages under investigation that exhibit smoothly grown films, the sample can not be expected to have a homogeneous chemical composition within the sensitivity range of the Auger spectroscopy. For this reason, the quantitative comparison of a single spectrum to literature spectra through tabulated sensitivity factors for different elements is not feasible. Direct comparison of peak heights in a Fe/Be(0001) sample to peak heights in reference spectra of pristine Be(0001) and Fe samples, respectively, may be misleading, too. A reason for this is that the surface roughness of the inspected samples varies for different temperatures during Fe deposition, and the surface roughness has influence on the Auger yield [60]. Auger analysis was used instead to qualitatively examine the changes in Fe concentration in surface-near layers on Be(0001) induced by variations of the growth conditions. This is done by comparison of the ratios between characteristic Fe and Be peaks for samples prepared at different substrate temperatures during Fe deposition with otherwise identical parameters. As a measure for the Fe content in surface-near layers, the ratio of the peak intensities for Fe and Be

$$\chi = \frac{I_{\text{Fe}}}{I_{\text{Be}}} = \frac{dN/dE(48 \text{ eV})}{dN/dE(105 \text{ eV})} \quad (7.3)$$

is introduced. The ratio χ compares intensities measured on a single sample

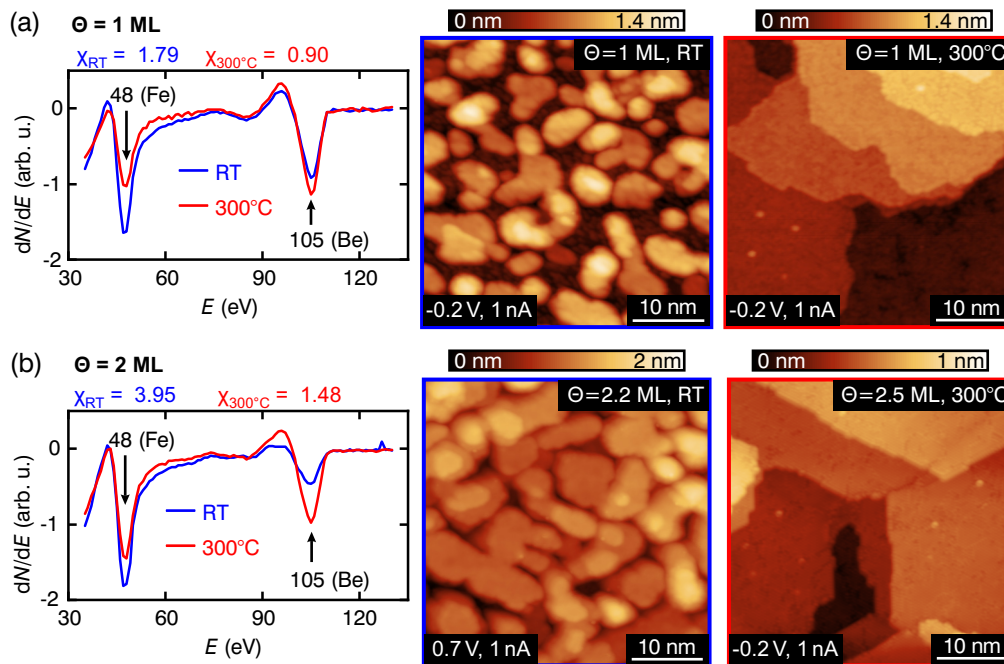


Figure 7.23: Comparison of Auger spectra for growth at room temperature and at $T = 300^\circ\text{C}$, respectively. (a), (b) Auger spectra for $\Theta = 1$ ML and $\Theta = 2$ ML of Fe on Be(0001) grown at a rate of 0.12 ML/min. STM images with similar Fe coverages grown at room temperature and at 300°C , respectively, are exemplarily shown. Deposition at elevated temperatures leads to an increased intensity of the Be-peak at 105 eV and a simultaneous decrease of the Fe-peak at 48 eV. Parameters: $E_p = 3$ keV, $I_p = 30$ μA , and $U_{\text{mod}} = 2$ mV.

and in a single experiment and should be robust with respect to changing total intensities due to surface roughness.

In Figure 7.23 (a) and (b) the Auger spectra in the two growth modes deviate around 48 eV and 105 eV. The intensity of the peaks at these energies, corresponding to Fe and Be, show a dependency on the sample temperature during Fe deposition. For room temperature deposition, the Fe peak is most prominent. Deposition at 300°C leads to an increase of the Be peak in the Auger spectrum at the expense of the Fe peak.

At $\Theta = 1$ ML, islands and clusters form at room temperature, while at 300°C the Be(0001) surface is covered by a disordered and uneven film. It is imaginable, that the substrate contributes substantially to the AES signal in both cases because of the thin coverage and especially because of the bare substrate in interstitial spaces of islands for room temperature growth. This contribution is found to be stronger for an elevated deposition temperature with $\chi_{300^\circ\text{C}} = 0.90$ versus $\chi_{\text{RT}} = 1.79$ for room temperature. Even for this low coverage, the deposition

temperature has a measurable influence on the relative peak heights, despite the large substrate contribution to the AES signal.

For $\Theta = 2$ ML, values of $\chi_{\text{RT}} = 3.95$ for room temperature deposition and $\chi_{300^\circ\text{C}} = 1.48$ for deposition at $T = 300^\circ\text{C}$ can be extracted. As a consequence, a higher concentration of Be within the topmost surface layers of the sample grown at elevated temperatures is expected.

In order to interpret this result, the surface morphologies for the two growth modes in this coverage regime are compiled in more detail in Figure 7.24. At room temperature (Figure 7.24 (a)), the growth still occurs in the Volmer-Weber mode. But compared to $\Theta = 1$ ML, coalescence of islands has started with deep trenches remaining between many islands. Figure 7.24 (b) shows the corrugation in z along the white line across multiple islands. The height of the islands amounts to approximately 1 nm. The small distance between neighboring islands may be too small for the tip to reach the lowest point in between, possibly influencing the line profile in the interstitial spaces.

Figure 7.24 (c) shows details of the films grown at 300°C . The height profile in Figure 7.24 (d) shows the monatomic step height between neighboring terraces and the reduced roughness compared to room temperature grown samples. A magnified part of the image is shown numerically differentiated in Figure 7.24 (e). The $p(2 \times 2)$ -ordered superstructure is observed on all the terraces, including the lowest lying one.

Despite the fully covered Be(0001) surface in this regime for growth at 300°C , the Auger spectrum showed a higher Be content in surface-near layers compared to room temperature growth. This is contradictory to pseudomorphic Fe growth with a (2×2) -reconstructed surface for the ordered film. In such a case, a closed Fe film would be expected to yield a higher relative Auger intensity compared to growth in separated islands.

The observations corroborate the hypothesis that the observed $p(2 \times 2)$ structure is a manifestation of intermixing at elevated deposition temperatures. The behavior can be explained by an argument about the dynamics of the growth process. Bare Be(0001) is energetically favorable over an intermixed surface or an Fe covered substrate. During Fe deposition, Fe atoms land on the Be surface and an energy barrier hinders the fast diffusion into the substrate. At RT, the Fe stays on top or intermixes slower than islands form on top. At $T = 300^\circ\text{C}$, a slow diffusion process takes place. A metastable intermixed phase forms until a thickness of saturation is reached. The incorporation of deposited Fe will become less likely as the intermixed film grows, because the mean distance to the Be reservoir in the substrate increases with film thickness. Consequently, the excess Fe grows in 3D islands as observed in Figure 7.20. In the following section, high resolution STM images of the ordered $p(2 \times 2)$ -structured sur-

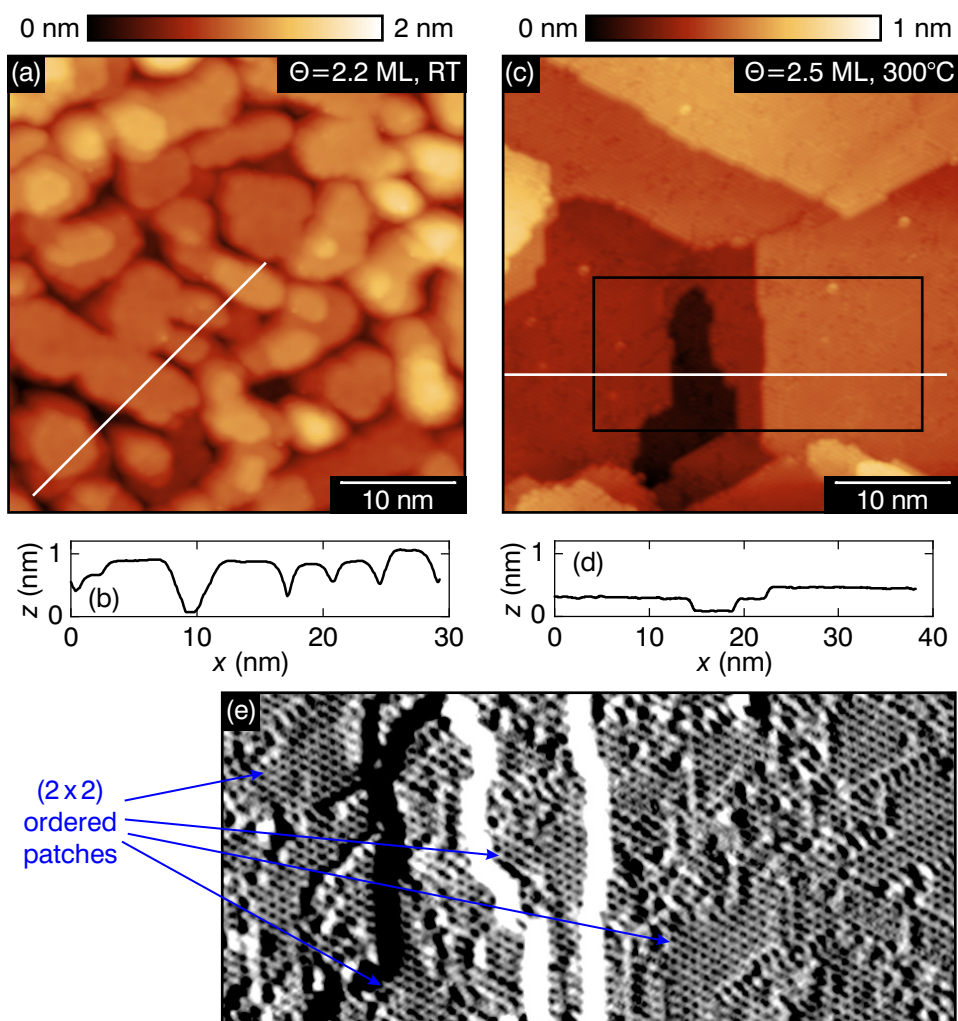


Figure 7.24: (a) Constant-current STM map of $\Theta = 2.2$ ML of Fe on Be(0001) deposited at room temperature. Growth of islands of various thicknesses is observed. In contrast to growth at 300 °C, coalescence of the islands is not concluded at this coverage. Parameters: $I = 1$ nA, $U = 700$ mV, $T = 60$ K, Cr tip. (b) Height profile along the white line in (a). (c) Constant-current STM map of $\Theta = 2.5$ ML of Fe on Be(0001) deposited at 300 °C. A continuous film has formed. Parameters: $I = 1$ nA, $U = -200$ mV, $T = 40$ K, Cr tip. (d) Height profile along the white line in (c). (e) Numerical differentiation of the rectangular area in (c), revealing patched, hexagonally ordered structures on consecutive terraces.

faces will be compared to known Fe-Be intermetallic compounds to identify candidates that could explain the observed growth.

7.5 Microscopic investigation of (2×2) -ordered Fe-Be films

So far, AES and STM showed indications of an intermixed phase of Fe and Be that exhibits a hexagonal surface order with a lattice constant of $a = 2a_{\text{Be}} = 456$ pm. STM data with high spatial resolution can be exploited to draw conclusions about possible atomic configurations inside the observed (2×2) surface unit cell and their comparison to ordered Fe-Be alloys.

7.5.1 Fe growth on Be(0001) compared to Fe-Be alloys

The Fe/Be(0001) surface was investigated regarding the internal structure and relative orientation of (2×2) ordered areas. STM images of the same surface area acquired with $U = -200$ mV and -700 mV are depicted in Figure 7.25 (a) and (b), respectively. They were obtained on a Be(0001) surface after deposition of $\Theta = 1.5$ ML of Fe. While the structure appears as hexagonally ordered elevations in Figure 7.25 (a), it appears as a honeycomb structure in Figure 7.25 (b). In between these two scans, the tip spontaneously changed on the microscopic scale. Therefore, the drastic change of appearance can not be attributed to the change in bias voltage alone.

In the zoomed image in Figure 7.25 (c), the apparent elevations seen at $U = -200$ mV are marked by green dots. In Figure 7.25 (d), the green lattice spots are overlaid on the honeycomb lattice seen at $U = -700$ mV. Every second vertex of the honeycomb lattice corresponds to an elevation at $U = -200$ mV (green). The other neighboring vertices are labeled in blue. A line defect in the lattice separating two crystalline domains is marked. In the bottom domain in Figure 7.25 (c), point defects are marked by circles. These sites may be vacancy sites. For comparison, in Figure 7.25 (d), these sites can be identified as missing vertices in the honeycomb lattice. This motivates the interpretation of these green sites as places where atoms reside. Accordingly, the surface structure can be interpreted as a hexagonal lattice with a two-atom basis (green and blue). The different appearance of the lattice in dependence of tip configuration and bias voltage shows that the two atoms per basis are not equivalent. They have to differ either in atomic species or occupy distinct lattice sites.

On closer inspection, one finds that the line defect separates two rotational domains of this lattice rotated by 180° . The unit cell of the superstructure with its two-atom basis — marked by a red diamond in the image — is threefold symmetric. It is found to align with the substrate lattice that is sixfold symmetric. Accordingly, there are two different rotational domains that can form

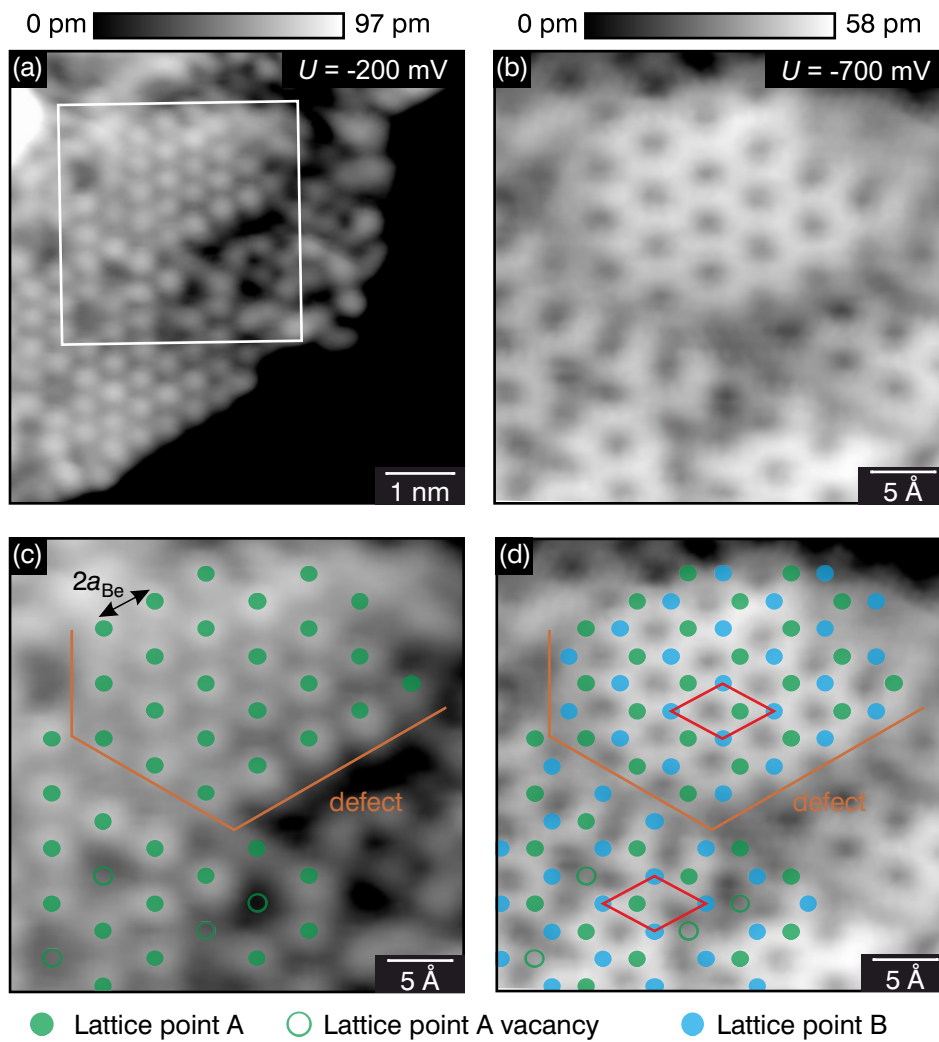


Figure 7.25: (a) Constant-current STM map of $\Theta = 1.5$ ML of Fe on Be(0001) imaged with $U = -200$ mV. A lattice of apparent protrusions is visible. (b) shows the highlighted area in (a) imaged with $U = -700$ mV after a spontaneous change of the tip. The appearance of the lattice changed to a honeycomb structure. (c) Magnification of the highlighted area in (a) with lattice points and vacancies marked in green. A line defect separating two ordered areas is visible. (d) Honeycomb lattice model overlaid on the image in (b). Green lattice spots are identified as vertices of the honeycomb lattice. Unit cells with a two-atomic basis are indicated by red diamonds. The line defect separates two domains that are rotated by 180° . Parameters: $U = -200$ mV (a,c), $U = -700$ mV (b,d), $I = 2$ nA, $T = 60$ K, Cr tip.

during growth and the random distribution of grains growing in one or the other orientation will induce dislocations where both domains meet.

The Fe-Be intermetallic system

Fe and Be are miscible substances in the sense that the total free energy is reduced for an intermixed phase compared to a separated phase. In solid Be for example, substitution of a Be atom by an Fe atom leads to a gain of 0.09 eV [164]. Accordingly, there are several stable bulk alloys of Fe and Be with a negative free energy of formation. Of those alloys, DFT calculations show that $\text{Fe}_2\text{Be}_{17}$ and FeBe_2 are the most stable ones for $T \leq 1000$ K [165]. Consequently, intermixing between the Fe adlayer and the Be(0001) substrate may be expected for sufficient substrate temperatures that allow interdiffusion of deposited material into the substrate [166].

The Fe-Be intermetallic system was structurally investigated in bulk by means of x-ray diffraction [24, 167]. Ohtani *et al.* derived the phase diagram by *ab-initio* calculation of the Gibbs free energy [168]. At $T \approx 300$ °C, two stable phases exist: The Be-rich ϵ -phase with a stoichiometry of FeBe_{11} or FeBe_{12} for Fe concentrations up to ca. 28 % [168, 169]; and for higher Fe concentrations up to 50 % the ζ -phase with a composition of FeBe_2 [165, 168, 169].

As the observed ordered films in this work exhibit a (2×2) superstructure of the closely spaced Be(0001) surface, the surface unit cell is expected to host a maximum of four atoms. Also, this structure was seen to saturate for Fe coverages ≥ 3.8 ML, suggesting it to be a phase of high Fe content. Because of these factors, the FeBe_2 phase, stable at higher Fe concentration is of particular interest.

Atomic structure of FeBe_2

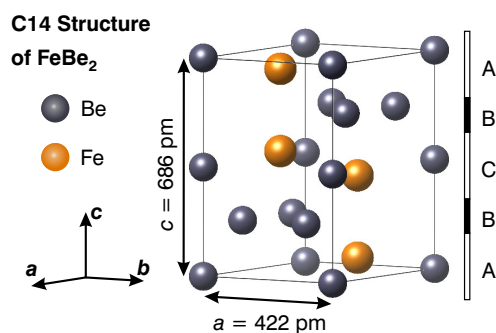


Figure 7.26: Conventional unit cell of FeBe_2 in the C14 Laves structure with lattice parameters of $a = 422$ pm and $c = 686$ pm [165, 169].

FeBe_2 crystallizes in the C14 Laves structure, which is a hexagonal structure with optimal packing for spheres of two different sizes. A differently stacked

configuration of FeBe_2 in the C15 Laves structure with a cubic unit cell was found to be energetically unfavorable for $T < 1000 \text{ K}$ [165]. The conventional unit cell of the C14 structure is shown in Figure 7.26. It consists of a sequence of mixed (C) and Be-heavy (B) layers stacked along the c -axis. The surface structure of FeBe_2 was not subject of investigations so far. Consequently, bulk-truncated surfaces terminated by layer B or C will be discussed. Additionally, the structure may be terminated in an only partially completed layer (A). These slices of the structure are shown in Figure 7.27. They represent imaginable surface terminations of the FeBe_2 Laves structure. The surface unit cells of such terminated surfaces are shown in a top view (parallel to the c -axis), and from the side (perpendicular to the c -axis).

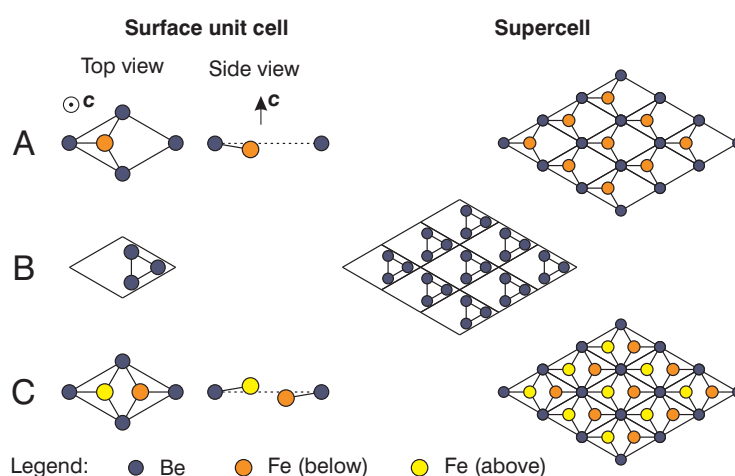


Figure 7.27: Representation of the surface terminations of FeBe_2 based on the layers A, B and C assigned in Figure 7.26. Fe atoms that are offset above (below) the plane of Be atoms in A and C are marked in yellow (orange). Supercells of nine surface unit cells are shown for comparison to the experimental data.

In the case "B" consisting exclusively of Be atoms, these atoms form a hexagonal lattice in a single plane with three atoms per unit cell. In case "A", the unit cell has a two-atomic basis with Fe atoms situated below the plane formed by Be atoms. In this case, both atomic species form hexagonal lattices and the supercell illustrates that this termination can be understood as a buckled honeycomb lattice with Fe atoms on top of hollow sites in "B". In case "C", the hollows inside this honeycomb lattice are filled by Fe atoms lying in a plane offset along the c -axis relative to the Be plane.

STM of Fe/Be(0001) compared to bulk-truncated FeBe₂

On Fe/Be(0001) surfaces, a hexagonal unit cell with two-atomic basis was found in STM (cf. Figure 7.25). Comparison to the possible surface terminations of FeBe₂ in Figure 7.27 shows that the terminations "A" and "C" could explain the observed bias-dependent appearance as either honeycomb-like or hexagonal. The different appearances would result from different atomic species, or alternatively of Fe atoms in differing lattice sites, with contributions to the tunneling current that vary for different configurations of the tip apex or vary with the applied bias voltage. The surface termination "B" has a unit cell of the same size, but this termination layer is sixfold symmetric and does not motivate an appearance as observed in STM in Figure 7.25. Also with Fe atoms inside the hollows in "B", the structure remains sixfold symmetric and can be excluded.

Figure 7.28 displays pictograms of supercells of layers A, B and C viewed from the top. Additionally, it is shown how layers A and C are stacked on layer B. Termination A can be superimposed on the experimental data by identification of the blue lattice sites in Figure 7.25 as recessed Fe atoms, and the green lattice spots as Be atoms in the FeBe₂ termination A. Consequently, the experimentally observed lattice defect presents itself as a domain boundary between two rotational domains of the FeBe₂ lattice.

The assignment of this specific configuration is ambiguous. The assignments of Be and Fe atoms could be reversed and still possibly yield the observed STM constant-current contour. Likewise, the FeBe₂ termination C provides another explanation for the observed structure. In this case, the assignment of protruding (yellow) Fe atoms to green lattice sites seems natural, as these sites appear as protrusions at $U = -200$ mV. Nevertheless, the STM is sensitive to the sample's electronic DOS and not its topography, so that additional investigations, as for example theoretical calculations of the electronic surface DOS, would be necessary for an unambiguous assignment.

The basal lattice constant of FeBe₂ in the C14 structure is $a = 422$ pm in bulk [165, 169]. The observed superstructure, however, has a lattice constant of $2a_{\text{Be}} = 456$ pm, corresponding to a mismatch of 8%. Accordingly, overlayers grown this way experience a tensile stress in the basal planes with more ample interatomic spacing than occurring in bulk material. The observed small scale of ordered surface areas may be a cause of this mismatch. Atoms occasionally occupying sites with smaller interatomic spacing during growth may be the cause of discontinuities in the surface structure. This interpretation of the data in Figure 7.28 was developed jointly with Karoline Oetker [153].

An open question is how the assumed alloy is oriented with respect to the underlying substrate. Evidently, the orientation of the substrate's high-symmetry

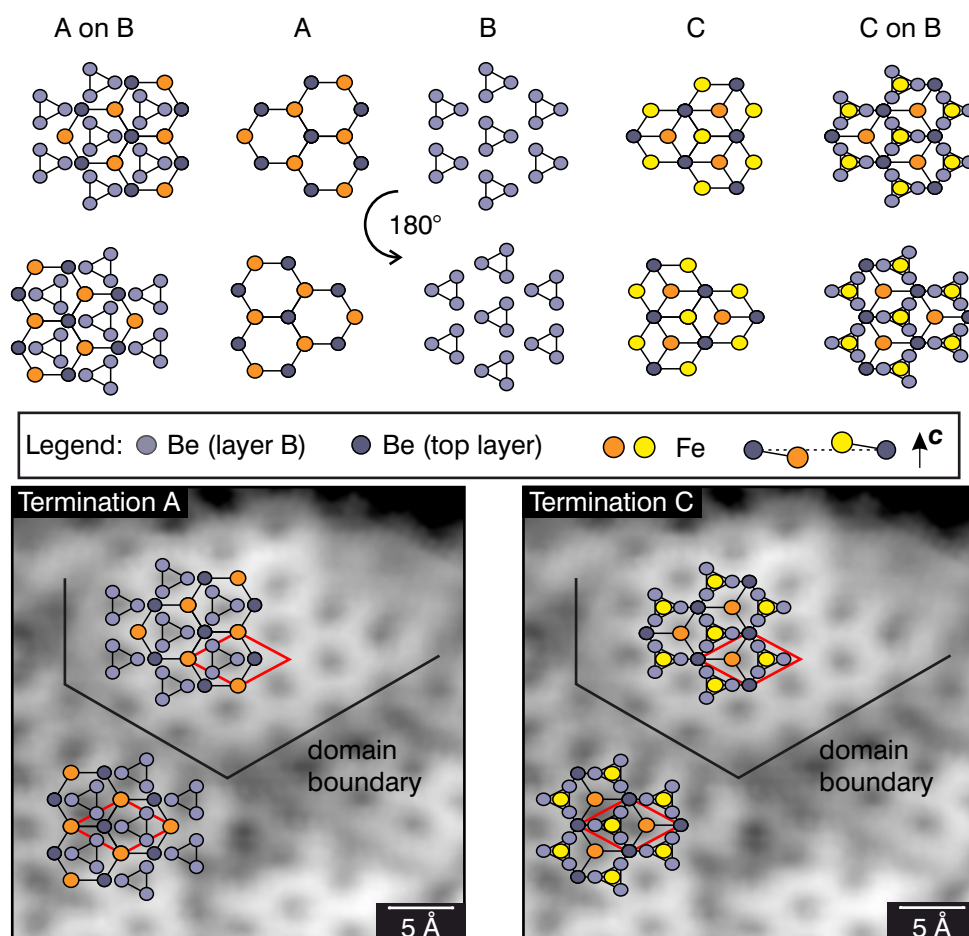


Figure 7.28: Models of different terminations of FeBe₂ overlaid on the STM-image from Figure 7.25 (b). Top: Pictograms of FeBe₂ layers A, B and C, as well as A and C superimposed on B. Two variations rotated by 180° are shown. Bottom: FeBe₂ terminations A and C overlaid on the experimental data. Layer B underneath is shown to demonstrate the stacking sequence. Comparison to Figure 7.25 allows the identification of two rotational domains separated by a domain boundary. Parameters: $U = -200$ mV, $I = 2$ nA, $T = 60$ K, Cr tip.

directions is preserved in the superstructure and the substrate's basal lattice constant is reflected in it as well. This suggests that Fe atoms may replace Be atoms in the substrate during deposition and occupy their previous lattice site. If this is the case, then the structural domains imaged on the sample surface should be offset relative to one another based on the boundary conditions set by a common substrate lattice. In order to investigate the relative shift of ordered domains, we turn to a relatively high Fe coverage of $\Theta = 3.8$ ML, yielding well-ordered structures across multiple terraces as known from Figure 7.20.

An STM image of the stepped surface is depicted in Figure 7.29 (a). First, we will investigate the domains within the largest terrace. A high-resolution STM image acquired with $U = -200$ mV, yielding good contrast of the (2×2) structure in this area, is shown in Figure 7.29 (b). Four domains are representatively chosen and marked with letters A-D. Solid, equally spaced, vertical lines of distance $d \approx \sqrt{3}a_{\text{Be}}$ between each other track the lattice spots on domain A. The lattice of domain C aligns with the one of domain A in this direction. Broken lines are horizontally offset from solid lines by $\frac{d}{2}$ and align with domains B and D. Accordingly, domains B and D are horizontally offset from domains A and C by $\frac{\sqrt{3}}{2}a_{\text{Be}}$. In Figure 7.29 (c) and (d), the process is repeated along the other high-symmetry directions with solid lines again centered on domain A. Due to a distortion caused by thermal drift between tip and sample, the high-symmetry directions in the image deviate from the ideal $\pm 120^\circ$ with respect to the vertical axis by 2° and 2.5° , respectively. In Figure 7.29 (c), domain B aligns with A and in Figure 7.29 (d), it is domain D that aligns with A. We find that each of the other domains aligns with domain A along one of the high-symmetry directions.

An explanatory model is depicted in Figure 7.29 (e). Green spots represent the surface domains and black spots represent an imaginary underlying Be(0001) substrate. The shifts found between the domains correspond to offsets by a_{Be} in one of the three directions of high symmetry, leading to four possible configurations. This is a consequence of the unit cell in the surface structure being four times as large as the substrate unit cell.

For the relative orientation of domains on different terraces, we turn to the step downward from this terrace. The area of interest is depicted in an STM image in Figure 7.30 (a). Lateral drift effects were corrected here based on the lattice on the topmost terrace to yield hexagonal symmetry. This correction is necessary to ascertain that the lateral offsets between ordered domains, amounting to only a few Å, are not artificially displaced. The drift correction is justified, as the superstructure was found to have hexagonal symmetry by LEED (c.f. Figure 7.19) and by STM under exclusion of drift effects (c.f. Figure 7.18). A line profile across the three depicted terraces is shown in Figure 7.30 (b). The terraces are vertically offset by (1.8 ± 0.5) Å, corresponding to the step height of Be along the principal axis. A full additional layer of FeBe_2 would result in a vertical offset of $\frac{c}{2} = 3.4$ Å [165], maybe slightly reduced by the lateral stretching due to the lattice mismatch. This discrepancy motivates that a step edge of the Be(0001) substrate may be buried there instead of a stepped overgrown film.

A magnified image of the area around the step edge is depicted in Figure 7.30 (c). Low-frequency Fourier components were filtered out to reduce the

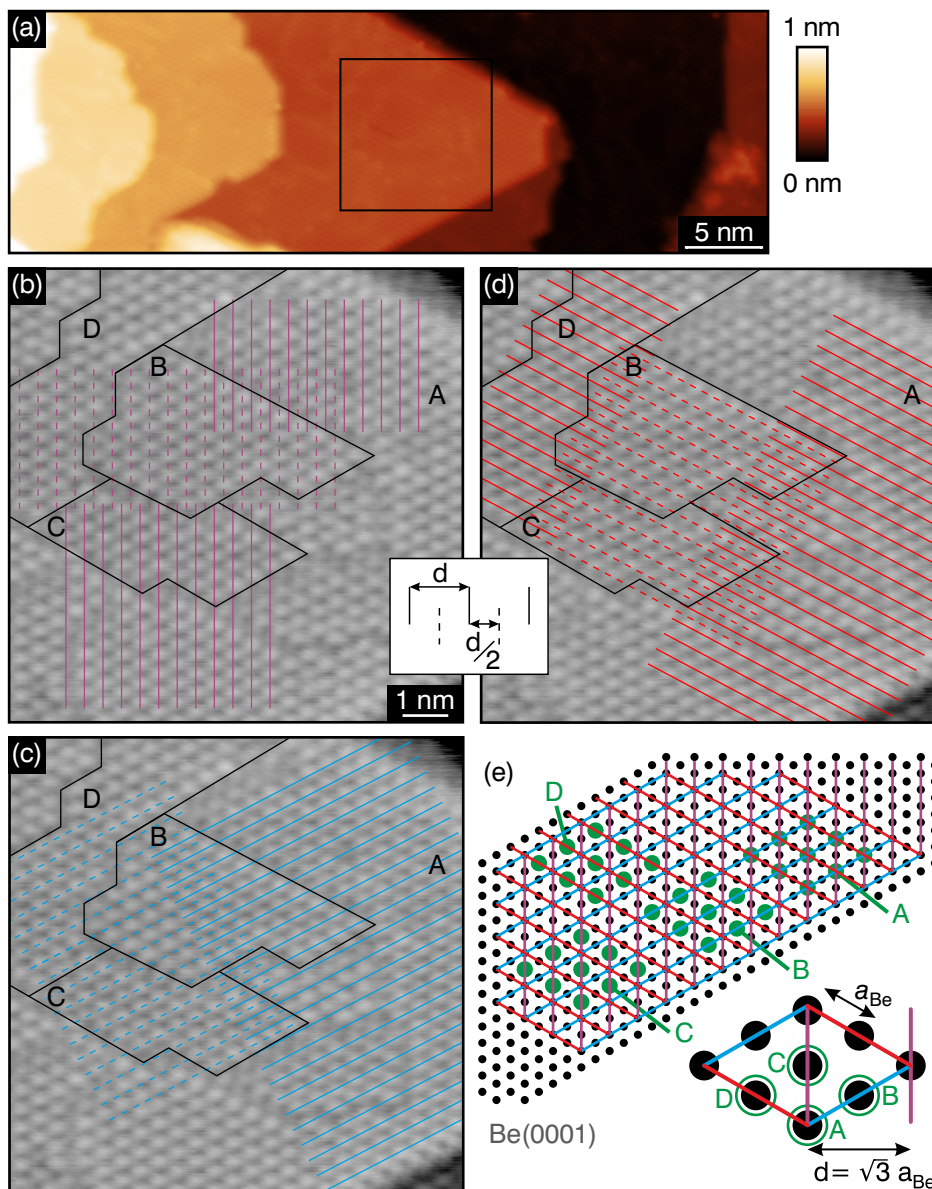


Figure 7.29: (a) Constant-current STM image of $\Theta = 3.8$ ML of Fe on Be(0001) deposited at 300°C . (b-d) Higher resolution STM image of the area marked on the largest terrace in (a). The data is filtered with a cut-off period of 800 pm to emphasize the superstructure. Structural domains are labeled A-D. Solid lines are aligned on bright spots (elevations in z) on domain A. Broken lines are positioned halfway in between solid lines. (e) Structural model showing the positions of the domains relative to each other and to a common Be(0001) substrate layer. Parameters: (a) $U = 175$ mV; (b-d) $U = -200$ mV, $I = 2$ nA, $T = 40$ K, Cr tip.

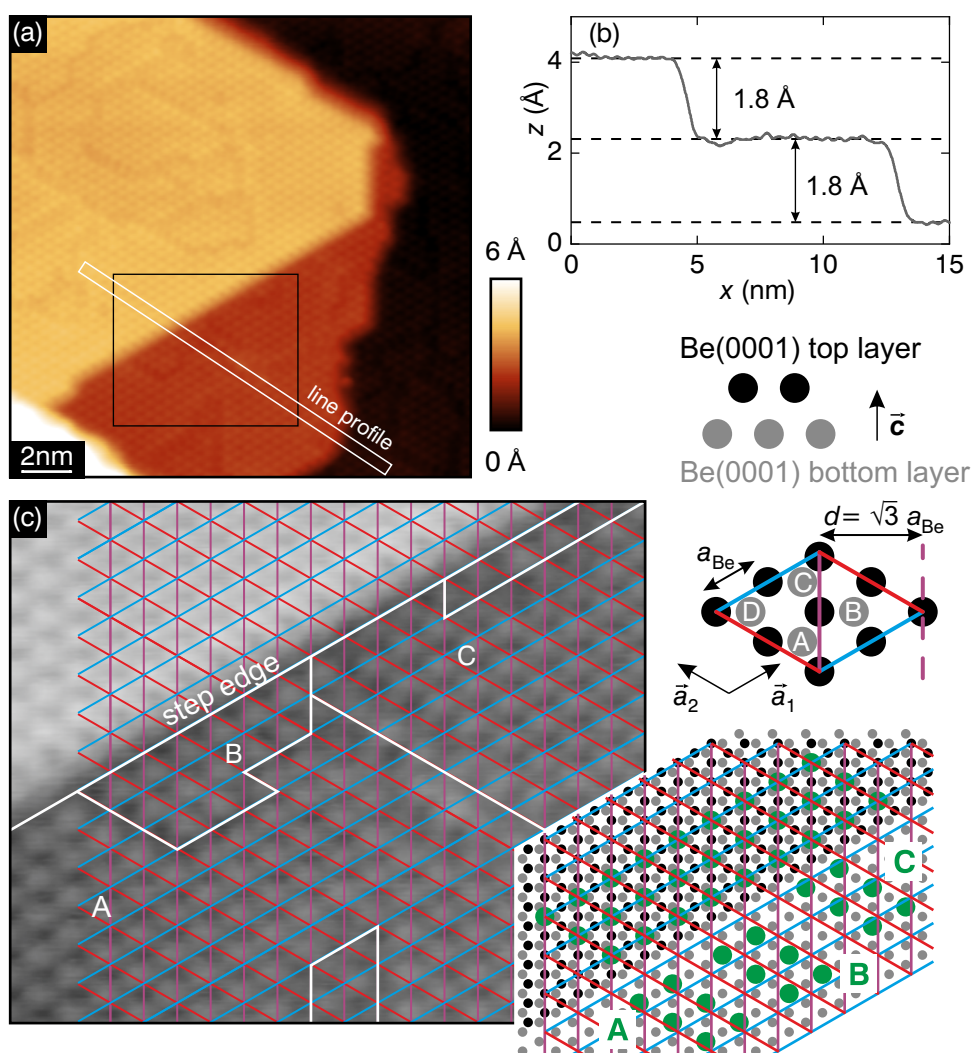


Figure 7.30: (a) Constant-current STM image of consecutive terraces exhibiting ordered domains. The data was corrected for lateral drift assuming a (2×2) superstructure on the upper terrace. (b) Line profile across the terraces in (a). (c) Magnified view of the area marked in (a). Fourier filtering with a maximum cutoff periodicity of 800 pm was applied to diminish the magnitude of the step relative to the lattice corrugation. Structural domains on the bottom terrace are labeled A-C. A hexagonal lattice is aligned with the structure on the upper terrace and extrapolated to the bottom terrace. A ball model of the domains with a buried Be(0001) step underneath is depicted on the side. Parameters: $U = -250$ mV, $I = 2$ nA, $T = 40$ K, Cr tip, $\Theta = 3.8$ ML, deposited at 300 °C.

magnitude of the step edge for better visibility of the lattice structures on both terraces. A hexagonal lattice is overlaid and aligned with the data measured on the upper terrace. Structural domains on the lower terrace are labeled A, B, and C. An atomic model of the situation is depicted on the right with substrate layers in gray and black, stacked on top of each other. Four sites with different shifts compared to the (2 × 2) unit cell can be identified in the lower substrate lattice (gray). They are shifted laterally with respect to the above layer (black) by A: $\left(\frac{1}{3}, \frac{2}{3}\right)$, B: $\left(\frac{4}{3}, \frac{2}{3}\right)$, C: $\left(\frac{4}{3}, \frac{5}{3}\right)$, and D: $\left(\frac{1}{3}, \frac{5}{3}\right)$ in a basis of the lattice vectors a_1 and a_2 of Be(0001). The extended ball model illustrates the arrangement of domains A-C on the bottom terrace with respect to the lattice on the upper terrace. It reproduces the shifts found in the STM image. Consequently, consecutive terraces in the film can not automatically be assumed to have different thickness. In this special case of a vertical offset of 1.8 Å between terraces, the same thickness on both sides of the step — offset by one atomic layer of Be — can be assumed. However, the step height between adjacent terraces was found to vary between 1.6 Å and 2.2 Å. This means that the growth of these supposedly alloyed films will generally occur in different local thicknesses or differently stacked layers. Also different local terminations of (2 × 2)-ordered films are possible within the model of bulk-truncated FeBe₂, as was shown in Figure 7.28, and may lead to varying measured step heights. Additionally, a changing stoichiometry with increasing Be content in deeper-lying layers can be imagined.

While the model of an alloyed FeBe₂ surface film is in accordance with the observed atomic surface structure, it also serves to explain the unexpectedly large surface coverage. Due to the stoichiometry and the lower atom density in FeBe₂ compared to Be, the model alloy with the same Fe content could cover up to four times the area of a pseudomorphically grown Fe film. Deviations from this theoretical value may result from the inaccessibility of volume buried below islands. If an alloying takes place, the alloy formation may as well advance from the sample surface downward with Fe atoms diffusing into the Be crystal. In the thin films grown on a substrate with lattice mismatch of 8 % compared to bulk FeBe₂, the volumetric structure of films may deviate from bulk material. Additionally, different surface terminations of FeBe₂ have different Fe content. The substrate area effectively covered per deposited Fe atom will thus depend on the preferred termination. Within these considerations, the model of an FeBe₂ surface film is in accordance with the observed enhancement of the measurable coverage of at least a factor of three.

7.5.2 STS measurements on (2×2) -ordered films

The atomic structure of (2×2) -ordered Fe/Be(0001) surfaces was discussed in the previous section as a manifestation of an Fe-Be alloy. Different chemical constituents in the surface should influence the electronic structure and could thus be reflected in tunneling spectra. An STS study was performed on the atomic (2×2) structure in order to assess spectroscopic signatures of specific lattice sites. The investigated area with a nominal coverage of $\Theta = 2.5$ ML is depicted in Figure 7.31 (a). The well-known layered structure of ordered terraces is reproduced. Higher resolution images of the investigated area are shown in Figure 7.31 (b) and (c). The hexagonal unit cell and the lattice constant of a_{Be} are indicated. The vertices of the hexagonal unit cell appear with different apparent height in agreement with the model of different atomic species in the surface of FeBe_2 . The corrugation in the structure measures $\Delta z \approx 20$ pm between dips and peaks as is evident in the line profile.

Challenges in this experiment arise from the necessity of a tip that is sharp enough to resolve the (2×2) structure including the distinct lattice sites within the structure, and is simultaneously stable over a wide range of applied bias values to yield comparable tunneling spectra. The bias range in the spectroscopy experiment was limited to $[-0.4 \text{ V}, 0.4 \text{ V}]$ because higher absolute bias values provoked frequent tip instabilities. The tip was stabilized in z above a certain position on the surface at $U = -0.4 \text{ V}$ and $I = 1 \text{ nA}$. Then the z -feedback loop was disabled and the bias swept to 0.4 V . The acquired spectra $dI/dU(U)$ for various lateral positions on the surface are shown in Figure 7.31 (d). The green spectrum is averaged over three query points on depressions, marked in Figure 7.31 (c). The black spectrum originates from elevations in the superstructure next to the depressions, circled in black. The spectra differ decidedly only in the lower conductance measured on depressions for positive bias. The spectrum in blue, representative of sites with intermediate corrugation, differs from the spectrum on depressions by a lowered conductance at around $U = -0.3 \text{ V}$.

Color maps of tunneling spectra acquired on two horizontal lines are displayed in Figure 7.31 (e). The lines are vertically spaced by 1.4 \AA and the spectroscopy points horizontally spaced by 1.1 \AA . The spectroscopic differences seen in the point spectra are reflected in the color plot of line B with an exceptionally high conductance at 0.4 V on point 5 and a reduced conductance at -0.3 V on points 1-3. This reduced conductance is reflected in line A as well on points 5-7, reflecting the geometry of the superstructure. A further correspondence of the constant-current image to spectroscopic features is identified by the reduced conductance measured at $U \approx -0.15 \text{ V}$ on or near elevations (points A1, A7, and B4) compared to neighboring sites. Still, the spectra acquired on these

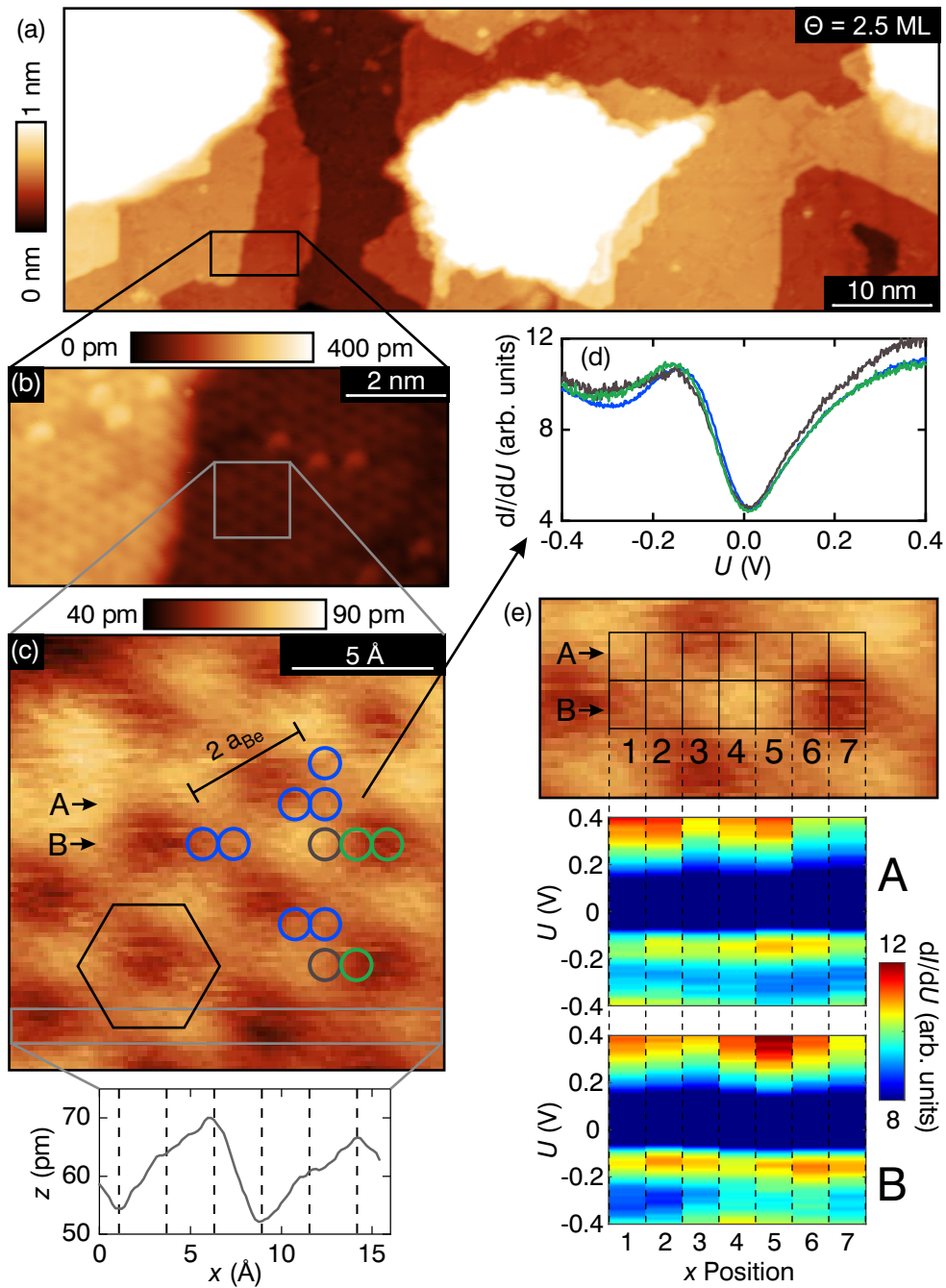


Figure 7.31: STS on various lattice sites of the (2×2) -ordered surface structure. (a,b) Constant-current STM images of $\Theta = 2.5$ ML Fe/Be(0001) grown at $T = 300^\circ\text{C}$. (c) Enlarged image of the surface structure under investigation with a lattice constant of $2a_{\text{Be}}$. A hexagon marks the unit cell. A line section across various lattice sites is shown in gray. Experimental parameters: (a) $U = 1.2$ V; (b,c) $U = -200$ mV, $I = 1$ nA, $T = 60$ K, Cr tip. (d) Tunneling spectra averaged over the sites marked with respective color in (c). (e) Color map of the tunneling conductance acquired on a spectroscopy grid of 2 by 7 query points. Stabilization conditions: $I = 1$ nA, $U = -400$ mV, $U_{\text{mod}} = 40$ mV, $f = 4814$ Hz.

various sites clearly share a common overall shape in the investigated bias range. While the structure of the (2×2) -ordered surface is reflected in the tunneling conductance, the minute site-dependent differences of the spectra do not serve to reveal which sites are inhibited by a specific atomic species.

7.5.2.1 Summary of Fe growth on Be(0001)

To summarize, Fe was found to grow in the Volmer-Weber growth mode on Be(0001) when deposited at room temperature. The resulting multilayer islands avoid coalescence into extended films. At substrate temperatures of 300 °C, deposited Fe intermixes with the substrate. Extended ordered films can be grown at this temperature. When the temperature is held for several hours or raised, these structures decompose and Be(0001) is exposed again on the sample surface. The films grown at elevated temperatures were identified as alloys of Fe and Be by a combined STM and AES study. The suspected composition is FeBe₂.

8 SP-STM investigation on the Fe/Be(0001) surface

The growth behavior of Fe on Be(0001) could be explained by the formation of an ordered alloy that resembles FeBe₂ in terms of its surface structure. In this chapter, the Fe/Be(0001) system will be investigated regarding its magnetic properties.

Alloys of Fe and Be have been studied regarding their magnetic properties by means of Mössbauer spectroscopy and magnetometry [170–172]. Ohta *et al.* found FeBe₂ with perfect stoichiometry to be ferromagnetic with an easy axis parallel to the *c*-axis [170]. In magnetometry experiments, the magnetization of polycrystalline FeBe₂ was found to saturate in an external magnetic field of 0.5 T [172]. Hysteresis measurements of FeBe₂ powder with a mean particle size of 1 μm showed a coercive field of $H_c = 1$ kOe that reduces to < 0.2 kOe for particles above 50 μm in size [171]. The Curie temperature was experimentally determined to be 880 K [172] and to decrease with increasing Be content [171]. In the C14 Laves structure of FeBe₂, all Fe atoms have four nearest Fe neighbors. For increasing Be content, the Fe sites in the lattice are gradually replaced by Be, altering the magnetic properties. At a Be concentration of 78 %-85 %, the alloy becomes paramagnetic at liquid nitrogen temperature [170].

The surface of FeBe(0001) films resembles the basal lattice plane of FeBe₂, as was shown in the previous chapter. Assuming the film to also retain the magnetic properties of FeBe₂, a ferromagnetic film could be assumed. However, the film grows strained with a lattice mismatch of 8 % on Be(0001). Strain and the proximity to a substrate have decisive influence on the magnetic ground state of thin films [2]. Fe for example that is ferromagnetic in bulk has a non-collinear magnetic ground state in thin films of two atomic layers grown on Ir(111) with a period in the local magnetization of only 1.9 nm [6]. The sensitivity of the magnetic properties of Fe-Be alloys on the particle size and stoichiometry suggest that the magnetic properties in thin Fe/Be(0001) films may deviate from bulk properties of FeBe₂. Thin films of Fe-Be alloys, have not been subject to investigations regarding their magnetic properties so far. SP-STM is a suitable tool for such an investigation as it combines surface sensitivity with a high lateral resolution.

In this chapter, the LT system, capable of applying an external magnetic field in the out-of-plane direction, is used to investigate the magnetic properties of Fe-Be islands with SP-STM. First, the magnetic properties of the STM tip are characterized based on the reference material system of two atomic layers of Fe/Ir(111). This tip is then used to measure the tunneling conductance on a Fe/Be(0001) sample in dependence of the external magnetic field. This study was supported by Karoline Oetker, who contributed to the preparation of a magnetically sensitive tip and to the data analysis as part of her master thesis [153].

8.1 Characterization of the tip magnetization on the reference sample Fe/Ir(111)

According to Equation (2.14), the differential conductance in SP-STM depends on the scalar product of the magnetizations of tip \vec{m}_T and sample \vec{m}_S

$$\frac{dI}{dU} \propto \vec{m}_T \vec{m}_S(eU). \quad (8.1)$$

Consequently, the detection of magnetic contrast in an out-of-plane magnetized sample requires a tip magnetization with an out-of-plane component. The magnetization of ferromagnetic domains in the sample can be aligned in an external field of sufficient magnitude. Likewise, a ferromagnetic tip apex may align with the external magnetic field. Therefore, the interpretation of changes in the differential conductance requires knowledge of the tip's response to an external magnetic field.

As a reference sample, two atomic layers of Fe were grown on Ir(111) with a deposition rate of 0.6 atomic layers per minute. The Ir substrate was held at an elevated temperature of 130 °C during deposition. An STM image of the resulting sample surface can be seen in Figure 8.1 (a). A terraced surface is visible. Fe double-layer areas can be identified by their characteristic dislocation lines [6]. These lines release strain between bcc-like areas on the pseudomorphically grown monolayer [4, 6]. Monolayer and triple-layer areas can be seen in addition to the predominantly occurring double-layer areas. A step edge in the substrate and local coverages are indicated.

Cycloidal spin spirals propagating along the dislocation lines represent the magnetic ground state of the Fe double-layer on Ir(111) [6]. These spin spirals offer a good reference system to calibrate the magnetization of a tip, because they contain magnetization components in all spatial directions and are insensitive to magnetic fields up to 9 T [63].

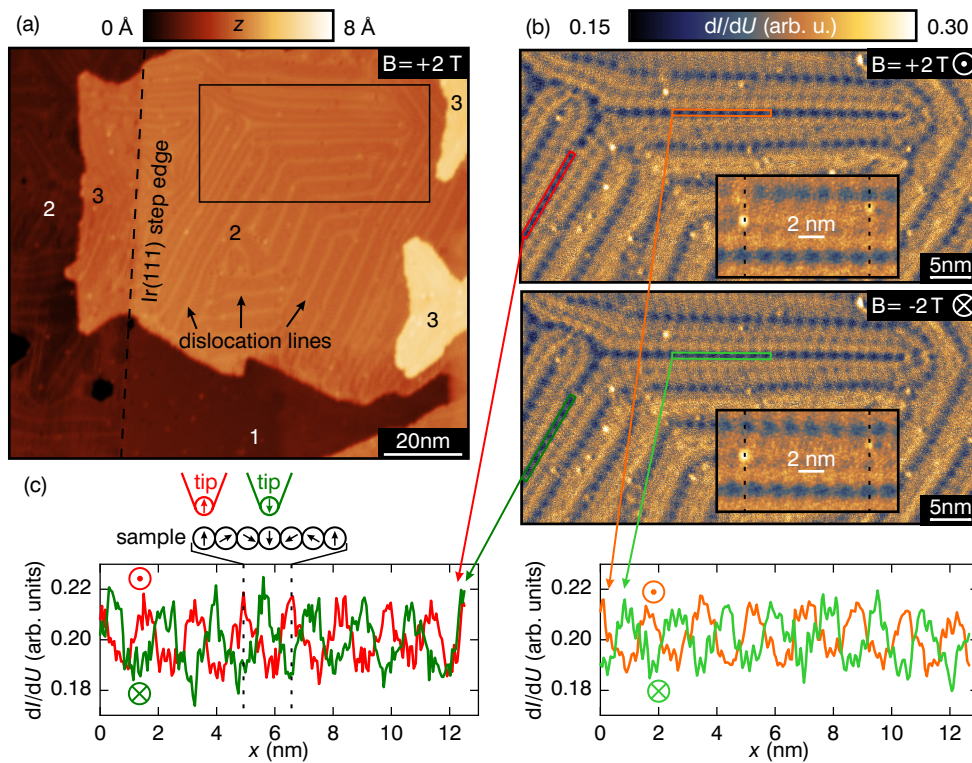


Figure 8.1: Magnetic characterization of the STM tip. (a) Constant-current STM image of 2 atomic layers of Fe on Ir(111). Local thicknesses of the Fe film are labeled with numbers in terms of atomic layers. A step edge in the Ir(111) substrate is indicated by a broken line. (b) Differential conductance images of spin spirals on the Fe double-layer indicated in (a), acquired with an out-of-plane magnetic field of $B = \pm 2\text{ T}$, respectively. (c) Line profiles of dI/dU along the lines indicated in (b). The spin spirals appear with a phase-shift of 180° for reversed external magnetic field. The magnified insets in (b) illustrate the apparent phase shift relative to impurities (broken lines). Parameters: $U = 200\text{ mV}$, $I = 500\text{ pA}$, $U_{\text{mod}} = 40\text{ mV}$, $f = 4277\text{ Hz}$, $T = 4.2\text{ K}$, Cr tip. The data was obtained and analyzed together with Karoline Oetker [153].

A magnetically sensitive tip was prepared by controlled contact with the sample surface and voltage pulses. This was realized by first stabilizing the tip above a triple-layer area at $U = 200\text{ mV}$ and $I = 500\text{ pA}$. Subsequently, the tip was driven towards the sample by 700 pm into contact and retracted under application of 2 V . This is done to either pick up Fe from the sample surface or reshape the Cr tip into a configuration with a spin-polarized state at the apex. Then pulses of a few volt were applied to the tip with a pulse length of 100 ms until magnetic contrast was achieved.

Differential conductance maps of the Fe double-layer acquired with such-prepared tips are shown in Figure 8.1 (b) for an out-of-plane external magnetic

field of $B = \pm 2$ T. The magnetic texture of the spin spiral is reflected in the periodic modulation of dI/dU along the dislocation lines. Figure 8.1 (c) depicts line profiles along the spin spirals taken in the areas marked in Figure 8.1 (b). The periodic signal shows a phase shift of 180° for external magnetic fields of opposite polarity. This is also evident in the magnified insets, where the phase of the spin spiral shifts relative to impurities on the surface with a change of sign of the external magnetic field. According to the scalar product in Equation (8.1), this corresponds to a sign change of \vec{m}_T or \vec{m}_S . As the sample magnetization is known to be independent of the applied magnetic field [6], it can be concluded that the tip magnetization aligns with the external field. The relative orientations of tip and sample magnetization are exemplarily indicated for one period of the spin spiral in the pictogram in Figure 8.1 (c). The magnitude of the spin-polarized tunneling conductance was quantified by sinusoidal fits to the line profiles. The amplitude of the differential conductance profile corresponds to the difference for parallel and antiparallel orientations of the tip and sample magnetization $dI/dU_{\uparrow\uparrow} - dI/dU_{\uparrow\downarrow}$. At $U = 200$ mV, the relative magnitude of the spin-polarized conductance relative to the spin averaged conductance

$$\frac{dI/dU_{\uparrow\uparrow} - dI/dU_{\uparrow\downarrow}}{dI/dU_{\uparrow\uparrow} + dI/dU_{\uparrow\downarrow}}$$

amounts to (5.0 ± 0.5) %.

The tip material Cr itself is antiferromagnetic with a randomly oriented magnetic moment at the apex [173]. Because of the antiferromagnetic order, it is generally not influenced by an external magnetic field [2]. The alignment of the tip's magnetization in the external field suggests that Fe may have been picked up from the sample and transferred to the tip apex during contact. Alternatively, uncompensated magnetic moments that align with the external field may be present at the apex cluster of the Cr tip [174, 175]. In either case, this means that an out-of-plane magnetic sensitivity of the tip can be established through alignment with the external field. That is an advantage over a strictly antiferromagnetic tip with a random orientation and an uncertain out-of-plane component of the magnetization. The caveat of a ferromagnetic tip is that it may reverse its magnetization simultaneously with a sample in a reversed external magnetic field, thus keeping the relative alignment of \vec{m}_T and \vec{m}_S and yielding no discernible contrast. This tip with a proven out-of-plane magnetic sensitivity in an external magnetic field was applied to an Fe/Be(0001) sample in a subsequent measurement.

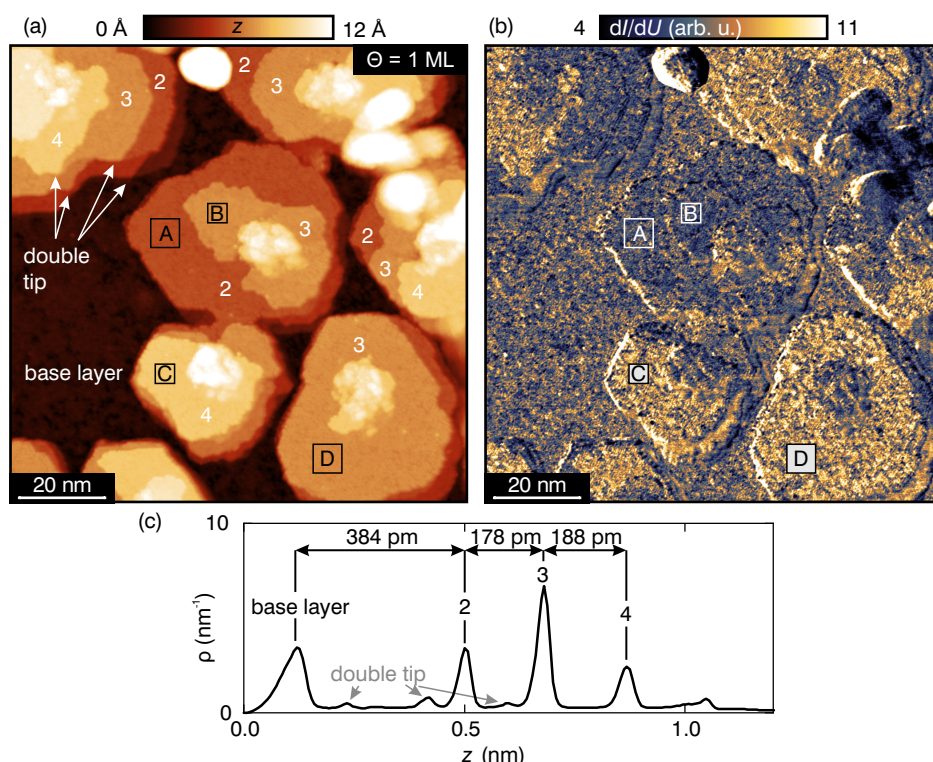


Figure 8.2: (a) Constant-current STM image of $\Theta = 1$ ML Fe on Be(0001) grown at $T = 215$ °C. The local thickness of the grown islands is indicated in atomic layers with respect to the base layer. (b) Simultaneously acquired differential conductance. (c) Histogram plot of the z -values in (a). Major peaks are labeled according to the corresponding layers in (a). Minor peaks originate from double-tip effects marked in (a). Parameters: $U = -0.3$ V, $I = 0.2$ nA, $U_{\text{mod}} = 40$ mV, $f = 4277$ Hz, $T = 4.2$ K, $B = -2$ T, Cr tip.

8.2 Probing Fe-Be islands with a spin-sensitive STM tip

The reference sample was replaced by a sample of $\Theta = 1$ ML of Fe on Be(0001). The deposition rate was 0.09 ML per minute and the substrate temperature was limited to $T = 215$ °C during deposition. The temperature was deliberately kept below the 300 °C used in the VT system to prevent the possibility of excessive heating leading to a surface dominated by bare Be(0001) instead of the alloyed phase. The reason is that the sample is not clamped to the manipulator in the LT system, which is the case in the VT system, and the heat conductance between the sample and the temperature sensor is expected to be lower.

An STM image of the resulting surface is shown in Figure 8.2 (a). The surface morphology resembles the known growth with pyramidal islands on a

rough base layer observed in the VT system in the previous chapter. A histogram of the measured z -values is plotted in Figure 8.2 (c). Three main levels in height can be discerned, being two, three, and four atomic layers above the base layer. Minor peaks in the histogram originate from a second microtip, receded by 265 pm with respect to the dominantly imaging microtip. Artifacts caused by this double-tip are indicated in Figure 8.2 (a) at the edges of islands. With the decay of the tunneling current of about one order of magnitude per 100 pm, the influence of this double-tip on extended terraces, away from higher terraces, is negligible.

Figure 8.2 (b) depicts the differential conductance at $U = -0.3$ V measured simultaneously with z . A contrast in dI/dU between different islands and terraces can be seen, for example between the terraces labeled A and B on the one hand, and C and D on the other hand. This contrast is independent of apparent height with terraces B and D both lying three atomic layers above the base layer. The contrast may be purely electronic and stem from different stackings within the islands or different terminations of the surface. Variations of the tunneling conductance in the Fe/Be(0001) film were also observed with nonmagnetic tips. Alternatively, it may originate from different magnetization directions of the islands, leading to a tunneling magnetoresistance. The out-of-plane sensitivity of the tip demonstrated in Figure 8.1 can be used to systematically look for out-of-plane magnetized domains in the Fe/Be(0001) film, as would be expected for bulk-like FeBe₂.

The tunneling magnetoresistance is in general a bias-dependent phenomenon. Four rectangular areas marked on terraces A-D were chosen for a bias-dependent investigation of the tunneling conductance. The tip magnetization was shown to align with an external magnetic field of $|B| = 2$ T. To investigate the dependence of the differential conductance on the magnetization direction of the tip, bias sweeps at alternating signs of the external magnetic field were conducted on these four areas. First, with $B = 2$ T, the tip was stabilized on area A at a setpoint of $I = 0.2$ nA and the differential conductance was recorded for -0.7 V $\leq U \leq 0.7$ V with active z -feedback, keeping the current constant. This measurement was repeated in turn on areas B-D. Last, the measurement was repeated on area A to examine the reproducibility of the experiment and to sense possible changes of the tip during the measurement run. Afterwards, the external magnetic field was reversed and the measurement was repeated on all areas.

The resulting spectra that are averaged over typically 16 points per area are shown in Figure 8.3 (b). They are displayed as $\frac{dI/dU}{I/U}$ because of diverging values of dI/dU as measured by lock-in technique at constant current for bias

8.2 Probing Fe-Be islands with a spin-sensitive STM tip

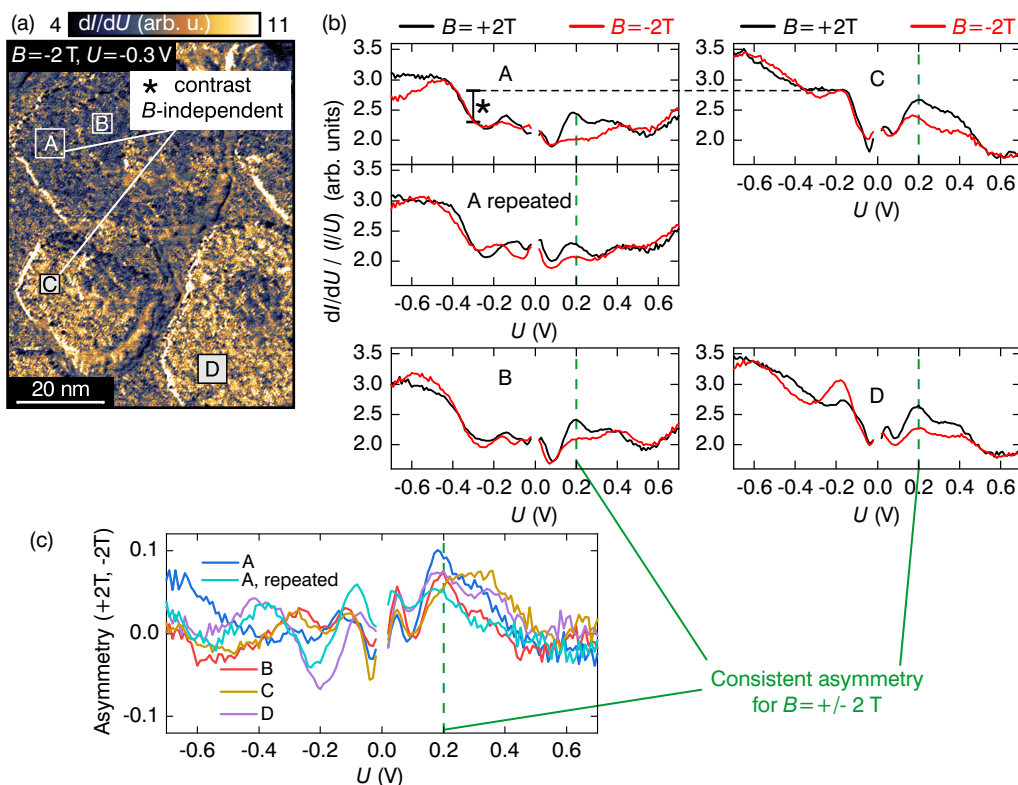


Figure 8.3: Tunneling spectroscopy on Fe-Be islands in dependence of the external magnetic field. (a) dI/dU image of the Fe/Be(0001) islands under investigation. The spectroscopy sites are marked with rectangles. Parameters: $U = -0.3$ V, $I = 0.2$ nA, $U_{\text{mod}} = 40$ mV, $f = 4277$ Hz, $T = 4.2$ K, $B = -2$ T, Cr tip. (b) Differential conductance acquired on the areas A-D marked in (a) with active z -feedback and normalized by (I/U) for $B = 2$ T and -2 T, respectively. Spectroscopy parameters: $I = 0.2$ nA, $T = 4.2$ K, $U_{\text{mod}} = 20$ mV, $f = 4277$ Hz, Cr tip. (c) Asymmetry calculated from the spectra above. At $U = 0.2$ V, an asymmetry is measured on all areas. The data was obtained and analyzed together with Karoline Oetker [153].

values close to zero. Spectra taken on areas C and D exhibit a steep increase of dI/dU from $U = 0$ V towards negative bias. The spectra acquired on areas A and B differ from those taken on C and D, mainly in their lower conductance at negative U and higher conductance at $U > 0.6$ V. This difference observed in the spectra on areas A and C is marked by an asterisk at $U = -0.3$ V and is reflected in the contrast of spatially resolved dI/dU in Figure 8.3 (a). This contrast between islands is evident to be independent of the external magnetic field and can be excluded to arise from out-of-plane magnetized domains of opposite magnetization direction.

For $B = -2$ T, changes in all spectra with respect to those taken at $B = 2$ T

can be observed. For a quantitative evaluation of these changes, the asymmetry

$$\frac{\frac{dI}{dU} / I (+2 \text{ T}) - \frac{dI}{dU} / I (-2 \text{ T})}{\frac{dI}{dU} / I (+2 \text{ T}) + \frac{dI}{dU} / I (-2 \text{ T})}$$

was calculated. The resulting curves are shown in Figure 8.3 (c). For negative bias values the curves are diverging but at positive bias they are more concordant. The tip magnetization \vec{m}_T was previously observed to align with an external magnetic field. With a switching tip magnetization and otherwise stable conditions, a consistent asymmetry profile for measurements on the same area would be expected. At negative bias values, the calculated asymmetry curves for area A show inconsistencies that can not be explained by only the changing tip magnetization.

Figure 8.4 shows a comparison of two spectroscopy experiments performed on area A in an external magnetic field of $B = 2 \text{ T}$. The spectra differ at $U = 0.2 \text{ V}$ although they were acquired under nominally equal experimental conditions. This difference may arise from changes of the electronic structure of the tip apex, or from the sampling of 16 points on the heterogeneous Fe/Be(0001) surface.

Nevertheless, a sizable asymmetry is found at $U = 0.2 \text{ V}$ in all experiments in Figure 8.3 (c). This consistent shift of the measured differential conductance upon reversal of the sign of the magnetic field may be an indication of magnetoresistance, with the tip aligning in the external field while the out-of-plane component of the sample magnetization does not. In order to test this hypothesis of a switching tip magnetization and a constant sample magnetization and reproduce the observation, differential conductance images at $U = 0.2 \text{ V}$ were acquired on the investigated surface area with $B = -2 \text{ T}$ and $B = 2 \text{ T}$ in direct succession. The corresponding images are displayed in Figure 8.5 (a) and (b).

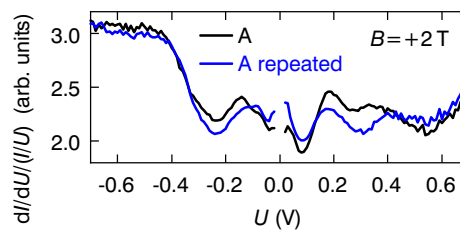


Figure 8.4: Comparison of tunneling spectra acquired on area A in Figure 8.3 under nominally equal experimental conditions in an external magnetic field of $B = +2 \text{ T}$. Spectroscopy parameters: z -feedback on, $I = 0.2 \text{ nA}$, $T = 4.2 \text{ K}$, $U_{\text{mod}} = 20 \text{ mV}$, $f = 4277 \text{ Hz}$, Cr tip. The data was obtained and analyzed together with Karoline Oetker [153].

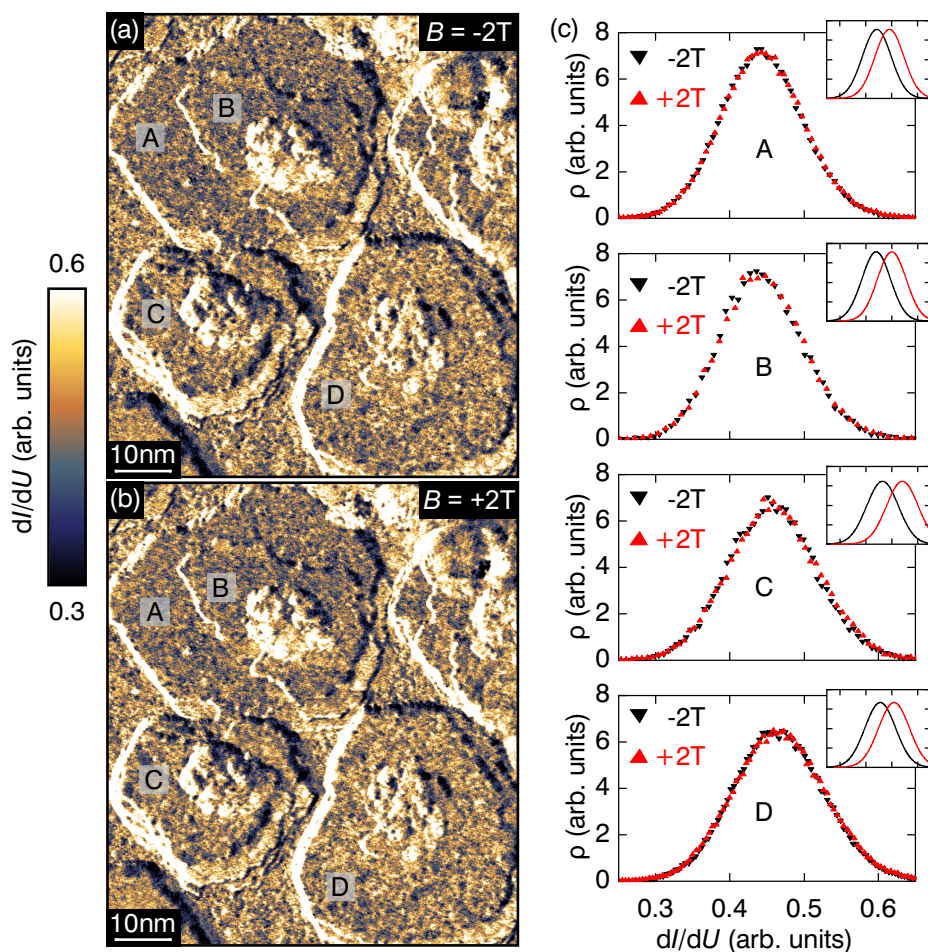


Figure 8.5: (a), (b) Differential conductance maps of the areas A-D on Fe-Be islands acquired in external magnetic fields of 2 T and -2 T, respectively. (c) Histograms of the dI/dU -values measured on terraces A-D. On none of the areas a shift with the sign change of the external magnetic field occurred. The insets represent expectations for the B -dependent conductance based on the asymmetry in Figure 8.3 (c). Parameters: $U = 0.2$ V, $I = 0.2$ nA, $U_{\text{mod}} = 20$ mV, $f = 4277$ Hz, $T = 4.2$ K, Cr tip.

An obvious change in the differential conductance with the external magnetic field is not evident.

For a better comparison, histograms of the dI/dU -values on the terraces A-D are compiled in Figure 8.5 (c). The histograms neither shift, nor broaden with the applied magnetic field, in contrast to the expectations from the spectroscopy experiment. According to the measured asymmetry in the spectroscopy experiment, a shift of the mean conductance would be expected as indicated in the insets.

Still, the contrast between areas (A,B) and (C,D) persists also at $U = 0.2$ V. Consequently, this contrast has to stem from different electronic structures, for example due to different surface terminations as discussed in section 7.5. Also stacking faults inside the islands, deviating from the preferred hcp-stacking of FeBe₂, are a possible cause for the observed contrast.

To understand the discrepancy between the spectroscopy experiment in Figure 8.3 showing an apparent influence of the external magnetic field and the scans in Figure 8.5 showing none, the relevant experimental conditions in both experiments have to be examined in detail. The scans shown in Figure 8.5 were surely acquired with the same microscopic tip. This becomes clear from the identical distribution of dI/dU on all four areas. Previously, on Fe/Ir(111), a magnetic sensitivity of the tip at $U = 0.2$ V was demonstrated. One obvious explanation of this behavior is a loss of the ferromagnetic tip apex in between the measurements. Due to the rough Be(0001) surface, it is thinkable that the experiment was not performed with the same tip apex previously tested on Fe/Ir(111).

Another possibility would be that the Fe-Be system is paramagnetic. In this case no tunneling magnetoresistance would be expected. Experiments on bulk material have shown that the ferromagnetism of Fe-Be alloys is carried mainly by Fe atoms with three or four Fe atoms as nearest neighbors [170]. The islands investigated here are only a few atomic layers thick and their internal stoichiometry is unknown. Apart from that, the islands may be ferromagnetic but with a saturated magnetization aligned with the external magnetic field. With the tip magnetization also following the external magnetic field, this would mean a parallel alignment of \vec{m}_T and \vec{m}_S for both signs of the external magnetic field, and thus no discernible contrast. In this regard, it is to note, that no magnetic contrast was observed for $B = \pm 0.1$ T, either.

Perspectives to determine the magnetic properties of Fe/Be(0001) films

For the determination of the magnetism in Fe/Be(0001), a tip with well characterized and well defined magnetic properties is vital. Ferromagnetic tips with known out-of-plane magnetization could be employed to test the hypothesis that the out-of-plane easy magnetization axis of bulk FeBe₂ is retained in intermixed thin films of Fe on Be(0001). Alternatively, in-plane sensitive Fe coated W tips [11] could be used to search for in-plane magnetized domains of Fe/Be(0001). With such tips of ascertained magnetization direction, magnetic field sweeps can be used to investigate the hysteresis of Fe/Be(0001) films.

However, ferromagnetic tips have the disadvantage of creating stray fields that can locally magnetize a ferromagnetic sample, thus possibly preventing contrast

in SP-STM experiments. If this is the case, antiferromagnetic Cr tips with a reliable magnetic sensitivity may be required. For Cr tips with an arbitrary and a priori unknown orientation of the magnetic moment at the tip apex, characterization on a reference system and a subsequent transfer of the same microtip to the Fe/Be(0001) sample is important. Cr tips were for example successfully applied in hysteresis measurements of the in-plane ferromagnetically ordered single layer of GdAu₂ on Au(111) [176].

The Cr tips employed in this work were etched from polycrystalline material. The etching process will in general occur with different rates for different crystallographic directions. With respect to the grains in polycrystalline material, this will lead to a granularity of the tip. A Cr tip etched from a single crystal may be of advantage in this respect, due to an expected uniform etching of the apex culminating in a sharp tip. The sharpness brings two important advantages. First, it is the prerequisite to reproducibly land the same microtip on a reference sample and subsequently on the actual sample under investigation. And second, a blunt Cr tip has a lower chance of yielding spin contrast, as antiferromagnetically coupled Cr layers of opposite spin direction may add to zero net magnetization at the apex [2].

Summary of SP-STM investigations on Fe/Be(0001)

In summary, an STM tip with out-of-plane magnetic sensitivity was prepared and its performance was demonstrated on the reference sample Fe/Ir(111). This tip was applied to Fe-Be islands grown on Be(0001). STS in an out-of-plane external magnetic field did not resolve the question if magnetic order exists in these islands. In order to demonstrate robust evidence of magnetic order in these structures and to map their characteristics, such as domain structure and coercivity, SP-STM experiments with more resilient probe tips will be necessary. In particular, the differential tunneling conductance between Fe/Be(0001) films and a tip of proven magnetic sensitivity has to be measured on different length scales from extended terraces down to their (2 × 2)-ordered atomic structure, over a wide bias range, and for varying flux density of the external magnetic field ranging from some mT to several T.

9 Conclusion and perspective

In this thesis, the Be(0001) surface was cleaned and characterized regarding its electronic properties. The growth of Fe on this surface was studied with regard to the feasibility of stabilizing pseudomorphical Fe overlayers that are compressed compared to α -Fe and may allow insight into the physical properties of iron's ϵ -phase.

First, a cleaning procedure that prepares the Be(0001) surface for investigations with the STM and for growth of Fe adlayers was developed in this work. Previous preparation procedures for STM investigations of Be(0001) and Be(10 $\bar{1}$ 0) relied on a limited annealing temperature after sputtering of 450 °C and 630 °C, respectively, in order to limit the surface segregation of bulk impurities [37, 84]. Such a preparation procedure is unfeasible to investigate the growth of Fe adlayers, as a growth study requires annealing of the deposited film. Furthermore, a higher annealing temperature was found to entail better ordered and larger extended substrate terraces. The cleaning procedure developed in this work consists of two steps. In an initial step, oxide layers are removed from the surface by Ar⁺-sputtering, followed by annealing of the sample surface at high temperatures up to 800 °C. In a subsequent step, the sputter ion energy and sample temperature have to be harmonized in order to preferentially sputter impurities and create a depletion zone at the Be(0001) surface.

The band structure of Be(0001) was probed by scanning tunneling spectroscopy. A surface state with parabolic dispersion was identified inside the partial bulk band gap. Standing waves seen in STM on Be(0001) were identified as Friedel oscillations of this surface state, in agreement with the picture of a two-dimensional electron gas. Strong inelastic contributions to the measured tunneling conductance in STM were unveiled and assigned to phonon excitations.

This work was motivated by the vision of realizing a highly compressed hcp-Fe film by pseudomorphic growth on Be(0001). The growth of Fe on Be(0001) was studied in dependence of the deposited Fe amount and of the deposition temperature. Bare Be was found to be favored over the formation of a wetting layer on the surface, and clustering of Fe atoms over pseudomorphic growth. At room temperature, Fe islands of a few nanometers in diameter grow in a three-dimensional fashion. These islands roughen with further annealing of

the sample and areas of Be(0001) emerge between these islands with increasing temperature. When Fe is deposited onto samples held at elevated temperatures, a metastable phase ensues, and ordered, extended films with a hexagonal surface unit cell of $2a_{\text{Be}}$ form. Auger electron spectroscopy indicates that an intermixing of Fe and Be accompanies the formation of this ordered phase. Based on their microscopic surface structure, these films are identified as an alloy, reflecting the order of FeBe_2 in the hexagonal C14 Laves phase. The alloyed films disintegrate with prolonged heating.

In the bulk phase, FeBe_2 is ferromagnetic with an easy axis perpendicular to its basal plane [170, 172]. Scanning tunneling spectroscopy with a spin-sensitive tip on intermixed Fe-Be films inside an external out-of-plane magnetic field did not reveal conclusive evidence for ferromagnetic order in the film.

Perspectively, SP-STM tips with a proven spin-sensitivity can be employed to study the magnetic configuration of Fe-Be films. On the (2×2) -ordered alloyed films, low temperature tunneling spectroscopy could for example have the potential to resolve local magnetic moments at Fe sites. Further, deposition of Fe onto Be(0001) at cryogenic temperatures may enable pseudomorphically grown overlayers. This would be the case if a regime of temperature and coverage can be found, where the mobility of Fe adatoms is high enough to move away from their landing sites but too low to overcome the energy barrier for intermixing with the substrate, observed here to occur at least for $T \geq 215^\circ\text{C}$, and for forming three-dimensional clusters, which occurs already at room temperature.

With the established cleaning procedure for Be(0001) and its thorough characterization by scanning tunneling spectroscopy, this surface is now available as a substrate material with peculiar electronic properties. By deposition of metals onto this substrate at elevated temperatures, the alloying of Be and other metals can be studied on the atomic scale using STM.

Bibliography

- [1] L. Zhou, J. Wiebe, S. Lounis, E. Vedmedenko, F. Meier, S. Blügel, P. H. Dederichs, and R. Wiesendanger, “Strength and directionality of surface Ruderman–Kittel–Kasuya–Yosida interaction mapped on the atomic scale”, *Nature Physics* **6**, 187 (2010).
- [2] R. Wiesendanger, “Spin mapping at the nanoscale and atomic scale”, *Reviews of Modern Physics* **81**, 1495 (2009).
- [3] S. Krause, L. Berbil-Bautista, G. Herzog, M. Bode, and R. Wiesendanger, “Current-Induced Magnetization Switching with a Spin-Polarized Scanning Tunneling Microscope”, *Science* **317**, 1537 (2007).
- [4] K. von Bergmann, S. Heinze, M. Bode, E. Y. Vedmedenko, G. Bihlmayer, S. Blügel, and R. Wiesendanger, “Observation of a Complex Nanoscale Magnetic Structure in a Hexagonal Fe Monolayer”, *Physical Review Letters* **96**, 167203 (2006).
- [5] S. Heinze, K. von Bergmann, M. Menzel, J. Brede, A. Kubetzka, R. Wiesendanger, G. Bihlmayer, and S. Blügel, “Spontaneous atomic-scale magnetic skyrmion lattice in two dimensions”, *Nature Physics* **7**, 713 (2011).
- [6] P.-J. Hsu, A. Finco, L. Schmidt, A. Kubetzka, K. von Bergmann, and R. Wiesendanger, “Guiding Spin Spirals by Local Uniaxial Strain Relief”, *Physical Review Letters* **116**, 017201 (2016).
- [7] A. Finco, P.-J. Hsu, A. Kubetzka, K. von Bergmann, and R. Wiesendanger, “Tailoring noncollinear magnetism by misfit dislocation lines”, *Physical Review B* **94**, 214402 (2016).
- [8] P.-J. Hsu, A. Kubetzka, A. Finco, N. Romming, K. von Bergmann, and R. Wiesendanger, “Electric-field-driven switching of individual magnetic skyrmions”, *Nature Nanotechnology* **12**, 123 (2017).
- [9] U. Gradmann and G. Waller, “Periodic lattice distortions in epitaxial films of Fe(110) on W(110)”, *Surface Science* **116**, 539 (1982).

- [10] H.-J. Elmers, J. Hauschild, and U. Gradmann, “Critical behavior of the uniaxial ferromagnetic monolayer Fe(110) on W(110)”, [Physical Review B](#) **54**, 15224 (1996).
- [11] A. Kubetzka, P. Ferriani, M. Bode, S. Heinze, G. Bihlmayer, K. von Bergmann, O. Pietzsch, S. Blügel, and R. Wiesendanger, “Revealing Antiferromagnetic Order of the Fe Monolayer on W(001): Spin-Polarized Scanning Tunneling Microscopy and First-Principles Calculations”, [Physical Review Letters](#) **94**, 087204 (2005).
- [12] S. Ouazi, T. Pohlmann, A. Kubetzka, K. von Bergmann, and R. Wiesendanger, “Scanning tunneling microscopy study of Fe, Co and Cr growth on Re(0001)”, [Surface Science](#) **630**, 280 (2014).
- [13] A. Palacio-Morales, A. Kubetzka, K. von Bergmann, and R. Wiesendanger, “Coupling of Coexisting Noncollinear Spin States in the Fe Monolayer on Re(0001)”, [Nano Letters](#) **16**, 6252 (2016).
- [14] T. Takahashi and W. A. Bassett, “High-Pressure Polymorph of Iron”, [Science](#) **145**, 483 (1964).
- [15] L.-G. Liu and W. A. Bassett, “The melting of iron up to 200 kbar”, [Journal of Geophysical Research](#) **80**, 3777 (1975).
- [16] L. Stixrude, R. E. Cohen, and D. J. Singh, “Iron at high pressure: Linearized-augmented-plane-wave computations in the generalized-gradient approximation”, [Physical Review B](#) **50**, 6442 (1994).
- [17] R. J. Hemley and H. K. Mao, “In Situ Studies of Iron under Pressure: New Windows on the Earth’s Core”, [International Geology Review](#) **43**, 1 (2001).
- [18] O. Mathon, F. Baudelet, J. P. Itié, A. Polian, M. d’Astuto, J. C. Chervin, and S. Pascarelli, “Dynamics of the Magnetic and Structural α - ϵ Phase Transition in Iron”, [Physical Review Letters](#) **93**, 255503 (2004).
- [19] S. Nasu, T. Sasaki, T. Kawakami, T. Tsutsui, and S. Endo, “Mössbauer study of ϵ -Fe under an external magnetic field”, [Journal of Physics: Condensed Matter](#) **14**, 11167 (2002).
- [20] A. B. Papandrew, M. S. Lucas, R. Stevens, I. Halevy, B. Fultz, M. Y. Hu, P. Chow, R. E. Cohen, and M. Somayazulu, “Absence of Magnetism in Hcp Iron-Nickel at 11 K”, [Physical Review Letters](#) **97**, 087202 (2006).
- [21] G. Steinle-Neumann, L. Stixrude, and R. E. Cohen, “First-principles elastic constants for the hcp transition metals Fe, Co, and Re at high pressure”, [Physical Review B](#) **60**, 791 (1999).

-
- [22] G. Steinle-Neumann, L. Stixrude, and R. E. Cohen, “Erratum: First-principles elastic constants for the hcp transition metals Fe, Co, and Re at high pressure [Phys. Rev. B 60 , 791 (1999)]”, [Physical Review B](#) **69**, 219903(E) (2004).
- [23] R. Lizárraga, L. Nordström, O. Eriksson, and J. Wills, “Noncollinear magnetism in the high-pressure hcp phase of iron”, [Physical Review B](#) **78**, 064410 (2008).
- [24] R. J. Teitel and M. Cohen, “The Beryllium-iron System”, Transactions of the Metallurgical Society of AIME **185**, 285 (1949).
- [25] M. Bode, R. Pascal, M. Dreyer, and R. Wiesendanger, “Nanostructural and local electronic properties of Fe/W(110) correlated by scanning tunneling spectroscopy”, [Physical Review B](#) **54**, R8385 (1996).
- [26] U. O. Karlsson, S. A. Flodström, R. Engelhardt, W. Gädeke, and E. E. Koch, “Intrinsic surface state on Be(0001)”, [Solid State Communications](#) **49**, 711 (1984).
- [27] R. A. Bartynski, E. Jensen, T. Gustafsson, and E. W. Plummer, “Angle-resolved photoemission investigation of the electronic structure of Be: Surface states”, [Physical Review B](#) **32**, 1921 (1985).
- [28] K. B. Ray, X. Pan, and E. W. Plummer, “The interaction of H with Be(0001): a photoemission investigation”, [Surface Science](#) **285**, 66 (1993).
- [29] I. Vobornik, J. Fujii, M. Mulazzi, G. Panaccione, M. Hochstrasser, and G. Rossi, “Surface electron bands and Fermi surface of Be(0001)”, [Physical Review B](#) **72**, 165424 (2005).
- [30] I. Vobornik, J. Fujii, M. Hochstrasser, D. Krizmancic, C. E. Viol, G. Panaccione, S. Fabris, S. Baroni, and G. Rossi, “Three-Dimensional Tomography of the Beryllium Fermi Surface: Surface Charge Redistribution”, [Physical Review Letters](#) **99**, 166403 (2007).
- [31] E. W. Plummer and J. B. Hannon, “The surfaces of beryllium”, [Progress in Surface Science](#) **46**, 149 (1994).
- [32] E. V. Chulkov, V. M. Silkin, and E. N. Shirykalov, “Surface electronic structure of Be(0001) and Mg(0001)”, [Surface Science](#) **188**, 287 (1987).
- [33] P. J. Feibelman and R. Stumpf, “Physics of the Be(0001) surface core-level spectrum”, [Physical Review B](#) **50**, 17480 (1994).
- [34] P. Hofmann, B. G. Briner, M. Doering, H.-P. Rust, E. W. Plummer, and A. M. Bradshaw, “Anisotropic Two-Dimensional Friedel Oscillations”, [Physical Review Letters](#) **79**, 265 (1997).

- [35] A. Fert and P. M. Levy, “Role of Anisotropic Exchange Interactions in Determining the Properties of Spin-Glasses”, *Physical Review Letters* **44**, 1538 (1980).
- [36] M. F. Crommie, C. P. Lutz, and D. M. Eigler, “Imaging standing waves in a two-dimensional electron gas”, *Nature* **363**, 524 (1993).
- [37] P. T. Sprunger, L. Petersen, E. W. Plummer, E. Lægsgaard, and F. Besenbacher, “Giant Friedel Oscillations on the Beryllium(0001) Surface”, *Science* **275**, 1764 (1997).
- [38] N. W. Ashcroft and N. D. Mermin, *Solid State Physics* (Holt, Rinehart and Winston, New York, 1976).
- [39] R. O. Adams, “Cleaning a (0001) beryllium surface”, *Materials Research Bulletin* **2**, 469 (1967).
- [40] A. K. Green and E. Bauer, “Work function and purity of the Beryllium (0001) surface”, *Surface Science* **74**, 676 (1978).
- [41] M. Hengsberger, D. Purdie, P. Segovia, M. Garnier, and Y. Baer, “Photoemission Study of a Strongly Coupled Electron-Phonon System”, *Physical Review Letters* **83**, 592 (1999).
- [42] J. Bardeen, “Tunnelling from a Many-Particle Point of View”, *Physical Review Letters* **6**, 57 (1961).
- [43] C. J. Chen, *Introduction to Scanning Tunneling Microscopy*, Vol. 4, Oxford Series in Optical and Imaging Sciences (Oxford University Press, New York, 1993).
- [44] J. Tersoff and D. R. Hamann, “Theory and Application for the Scanning Tunneling Microscope”, *Physical Review Letters* **50**, 1998 (1983).
- [45] R. Wiesendanger, *Scanning Probe Microscopy and Spectroscopy: Methods and Applications* (Cambridge University Press, Cambridge/New York, 1994).
- [46] R. J. Hamers, “Atomic-Resolution Surface Spectroscopy with the Scanning Tunneling Microscope”, *Annual Review of Physical Chemistry* **40**, 531 (1989).
- [47] V. A. Ukraintsev, “Data evaluation technique for electron-tunneling spectroscopy”, *Physical Review B* **53**, 11176 (1996).
- [48] J. Li, W.-D. Schneider, and R. Berndt, “Local density of states from spectroscopic scanning-tunneling-microscope images: Ag(111)”, *Physical Review B* **56**, 7656 (1997).

-
- [49] J. Kröger, L. Limot, H. Jensen, R. Berndt, S. Crampin, and E. Pehlke, “Surface state electron dynamics of clean and adsorbate-covered metal surfaces studied with the scanning tunnelling microscope”, [Progress in Surface Science](#) **80**, 26 (2005).
- [50] J. A. Støvneng and P. Lipavský, “Thermopower in scanning-tunneling-microscope experiments”, [Physical Review B](#) **42**, 9214 (1990).
- [51] C. Friesen, H. Osterhage, J. Friedlein, A. Schlenhoff, R. Wiesendanger, and S. Krause, “Scanning Seebeck tunneling microscopy”, [Journal of Physics D: Applied Physics](#) **51**, 324001 (2018).
- [52] J. C. Slonczewski, “Conductance and exchange coupling of two ferromagnets separated by a tunneling barrier”, [Physical Review B](#) **39**, 6995 (1989).
- [53] D. Wortmann, S. Heinze, P. Kurz, G. Bihlmayer, and S. Blügel, “Resolving Complex Atomic-Scale Spin Structures by Spin-Polarized Scanning Tunneling Microscopy”, [Physical Review Letters](#) **86**, 4132 (2001).
- [54] P. K. Hansma, “Inelastic electron tunneling”, [Physics Reports](#) **30**, 145 (1977).
- [55] M. Schackert, T. Märkl, J. Jandke, M. Hölzer, S. Ostanin, E. K. U. Gross, A. Ernst, and W. Wulfhekel, “Local Measurement of the Eliashberg function of Pb Islands: Enhancement of Electron-Phonon Coupling by Quantum Well States”, [Physical Review Letters](#) **114**, 047002 (2015).
- [56] J. Jandke, P. Hlobil, M. Schackert, W. Wulfhekel, and J. Schmalian, “Coupling to real and virtual phonons in tunneling spectroscopy of superconductors”, [Physical Review B](#) **93**, 060505(R) (2016).
- [57] J. G. Adler, H. J. Kreuzer, and W. J. Wattamaniuk, “Multichannel Theory of Inelastic Electron Tunneling in Normal Metal-Insulator-Metal Junctions”, [Physical Review Letters](#) **27**, 185 (1971).
- [58] K. D. Childs, B. A. Carlson, L. A. LaVanier, J. F. Moulder, D. F. Paul, W. F. Stickle, and D. G. Watson, *Handbook of Auger Electron Spectroscopy: A Book of Reference Data for Identification and Interpretation in Auger Electron Spectroscopy*, 3rd ed. (Physical Electronics, Inc., Eden Prairie, MN, 1995).
- [59] J. P. Langeron, L. Minel, J. L. Vignes, S. Bouquet, F. Pellerin, G. Lorang, P. Ailloud, and J. Le Héricy, “An important step in quantitative Auger analysis: The use of peak to background ratio”, [Surface Science](#) **138**, 610 (1984).

- [60] L. E. Davis, N. C. McDonald, P. W. Palmberg, G. E. Riach, and R. E. Weber, *Handbook of Auger Electron Spectroscopy: A Reference Book of Standard Data for Identification and Interpretation of Auger Electron Spectroscopy Data*, 2nd ed. (Physical Electronics Division, Perkin Elmer Corporation, Eden Prairie, MN, 1976).
- [61] J. Harm, “Entwicklung und Aufbau einer Tieftemperatur-Ultrahochvakuumanlage für spinaufgelöste Mehrfach-Spitzen-Rastertunnelmikroskopie mit hoher Zeitauflösung”, PhD thesis (Universität Hamburg, Hamburg, 2019).
- [62] M. Bode, S. Krause, L. Berbil-Bautista, S. Heinze, and R. Wiesendanger, “On the preparation and electronic properties of clean W(110) surfaces”, *Surface Science* **601**, 3308 (2007).
- [63] A. Finco, “Interplay between non-collinear magnetism and nanoscale structural properties in epitaxial Fe-based ultrathin films”, PhD thesis (Universität Hamburg, Hamburg, 2018).
- [64] A. Schlenhoff, “Imaging and Switching Individual Nanomagnets with Spin-Polarized Scanning Field Emission Microscopy”, PhD thesis (Universität Hamburg, Hamburg, 2013).
- [65] J. Friedlein, “A radio frequency-spin-polarized-scanning tunneling microscope for spin dynamics experiments”, PhD thesis (Universität Hamburg, Hamburg, 2018).
- [66] J.-H. Schmidt, “Wachstum von Eisenfilmen auf Beryllium(0001)”, Bachelor thesis (Universität Hamburg, Hamburg, 2019).
- [67] I. Ekvall, E. Wahlström, D. Claesson, H. Olin, and E. Olsson, “Preparation and characterization of electrochemically etched W tips for STM”, *Measurement Science and Technology* **10**, 11 (1999).
- [68] C. Friesen, “Magneto-Seebeck tunneling across a vacuum barrier”, PhD thesis (Universität Hamburg, Hamburg, 2019).
- [69] H. Osterhage, “Calorimetric experiments on Fe/W(110) using scanning tunneling microscopy”, Master thesis (Universität Hamburg, Hamburg, 2016).
- [70] T. Hänke, “A new variable-temperature scanning tunneling microscope and temperature-dependent spin-polarized scanning tunneling spectroscopy on the Cr(001) surface”, PhD thesis (Universität Hamburg, Hamburg, 2005).

-
- [71] J. Friedlein, J. Harm, P. Lindner, L. Bargsten, M. Bazarnik, S. Krause, and R. Wiesendanger, “A radio-frequency spin-polarized scanning tunneling microscope”, *Review of Scientific Instruments* **90**, 123705 (2019).
- [72] P. J. Feibelman, “First-principles calculation of the geometric and electronic structure of the Be(0001) surface”, *Physical Review B* **46**, 2532 (1992).
- [73] H. L. Davis, J. B. Hannon, K. B. Ray, and E. W. Plummer, “Anomalous interplanar expansion at the (0001) surface of Be”, *Physical Review Letters* **68**, 2632 (1992).
- [74] J. B. Hannon, E. J. Mele, and E. W. Plummer, “Phonon dispersion at the Be(0001) surface”, *Physical Review B* **53**, 2090 (1996).
- [75] V. M. Silkin and E. V. Chulkov, “The linewidth of surface states of simple metals”, *Physics of the Solid State* **42**, 1373 (2000).
- [76] T. Chien, X. He, S.-K. Mo, M. Hashimoto, Z. Hussain, Z.-X. Shen, and E. W. Plummer, “Electron-phonon coupling in a system with broken symmetry: Surface of Be(0001)”, *Physical Review B* **92**, 075133 (2015).
- [77] R. Li, X. Cheng, H. Ma, S. Wang, D. Li, Z. Zhang, Y. Li, and X.-Q. Chen, “Dirac Node Lines in Pure Alkali Earth Metals”, *Physical Review Letters* **117**, 096401 (2016).
- [78] R. Li, J. Li, L. Wang, J. Liu, H. Ma, H.-F. Song, D. Li, Y. Li, and X.-Q. Chen, “Underlying Topological Dirac Nodal Line Mechanism of the Anomalously Large Electron-Phonon Coupling Strength on a Be (0001) Surface”, *Physical Review Letters* **123**, 136802 (2019).
- [79] A. Eiguren, S. de Gironcoli, E. V. Chulkov, P. M. Echenique, and E. Tosatti, “Electron-Phonon Interaction at the Be(0001) Surface”, *Physical Review Letters* **91**, 166803 (2003).
- [80] T. Ando, A. B. Fowler, and F. Stern, “Electronic properties of two-dimensional systems”, *Reviews of Modern Physics* **54**, 437 (1982).
- [81] J. Friedel, “Metallic alloys”, *Il Nuovo Cimento (1955-1965)* **7**, 287 (1958).
- [82] P. Avouris, I. W. Lyo, R. E. Walkup, and Y. Hasegawa, “Real space imaging of electron scattering phenomena at metal surfaces”, *Journal of Vacuum Science and Technology B* **12**, 1447 (1994).
- [83] B. G. Briner, P. Hofmann, M. Doering, H.-P. Rust, E. W. Plummer, and A. M. Bradshaw, “Observation of interfering Bloch waves”, *Europhysics Letters* **39**, 67 (1997).

- [84] B. G. Briner, P. Hofmann, M. Doering, H.-P. Rust, E. W. Plummer, and A. M. Bradshaw, “Charge-density oscillations on Be(10 $\bar{1}$ 0): Screening in a non-free two-dimensional electron gas”, *Physical Review B* **58**, 13931 (1998).
- [85] X. Zhu, Y. Cao, J. Zhang, E. W. Plummer, and J. Guo, “Classification of charge density waves based on their nature”, *Proceedings of the National Academy of Sciences of the United States of America* **112**, 2367 (2015).
- [86] M. Hengsberger, R. Frésard, D. Purdie, P. Segovia, and Y. Baer, “Electron-phonon coupling in photoemission spectra”, *Physical Review B* **60**, 10796 (1999).
- [87] P. Hofmann, I. Y. Sklyadneva, E. D. L. Rienks, and E. V. Chulkov, “Electron–phonon coupling at surfaces and interfaces”, *New Journal of Physics* **11**, 125005 (2009).
- [88] S. LaShell, E. Jensen, and T. Balasubramanian, “Nonquasiparticle structure in the photoemission spectra from the Be(0001) surface and determination of the electron self energy”, *Physical Review B* **61**, 2371 (2000).
- [89] I. Sklyadneva, E. V. Chulkov, P. M. Echenique, and A. Eiguren, “Electron–phonon interaction and hole (electron) lifetimes on Be(0001)”, *Surface Science* **600**, 3792 (2006).
- [90] S.-J. Tang, J. Shi, B. Wu, P. T. Sprunger, W. L. Yang, V. Brouet, X. J. Zhou, Z. Hussain, Z.-X. Shen, Z. Zhang, and E. W. Plummer, “A spectroscopic view of electron–phonon coupling at metal surfaces”, *physica status solidi (b)* **241**, 2345 (2004).
- [91] T. Chien, E. D. L. Rienks, M. F. Jensen, P. Hofmann, and E. W. Plummer, “Anisotropic electron-phonon coupling on a two-dimensional circular Fermi contour”, *Physical Review B* **80**, 241416(R) (2009).
- [92] R. Stedman, Z. Amilius, R. Pauli, and O. Sundin, “Phonon spectrum of beryllium at 80K”, *Journal of Physics F: Metal Physics* **6**, 157 (1976).
- [93] H. Hasegawa and D. G. Pettifor, “Microscopic Theory of the Temperature-Pressure Phase Diagram of Iron”, *Physical Review Letters* **50**, 130 (1983).
- [94] M. Nicol and G. Jura, “Mössbauer Spectrum of Iron-57 in Iron Metal at Very High Pressures”, *Science* **141**, 1035 (1963).

-
- [95] M. Ekman, B. Sadigh, K. Einarsdotter, and P. Blaha, “*Ab initio* study of the martensitic bcc-hcp transformation in iron”, *Physical Review B* **58**, 5296 (1998).
- [96] S. Hsieh, P. Bhattacharyya, C. Zu, T. Mittiga, T. J. Smart, F. Machado, B. Kobrin, T. O. Höhn, N. Z. Rui, M. Kamrani, S. Chatterjee, S. Choi, M. Zaletel, V. V. Struzhkin, J. E. Moore, V. I. Levitas, R. Jeanloz, and N. Y. Yao, “Imaging stress and magnetism at high pressures using a nanoscale quantum sensor”, *Science* **366**, 1349 (2019).
- [97] G. Steinle-Neumann, R. E. Cohen, and L. Stixrude, “Magnetism in iron as a function of pressure”, *Journal of Physics: Condensed Matter* **16**, S1109 (2004).
- [98] I. I. Mazin, D. A. Papaconstantopoulos, and M. J. Mehl, “Superconductivity in compressed iron: Role of spin fluctuations”, *Physical Review B* **65**, 100511(R) (2002).
- [99] V. Thakor, J. B. Staunton, J. Poulter, S. Ostanin, B. Ginatempo, and E. Bruno, “*Ab initio* calculations of incommensurate antiferromagnetic spin fluctuations in hcp iron under pressure”, *Physical Review B* **67**, 180405(R) (2003).
- [100] K. Shimizu, T. Kimura, S. Furomoto, K. Takeda, K. Kontani, Y. Onuki, and K. Amaya, “Superconductivity in the non-magnetic state of iron under pressure”, *Nature* **412**, 316 (2001).
- [101] D. Naglav, M. R. Buchner, G. Bendt, F. Kraus, and S. Schulz, “Off the Beaten Track—A Hitchhiker’s Guide to Beryllium Chemistry”, *Angewandte Chemie (International ed. in English)* **55**, 10562 (2016).
- [102] K. A. Walsh, *Beryllium chemistry and processing* (ASM International, Materials Park, OH, 2009).
- [103] A. J. Stonehouse, “Physics and chemistry of beryllium”, *Journal of Vacuum Science & Technology A: Vacuum, Surfaces, and Films* **4**, 1163 (1986).
- [104] M. Svilar, G. Schuster, T. Civic, P. Sabey, E. Vidal, S. Freeman, G. Petzow, F. Aldinger, S. Jönsson, P. Welge, V. Kampen, T. Mensing, and T. Brüning, “Beryllium and Beryllium Compounds”, in *Ullmann’s Encyclopedia of Industrial Chemistry* (Wiley-VCH, Weinheim, 2013).
- [105] R. O. Adams, “LEED and adsorption studies of Beryllium”, in *The structure and chemistry of solid surfaces*, edited by G. A. Somorjai (Wiley, New York, 1969), pp. 70.

- [106] A. J. Stonehouse and W. W. Beaver, "Surface treatments and coatings", in *Beryllium: Its Metallurgy and Properties*, edited by H. H. Hausner (University of California Press, Berkeley and Los Angeles, 1965), pp. 155.
- [107] R. G. Musket, W. McLean, C. A. Colmenares, D. M. Makowiecki, and W. J. Siekhaus, "Preparation of atomically clean surfaces of selected elements: A review", *Applications of Surface Science* **10**, 143 (1982).
- [108] D. E. Fowler and J. M. Blakely, "The initial oxidation of the beryllium (0001) surface", *Surface Science* **148**, 265 (1984).
- [109] M. Euler and A. Scharmann, "Thermally stimulated exoelectron emission (TSEE) of BeO layers. Auger electron spectroscopy investigations", *physica status solidi (a)* **34**, 297 (1976).
- [110] D. W. Aylmore, S. J. Gregg, and W. B. Jepson, "The high temperature oxidation of beryllium", *Journal of Nuclear Materials* **2**, 169 (1960).
- [111] R. O. Adams, *Cleaning an ideal beryllium surface*, edited by The Dow chemical company, Golden, Colorado, 1967.
- [112] R. G. Musket and R. J. Fortner, "Observation and Interpretation of the Auger Electron Spectrum from Clean Beryllium", *Physical Review Letters* **26**, 80 (1971).
- [113] F. Jona, J. A. Strozier, J. Kumar, and R. O. Jones, "Intensities of Low-Energy-Electron-Diffraction Beams from Be(0001)", *Physical Review B* **6**, 407 (1972).
- [114] K. Pohl, "The surfaces of beryllium and their interaction with hydrogen", PhD thesis (University of Pennsylvania, Philadelphia, 1997).
- [115] L. I. Johansson, H. I. P. Johansson, J. N. Andersen, E. Lundgren, and R. Nyholm, "Three surface-shifted core levels on Be(0001)", *Physical Review Letters* **71**, 2453 (1993).
- [116] K. Pohl, E. W. Plummer, S. V. Hoffmann, and P. Hofmann, "Phase diagram of hydrogen on Be(0001) from reconstruction-induced surface core-level shifts", *Physical Review B* **70**, 235424 (2004).
- [117] A. Kubetzka, M. Bode, O. Pietzsch, and R. Wiesendanger, "Spin-Polarized Scanning Tunneling Microscopy with Antiferromagnetic Probe Tips", *Physical Review Letters* **88**, 057201 (2002).
- [118] M. Schmid, W. Hebenstreit, P. Varga, and S. Crampin, "Quantum wells and electron interference phenomena in Al due to subsurface noble gas bubbles", *Physical Review Letters* **76**, 2298 (1996).

-
- [119] V. P. Chakin and Z. Ye Ostrovsky, “Evolution of beryllium microstructure under high-dose neutron irradiation”, *Journal of Nuclear Materials* **307-311**, 657 (2002).
- [120] R. E. Honig, “Vapor Pressure Data for the Solid and Liquid Elements”, *RCA Review* **23**, 567 (1962).
- [121] Y. Shapira and D. Lichtman, “Properties of Materials used in Vacuum Technology”, in *Vacuum physics and technology*, edited by G. L. Weissler and R. W. Carlson, Methods of experimental physics (Acad. Press, New York, 1981), pp. 345–423.
- [122] SPECS GmbH - Surface Analysis and Computer Technology Voltastrasse 5, 13355 Berlin, Germany, *Useful Information and Facts about Practice of Sputtering*, https://www.specs-group.com/fileadmin/user_upload/products/technical-note/sputter-info.pdf (visited on 10/14/2020).
- [123] H. Osterhage, R. Wiesendanger, and S. Krause, “Phonon-mediated tunneling into a two-dimensional electron gas on the Be(0001) surface”, *Physical Review B* **103**, 155428 (2021).
- [124] J. E. Hoffman, K. McElroy, D.-H. Lee, K. M. Lang, H. Eisaki, S. Uchida, and J. C. Davis, “Imaging quasiparticle interference in $\text{Bi}_2\text{Sr}_2\text{CaCu}_2\text{O}_{8+\delta}$ ”, *Science* **297**, 1148 (2002).
- [125] C. Hess, S. Sykora, T. Hänke, R. Schlegel, D. Baumann, V. B. Zabolotnyy, L. Harnagea, S. Wurmehl, J. van den Brink, and B. Büchner, “Interband quasiparticle scattering in superconducting LiFeAs reconciles photoemission and tunneling measurements”, *Physical Review Letters* **110**, 017006 (2013).
- [126] L. Petersen, P. T. Sprunger, P. Hofmann, E. Lægsgaard, B. G. Briner, M. Doering, H.-P. Rust, A. M. Bradshaw, F. Besenbacher, and E. W. Plummer, “Direct imaging of the two-dimensional Fermi contour: Fourier-transform STM”, *Physical Review B* **57**, R6858 (1998).
- [127] K. Schouteden, P. Lievens, and C. van Haesendonck, “Fourier-transform scanning tunneling microscopy investigation of the energy versus wave vector dispersion of electrons at the Au(111) surface”, *Physical Review B* **79**, 195409 (2009).
- [128] E. L. Wolf, *Principles of Electron Tunneling Spectroscopy*, 2nd ed. (Oxford University Press, New York, 2012).

- [129] P. M. Echenique, R. Berndt, E. V. Chulkov, T. Fauster, A. Goldmann, and U. Höfer, “Decay of electronic excitations at metal surfaces”, [Surface Science Reports](#) **52**, 219 (2004).
- [130] A. Bauer, A. Mühlig, D. Wegner, and G. Kaindl, “Lifetime of surface states on (0001) surfaces of lanthanide metals”, [Physical Review B](#) **65**, 075421 (2002).
- [131] B. A. McDougall, T. Balasubramanian, and E. Jensen, “Phonon contribution to quasiparticle lifetimes in Cu measured by angle-resolved photoemission”, [Physical Review B](#) **51**, 13891(R) (1995).
- [132] G. Grimvall, “The electron-phonon interactions in metals”, in *Selected Topics in Solid State Physics*, Vol. 16, edited by E. P. Wohlfarth (North Holland Publishing Company, Amsterdam, New York, Oxford, 1981).
- [133] B. Hellsing, A. Eiguren, and E. V. Chulkov, “Electron-phonon coupling at metal surfaces”, [Journal of Physics: Condensed Matter](#) **14**, 5959 (2002).
- [134] L. C. Davis, M. P. Everson, R. C. Jaklevic, and W. Shen, “Theory of the local density of surface states on a metal: Comparison with scanning tunneling spectroscopy of a Au(111) surface”, [Physical Review B](#) **43**, 3821 (1991).
- [135] J. Li, W.-D. Schneider, R. Berndt, O. R. Bryant, and S. Crampin, “Surface-State Lifetime Measured by Scanning Tunneling Spectroscopy”, [Physical Review Letters](#) **81**, 4464 (1998).
- [136] G. Hörmandinger, “Imaging of the Cu(111) surface state in scanning tunneling microscopy”, [Physical Review B](#) **49**, 13897 (1994).
- [137] J. Kliewer, R. Berndt, E. V. Chulkov, V. M. Silkin, P. M. Echenique, and S. Crampin, “Dimensionality effects in the lifetime of surface states”, [Science](#) **288**, 1399 (2000).
- [138] J. Kröger, M. Becker, H. Jensen, T. von Hofe, N. Néel, L. Limot, R. Berndt, S. Crampin, E. Pehlke, C. Corriol, V. M. Silkin, D. Sánchez-Portal, A. Arnau, E. V. Chulkov, and P. M. Echenique, “Dynamics of surface-localised electronic excitations studied with the scanning tunnelling microscope”, [Progress in Surface Science](#) **82**, 293 (2007).
- [139] F. Reinert, G. Nicolay, S. Schmidt, D. Ehm, and S. Hüfner, “Direct measurements of the L -gap surface states on the (111) face of noble metals by photoelectron spectroscopy”, [Physical Review B](#) **63**, 115415 (2001).

-
- [140] V. M. Silkin, T. Balasubramanian, E. V. Chulkov, A. Rubio, and P. M. Echenique, “Surface-state hole decay mechanisms: The Be(0001) surface”, *Physical Review B* **64**, 085334 (2001).
- [141] L. Bürgi, O. Jeandupeux, H. Brune, and K. Kern, “Probing Hot-Electron Dynamics at Surfaces with a Cold Scanning Tunneling Microscope”, *Physical Review Letters* **82**, 4516 (1999).
- [142] G. M. Watson, P. A. Bruhwiler, E. W. Plummer, H.-J. Sagner, and K.-H. Frank, “Two-Dimensional Band Structure of a Li layer: Li/Be(0001)”, *Physical Review Letters* **65**, 468 (1990).
- [143] C. J. Arguello, E. P. Rosenthal, E. F. Andrade, W. Jin, P. C. Yeh, N. Zaki, S. Jia, R. J. Cava, R. M. Fernandes, A. J. Millis, T. Valla, R. M. Osgood Jr., and A. N. Pasupathy, “Quasiparticle Interference, Quasiparticle Interactions, and the Origin of the Charge Density Wave in $2H\text{-NbSe}_2$ ”, *Physical Review Letters* **114**, 037001 (2015).
- [144] P. T. Sprunger, E. Lægsgaard, and F. Besenbacher, “Growth of Ag on Cu(100) studied by STM: From surface alloying to Ag superstructures”, *Physical Review B* **54**, 8163 (1996).
- [145] J. Homoth, M. Wenderoth, K. J. Engel, T. Druga, S. Loth, and R. G. Ulbrich, “Reconstruction of the local density of states in Ag(111) surfaces using scanning tunneling potentiometry”, *Physical Review B* **76**, 193407 (2007).
- [146] S. Grothe, S. Johnston, S. Chi, P. Dosanjh, S. A. Burke, and Y. Pennec, “Quantifying Many-Body Effects by High-Resolution Fourier Transform Scanning Tunneling Spectroscopy”, *Physical Review Letters* **111**, 246804 (2013).
- [147] J. B. Hannon and E. W. Plummer, “Shear Horizontal Vibrations at the (0001) Surface of Beryllium”, *Journal of Electron Spectroscopy and Related Phenomena* **64-65**, 683 (1993).
- [148] I. Y. Sklyadneva, E. V. Chulkov, W.-D. Schöne, V. M. Silkin, R. Keyling, and P. M. Echenique, “Role of electron-phonon interactions versus electron-electron interactions in the broadening mechanism of the electron and hole linewidths in bulk Be”, *Physical Review B* **71**, 174302 (2005).
- [149] J. Shi, S.-J. Tang, B. Wu, P. T. Sprunger, W. L. Yang, V. Brouet, X. J. Zhou, Z. Hussain, Z.-X. Shen, Z. Zhang, and E. W. Plummer, “Direct Extraction of the Eliashberg Function for Electron-Phonon Coupling: A case study of Be(1010)”, *Physical Review Letters* **92**, 186401 (2004).

- [150] E. Minamitani, N. Takagi, R. Arafune, T. Frederiksen, T. Komeda, H. Ueba, and S. Watanabe, “Inelastic electron tunneling spectroscopy by STM of phonons at solid surfaces and interfaces”, [Progress in Surface Science](#) **93**, 131 (2018).
- [151] Y. Zhang, V. W. Brar, F. Wang, C. Girit, Y. Yayon, M. Panlasigui, A. Zettl, and M. F. Crommie, “Giant phonon-induced conductance in scanning tunnelling spectroscopy of gate-tunable graphene”, [Nature Physics](#) **4**, 627 (2008).
- [152] V. W. Brar, S. Wickenburg, M. Panlasigui, C.-H. Park, T. O. Wehling, Y. Zhang, R. Decker, Ç. Girit, A. V. Balatsky, S. G. Louie, A. Zettl, and M. F. Crommie, “Observation of Carrier-Density-Dependent Many-Body Effects in Graphene via Tunneling Spectroscopy”, [Physical Review Letters](#) **104**, 036805 (2010).
- [153] K. Oetker, “Characterization of Fe/Be (0001) using scanning tunneling microscopy”, Master thesis (Universität Hamburg, Hamburg, 2021).
- [154] I. Leonov, A. I. Poteryaev, V. I. Anisimov, and D. Vollhardt, “Electronic Correlations at the α - γ Structural Phase Transition in Paramagnetic Iron”, [Physical Review Letters](#) **106**, 106405 (2011).
- [155] M. T. Kief and W. F. Egelhoff, “Growth and structure of Fe and Co thin films on Cu(111), Cu(100), and Cu(110): A comprehensive study of metastable film growth”, [Physical Review B](#) **47**, 10785 (1993).
- [156] A. Biedermann, W. Rupp, M. Schmid, and P. Varga, “Coexistence of fcc- and bcc-like crystal structures in ultrathin Fe films grown on Cu(111)”, [Physical Review B](#) **73**, 165418 (2006).
- [157] E. Bauer, “Epitaxy of metals on metals”, [Applications of Surface Science](#) **11/12**, 479 (1982).
- [158] L. Vitos, A. V. Ruban, H. L. Skriver, and J. Kollár, “The surface energy of metals”, [Surface Science](#) **411**, 186 (1998).
- [159] S.-J. Lee, Y.-K. Lee, and A. Soon, “The austenite/ ϵ martensite interface: A first-principles investigation of the *fcc* Fe(111)/*hcp* Fe(0001) system”, [Applied Surface Science](#) **258**, 9977 (2012).
- [160] I. Markov, “Kinetics of nucleation in surfactant-mediated epitaxy”, [Physical Review B](#) **53**, 4148 (1996).
- [161] R. C. Weast and D. R. Lide, eds., *CRC handbook of chemistry and physics*, 70. ed., (CRC Press, Boca Raton, 1989).

-
- [162] J. A. Stroscio, D. T. Pierce, A. Davies, R. J. Celotta, and M. Weinert, “Tunneling Spectroscopy of bcc (001) Surface States”, *Physical Review Letters* **75**, 2960 (1995).
- [163] C. Busse, C. Polop, M. Müller, K. Albe, U. Linke, and T. Michely, “Stacking-Fault Nucleation on Ir(111)”, *Physical Review Letters* **91**, 056103 (2003).
- [164] S. C. Middleburgh and R. W. Grimes, “Defects and transport processes in beryllium”, *Acta Materialia* **59**, 7095 (2011).
- [165] P. A. Burr, S. C. Middleburgh, and R. W. Grimes, “Crystal structure, thermodynamics, magnetism and disorder properties of Be-Fe-Al intermetallics”, *Journal of Alloys and Compounds* **639**, 111 (2015).
- [166] J. A. Venables, G. D. T. Spiller, and M. Hanbücken, “Nucleation and growth of thin films”, *Reports on Progress in Physics* **47**, 399 (1984).
- [167] L. Misch, “Über zwei intermetallische Verbindungen des Berylliums mit Eisen”, *Die Naturwissenschaften* **23**, 287 (1935).
- [168] H. Ohtani, Y. Takeshita, and M. Hasebe, “Effect of the Order-Disorder Transition of the bcc Structure on the Solubility of Be in the Fe-Be Binary System”, *Materials Transactions* **45**, 1499 (2004).
- [169] H. Okamoto and L. E. Tanner, “The Be-Fe (Beryllium-Iron) system”, *Bulletin of Alloy Phase Diagrams* **9**, 494 (1988).
- [170] K. Ohta, “Mössbauer Effect and Magnetic Properties of Iron–Beryllium Compounds”, *Journal of Applied Physics* **39**, 2123 (1968).
- [171] K. Ohta and Y. Nagata, “Magnetic Properties of Iron-Beryllium Compounds”, *Journal of the Japan Society of Powder and Powder Metallurgy* **25**, 141 (1978).
- [172] H. Samata, Y. Nagata, S. Morita, G. Tanaka, T. Mitsunashi, S. Yashiro, and S. Abe, “Magnetic properties of the Laves-phase compounds $\text{Fe}_{1-x}\text{Co}_x\text{Be}_2$ ”, *Journal of Alloys and Compounds* **302**, 29 (2000).
- [173] A. Schlenhoff, S. Krause, G. Herzog, and R. Wiesendanger, “Bulk Cr tips with full spatial magnetic sensitivity for spin-polarized scanning tunneling microscopy”, *Applied Physics Letters* **97**, 083104 (2010).
- [174] G. Rodary, S. Wedekind, D. Sander, and J. Kirschner, “Magnetic Hysteresis Loop of Single Co Nano-islands”, *Japanese Journal of Applied Physics* **47**, 9013 (2008).

- [175] M. Corbetta, S. Ouazi, J. Borme, Y. Nahas, F. Donati, H. Oka, S. Wedekind, D. Sander, and J. Kirschner, “Magnetic Response and Spin Polarization of Bulk Cr Tips for In-Field Spin-Polarized Scanning Tunneling Microscopy”, [Japanese Journal of Applied Physics](#) **51**, 030208 (2012).
- [176] M. Bazarnik, M. Abadia, J. Brede, M. Hermanowicz, E. Sierda, M. Elsebach, T. Hänke, and R. Wiesendanger, “Atomically resolved magnetic structure of a Gd-Au surface alloy”, [Physical Review B](#) **99**, 174419 (2019).

Index of abbreviations

AES Auger electron spectroscopy	4
ARPES angle resolved photoemission spectroscopy	25
bcc body-centred cubic	1
CBD chronic beryllium disease	31
CDW charge density wave	4
DFT density functional theory	2
DOS density of states	1
fcc face-centered cubic	71
FFT fast-Fourier transform	48
hcp hexagonal close-packed	2
IETS inelastic electron tunneling spectroscopy	4
LEED low energy electron diffraction	4

Index of abbreviations

LT low temperature	15
LT-STM low-temperature scanning tunneling microscope	21
MBE molecular beam epitaxy	1
ML mono-layer	17
PID proportional-integral-derivative	20
PTFE polytetrafluoroethylene	22
RF radio frequency	22
RKKY Ruderman-Kittel-Kasuya-Yosida	3
RT room temperature	100
SP-STM spin-polarised scanning tunneling microscopy	1
STM scanning tunneling microscopy	1
STS scanning tunneling spectroscopy	3
UHV ultra-high vacuum	15
VT variable temperature	15
VT-STM variable-temperature scanning tunneling microscope	19

Publications

- H. Osterhage, J. Gooth, B. Hamdou, P. Gwozdz, R. Zierold, and K. Nielsch, “Thermoelectric properties of topological insulator Bi_2Te_3 , Sb_2Te_3 , and Bi_2Se_3 thin film quantum wells”, [Applied Physics Letters](#) **105**, 123117 (2014).
- H. S. Shin, B. Hamdou, H. Reith, H. Osterhage, J. Gooth, C. Damm, B. Rellinghaus, E. Pippel, and K. Nielsch, “The surface-to-volume ratio: a key parameter in the thermoelectric transport of topological insulator Bi_2Se_3 nanowires”, [Nanoscale](#) **8**, 13552 (2016).
- C. Friesen, H. Osterhage, J. Friedlein, A. Schlenhoff, R. Wiesendanger, and S. Krause, “Scanning Seebeck tunneling microscopy”, [Journal of Physics D: Applied Physics](#) **51**, 324001 (2018).
- C. Friesen, H. Osterhage, J. Friedlein, A. Schlenhoff, R. Wiesendanger, and S. Krause, “Magneto-Seebeck tunneling on the atomic scale”, [Science](#) **363**, 1065 (2019).
- H. Osterhage, R. Wiesendanger, and S. Krause, “Phonon-mediated tunneling into a two-dimensional electron gas on the $\text{Be}(0001)$ surface”, [Physical Review B](#) **103**, 155428 (2021).

Conferences

Contributed talks

- 2019-04-01:
C. Friesen, H. Osterhage, J. Friedlein, A. Schlenhoff, R. Wiesendanger, and S. Krause, "Magneto-Seebeck Tunneling on the Atomic Scale". 83rd Spring Meeting, Deutsche Physikalische Gesellschaft, Regensburg (Germany).
- 2021-07-12
H. Osterhage, R. Wiesendanger, and S. Krause, "Phonon-mediated tunneling into Be(0001) surface states probed by scanning tunneling spectroscopy". International Conference on Nanoscience and Technology, Vancouver (Canada) (virtual meeting).
- 2021-09-27
H. Osterhage, K. Oetker, R. Wiesendanger, and S. Krause, "Iron growth on Be(0001) studied by STM". 84th Annual Meeting, Deutsche Physikalische Gesellschaft, virtual (Germany).

Posters

- 2017-03-24:
H. Osterhage, C. Friesen, and S. Krause, "Calorimetric Experiments on Fe/W(110) using SP-STM". 81st Spring Meeting, Deutsche Physikalische Gesellschaft, Dresden (Germany).
- 2019-06-18:
H. Osterhage, J.-H. Schmidt, R. Dao, V. Přikryl, S. Krause, and R. Wiesendanger, "Scanning Tunneling Spectroscopy of a clean Be(0001) surface". 8th International Conference on Scanning Probe Spectroscopy (SPS 19), Hamburg (Germany).

- 2021-03-02:
H. Osterhage, K. Oetker, R. Wiesendanger, and S. Krause "Phonon mediated tunneling into a 2D electron gas on the Be(0001) surface". Virtual DPG Spring Meeting of the Surface Science Division (SurfaceScience21), virtual (Germany).

Danksagung / Acknowledgments

Diese Arbeit wurde durch die Hilfe und die Unterstützung zahlreicher Menschen ermöglicht, denen ich zu Dank verpflichtet bin.

Herrn Prof. Dr. Wiesendanger danke ich herzlich für die Betreuung meiner Promotion und die kontinuierliche Unterstützung der experimentellen Arbeit. In dieser Forschungsgruppe durfte ich erstklassige Bedingungen zu forschen und zu lernen genießen.

Stefan Krause leitete das Forschungsprojekt und stand mir allezeit mit Rat und Tat zur Seite. Vielen Dank für die Unterstützung und all die Anregungen und Diskussionen.

In diesem Zusammenhang bedanke ich mich bei der Deutschen Forschungsgemeinschaft für die finanzielle Unterstützung meiner Arbeit im Rahmen des Projekts KR3771/2-1.

Ich hatte die Freude, die Abschlussarbeiten von Jan-Hendrik Schmidt und Karoline Oetker zu betreuen, die dieses Projekt mit ihrem Elan vorangetrieben haben. Ich bin mir sicher, dass die kollegiale Zusammenarbeit für uns alle vorteilhaft und lehrreich war.

Bei der tagtäglichen Laborarbeit hatte ich ferner tatkräftige Unterstützung von Vojtěch Příklad und Radek Dao. Vielen Dank für eure motivierte und selbständige Mitarbeit.

Die experimentelle Arbeit hat viele Tücken. Ich bedanke mich bei der gesamten Gruppe R, die einen enormen Erfahrungsschatz hegt, und insbesondere bei Cody Friesen, Anika Schlenhoff, Maciej Bazarnik, Aurore Finco, André Kubetzka, Philipp Lindner, Jonas Harm, Johannes Friedlein, Emil Sierda, Lucas Schneider, und Jonas Koch für hilfreiche Tipps und Diskussionen.

Außerdem habe ich der mechanischen Werkstatt für die technische Unterstützung zu danken. Auch ohne das besondere Engagement von Herrn Biedermann und des Helium-Teams um M. Brandt, M. Langer und H. Schröder wäre diese Arbeit nicht möglich gewesen. Die Sensibilität für die Bedürfnisse von uns Forschern empfand ich als bemerkenswert.

Besonderer Dank gilt meiner Familie, die mir die Fokussierung auf diese Arbeit mit ihrem Verständnis und ihrem Rückhalt in dieser Zeit ermöglicht hat.

Und schließlich Nadine, deren Zuversicht sich immer wieder auf mich übertragen und die mich getragen hat. Dankeschön.

Eidesstattliche Versicherung

Hiermit versichere ich an Eides statt, die vorliegende Dissertationsschrift selbst verfasst und keine anderen als die angegebenen Hilfsmittel und Quellen benutzt zu haben.

Die eingereichte schriftliche Fassung entspricht der auf dem elektronischen Speichermedium.

Die Dissertation wurde in der vorgelegten oder einer ähnlichen Form nicht schon einmal in einem früheren Promotionsverfahren angenommen oder als ungenügend beurteilt.

Hamburg, den _____